Fall 2013

Tensile failure during structural development of single-layer buckle folds

Xiaolong Liu

Department:

TENSILE FAILURE DURING STRUCTURAL DEVELOPMENT OF SINGLE-LAYER BUCKLE FOLDS

by

XIAOLONG LIU

A THESIS

Presented to the Faculty of the Graduate School of the

MISSOURI UNIVERSITY OF SCIENCE AND TECHNOLOGY

In Partial Fulfillment of the Requirements for the Degree

MASTER OF SCIENCE IN PETROLEUM ENGINEERING

2013

Approved by

Andreas Eckert, Advisor
Runar Nygaard
John P. Hogan.

ABSTRACT

Folds and fold trains of sedimentary strata are among the most common structural traps systems for hydrocarbon reservoirs. The existence of tensile fractures associated to buckle folding is associated to the distribution of extensional strain in the outer arc of the fold hinges. This study investigates the conditions under which tensile stresses develop due to buckling in a realistic in situ stress scenario. By applying a 2D finite element modeling approach, the influence of realistic mechanical stratigraphy (including strain rate, overburden depth, competence contrasts, viscosity, and permeability) on the development of single-layer buckle folds with Newtonian viscous rheology is studied. Based on the simulation results, it can be concluded that the buckling process cannot explain the common observation and occurrence of tensile failure. Only low permeability ($<10^{-19}$ m^2) or low overburden pressure environments are possible to generate tensile failure at the top of the fold crest. Tensile failures in the limb of the fold cannot be explained by buckling only. This study shows that for high permeability rocks the generation of tensile stress both at the crest and limb of the fold can be the result of buckling followed by erosional unloading. In summary, tensile stresses and associated failure in buckle folds systems are determined by material parameters and the strain history.

ACKNOWLEDGMENTS

I would like to thank my advisor, Dr. Andreas Eckert, for accepting me into the geomechanical modeling group as a research assistant and for being a supportive and encouraging mentor and friend during my graduate studies. Without his significant help both in academic research and daily life, I would have failed to overcome the barriers and difficulties caused by foreign language and lacking of related background knowledge. His technical guidance and editorial corrections have been important to the completion of this thesis. I also want to express my gratitude for the care given by his family and for making me feel at home in Rolla by offering free beer in his house.

I would like to thank Dr. Hogan and Dr. Nygaard for their guidance throughout past two years. Their help and comments have been essential for me to overcome the difficulties during my research.

My thanks also goes to my friends with whom I worked : Nevan Himmelberg, Deepak Gokaraju, Amin Amirlatifi, and Matthew Paradeis. Their assistance, along with the collaborative work environment in the Rock Mechanics office, immensely improved my research outcome. In particular, Nevan Himmelberg deserves a special thanks as my roommate and personal English teacher.

I also want express my gratitude to the Chevron ETC for the funding sources.

Last but not the least, I want to thanks my family for their support: my girlfriend Yun Wu for her understanding of the long distance relationship and encouragement; my parents Zhonglie Liu and Jing Zhu for their love and care throughout my life.

TABLE OF CONTENTS

LIST OF ILLUSTRATIONS

Figure Page

LIST OF TABLES

NOMENCLATURE

Symbol	Description
σ_3	Minimum Principal Stress
σ_1	Maximum Principal Stress
ρ_b	Bulk Density
ρ_d	Dry Density
M_t	Total Mass
V_t	Total Volume
ρ_w	Water Density
ϕ	Porosity
d	Depth
e	Void Ratio
G_s	Specific Gravity
σ	Stress
ε	Strain
C_{ijkl}	Stiffness Tensor
E	Young's Modulus
ν	Possion's Ratio
$\dot{\varepsilon}$	Strain Rate
μ	Viscosity
G	Shear Modulus
K	Bulk Modulus
$\boldsymbol{F}$	Force Vector
$\boldsymbol{T}$	Traction Vector
P_p	Pore Pressure
$\boldsymbol{\sigma}$	Stress Tensior
α	Effective Stress Coefficient
T_0	Tensile Strength
$\sigma_3^{'}$	Effective Minimum Principle Stress
σ_n	Normal Stress

τ	Critical Share Stress
S_0	Cohesion
ψ	Angle of Internal Friction
λ_d	Dominant Wavelength
R	Competence Contrast
h	Layer Thickness
μ_L	Layer Viscosity
μ_M	Matrix Viscosity
S_x	Horizontal Stretch
A	Amplitude
$\hat{L}_{arc}$	Fold Arc Length
P_L	Axial Load
M	Bending Moments
Q	Shear Force
w	Deflection
η	Coefficient of Viscosity
P	Static Pressure
K^e	Element Stiffness Matrix
f^e	Element Loading
q^e	Internal Force

1. INTRODUCTION

1.1. OVERVIEW

Folds are the most noticeable and common geological structure that provide evidence of Earth's ductile deformation. They are also viewed as natural images reflecting the evolution of rock bodies over geologic time scales. Folds and their properties have been studied for a number of reasons. Most importantly, folds represent structural traps for oil and gas accumulation. Anticlines and domes, parts of folded sedimentary layers, commonly act as collection sites for oil and gas that migrate up from hydrocarbon source rocks. This migration usually occurs in a permeable reservoir rock, such as porous sandstone. If the reservoir layer sealed by impermeable rocks is folded into either a dome or an anticline, further migration of both oil and gas will be prevented by closure of the folding structure. With the increase of soil temperature, gas is displaced from the oil and trapped by the impervious or nonporous folding layer (Figure 1.1).

The relationship between folding and fracture development also plays an important role in the porosity–permeability changes of potential reservoirs, which is important to hydrocarbons exploration and recovery (Sibson, 2003). New fractures and reactivation of pre-existing fractures in folded layers generally open parallel to fold axes and develop high permeability pathways for hydrocarbon migration, followed by fluid motion parallel to fold axes (Sibson, 2005). Since hydrocarbon transportation is strongly governed by folding and the influence of fracture development on structural permeability, it is important to investigate the kinematics of folding deformation kinematics and fracture evolution within source rock and reservoirs. Of particular interest in a geomechanical analysis of such reservoirs is the prediction of the location, type, extent, and orientation of these fold related structures both for fluid flow pathway and reservoir stability prediction.

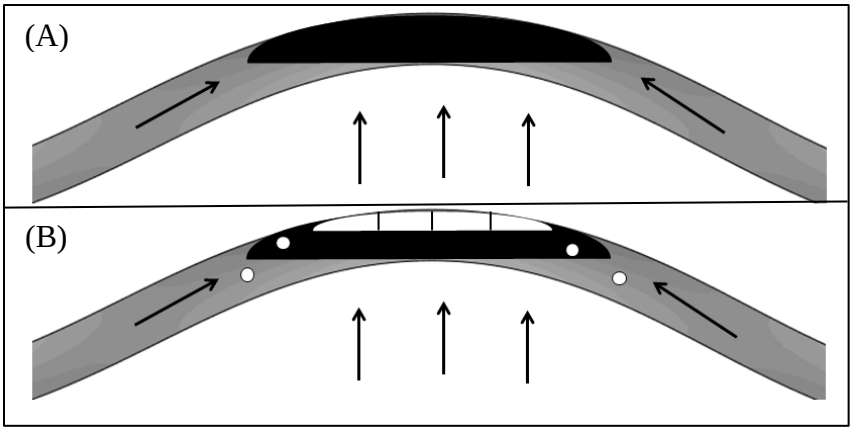

Figure 1.1 Sequential formation of oil (black) and gas (vertical lines and open circles) and filling an anticline. (A) Burial to the temperature of the formation of oil. (B) Additional burial to the temperature of the formation of thermal gas (Groshong, 1999).

1.2. LITERATURE REVIEW ON EXISTING KNOWLEDGE

Folded rock and their analysis have been studied extensively in the past fifty years to understand rock rheology, strain and deformation history from fold theory and modeling.

1.2.1. Fold Theory and Modeling. The dominant wavelength theory, developed by Biot (1959,1961), Biot et al.(1961) and Ramberg (1960,1964) for viscous materials, can be viewed as the most influential outcome from an enormous number of such studies. This theory has been modified by others (e.g, Chapple, 1968; Sherwin and Chapple,1968; Hudleston,1973; Fletcher,1974,1977,1979; Smith, 1975,1977,1979). According to the dominate wavelength theory, a single layer with many random, small perturbations embedded in a weaker matrix will develop into a fold when subjected to layer parallel shortening. The dominant wavelength depends on both the layer thickness as well as the competence contrast (i.e. the viscosity or Young's modulus contrast) between the layer and the surrounding material (here referred as a matrix). However, Biot's theory can only predict the finite folding stages in which the limb dip angle is below 20 degrees (Chapple,1969). Treagus (1973,1981) suggested that this theory could also be applicable to cases in which the layer is under oblique shortening with increasing stress at the boundary.

The initial perturbation plays an important role in the development of a single layer fold. Based on the results from models made from paraffin waxes of known rheological properties, Cobbold (1975) found that the initial perturbation propagates along the layer and further folds will appear serially in time and distance. Műhlhaus (1993) confirmed this finding with analytical results from the model with an elastic layer in a viscous matrix. Williams et al. (1978) determined that the final fold wavelength relies on the initial perturbation, even when the amplitude of the perturbation is small. The same conclusion is verified by Abbassi and Mancktelow (1990, 1992). They also discovered that the symmetry of the initial perturbation maintains. Random, finite-amplitude perturbations can exist before deformation in natural bedding layers. Therefore, the buckling theory, developed for a single layer with isolated, finite-amplitude perturbations, can be used to explain some natural folds.

In addition to analytical solutions and physical analogue models, two-dimensional (2D) numerical modeling of single-layer folding has been established to study the buckle folding process. Dieterich and Carter (1969) analyzed the two-dimensional large amplitude folding model of a viscous layer in a less viscous matrix. By using the finite element method, they show the changes of principal stress orientations during the different stages of the buckling process. Using a finite-difference code (FLAC), Zhang (1996) determined that the dominant wavelength is largely independent of the initial perturbation's position and shape. Mancktelow (1999), however, disagreed with this finding. He suggested that the initial perturbation may influence the final shape of the folding layers. This conflict results from using different strain rate. Zhang (2000) confirmed Mancktelow' theory by using finite-element (MARC) numerical models with low strain rate material.

For a linearly viscous layer and matrix, theoretically predicted initial growth rates, which depend on the layer's wavelength and thickness, are consistent with numerical results. Mancktelow (1999) presented that initial growth rates are independent of initial perturbations' waveform if a low-amplitude single waveform is initially applied. However, initial irregularities have influence on the geometry of the final folds (Mancktelow, 1999). This relation has also been verified for Newtonian materials (Mancktelow, 1999).

Considering both viscous and elastic properties, the system's response to buckling depends not only on the viscosity contrast, but also on the applied layer-parallel stress or strain rate. Using the Maxwell model in a numerical simulation, which contains both viscous and elastic properties, Schmalholz and Podladchikov (1999) confirmed that the developed wavelength of the viscoelastic folded layer, embedded in a viscous matrix, depends on the ratio of viscous dominant wavelength to elastic dominant wavelength. For the same system (a viscoelastic layer in viscous matrix), a transition from viscous properties dominate deformation to elastic properties dominate deformation with increasing strain rate Zhang (2000).

Besides 2D numerical models, three dimensional (3D) numerical simulations are also used to study fold geometry. Kocher et al. (2006) show that the final fold shapes of 3D folded layers are determined by the initial perturbation geometry of the layer and the boundary conditions. By using 3D numerical models with complex and non-cylindrical fold shapes, Schmalholz (2008) concludes that different fold axis orientations and curved fold axes can be generated from single direction shortening.

1.2.2. Fracture Patterns Associated with Folds. Major folds are characterized by associated fractures and the evolution history of these fracture sets becomes of interest. An early study of fractures in the Zagros buckle folds conducted by McQuillan (1973) focuses on the relationship between fracture spacing and folding layer thickness. The discussion of the possible mechanisms leading to this relationship is accomplished by Ladeira and Price (1981). However, the meaningful relationship between folding deformation and fracture orientation is neglected.

A diagram of minor fractures and cylindrical folded structures are shown by Price (1966), based on field observations and previous studies (see Figure 1.2).

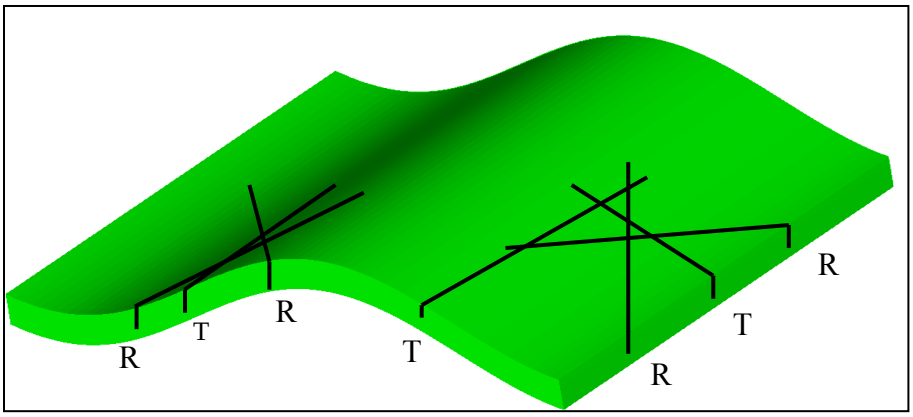

Figure 1.2.Trends of minor fractures in folded structures. R and T are shear and extension fractures, respectively (Price, 1966).

Price and Cosgrove (1990) study the relations between shear fractures and the principal stresses in the folded layer which is inferred by the Navier-Coulomb criterion of failure (fracture sets 1-4 in Figure 1.3A). Various orientations of the principal stresses give rise to differing types of shear fractures including normal, thrust and strike-slip faults. Fracture sets 5 and 6 (Figure 1.3B) indicate that the major tensile fractures are perpendicular to the fold axes with vertical or steeply dipping features (Price and Cosgrove, 1990). They also emphasize that the minimum principal stress (σ_3) acts perpendicular to the fracture plane (see Figure 1.3B). Tensile fracture can also be observed parallel to the fold axes if the minimum principal stress rotates ninety degrees. Price and Cosgrove proposed that different sets of fractures require different relations of the principle stress and develop at different times during fold development.

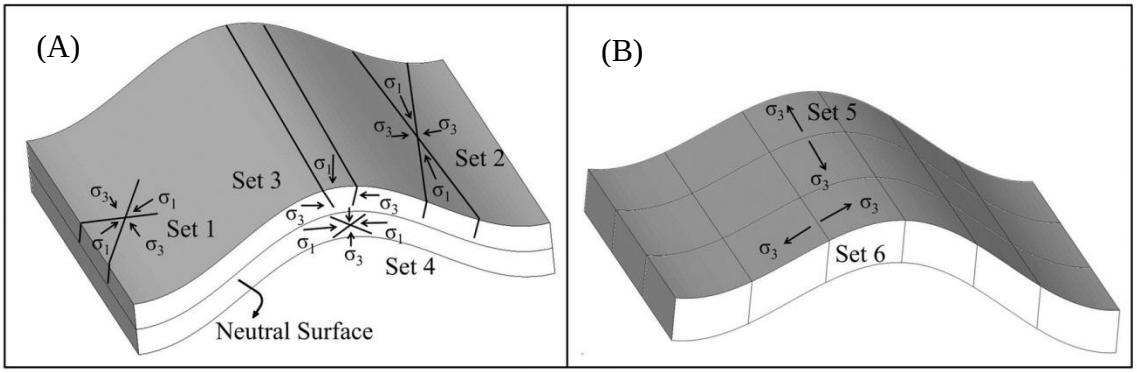

Figure 1.3: Fold associated fractures sets.(A) Set of 4 different shear fractures commonly associated to fold structures. (B) 2 sets of extensional fractures associated to fold structures

1.2.3. Tensile Failure within a Fold. To describe the development of homogeneous, isotropic layer buckling, the neutral surface concept (Ramsay, 1967) is used. As shown in Figure 1.4A, the outer arc of the crest reveals extension strain parallel to the folding layer. Conversely, the inner arc of the crest is under compression. The neutral surface which has no strain separates the layer-parallel extension region above the surface from the layer-parallel compression region below it. This strain distribution is referred as tangential longitudinal strain pattern, in which the maximum strain occurs at the crests (Johnson and Fletcher, 1994). Significant reduction of the compressive stress will occur above the neutral surface (Figure 1.4B). Ramberg (1964) suggested that the layer-parallel tension developed at the folding layer crest commonly produce tensile failures, known as tension gashes.

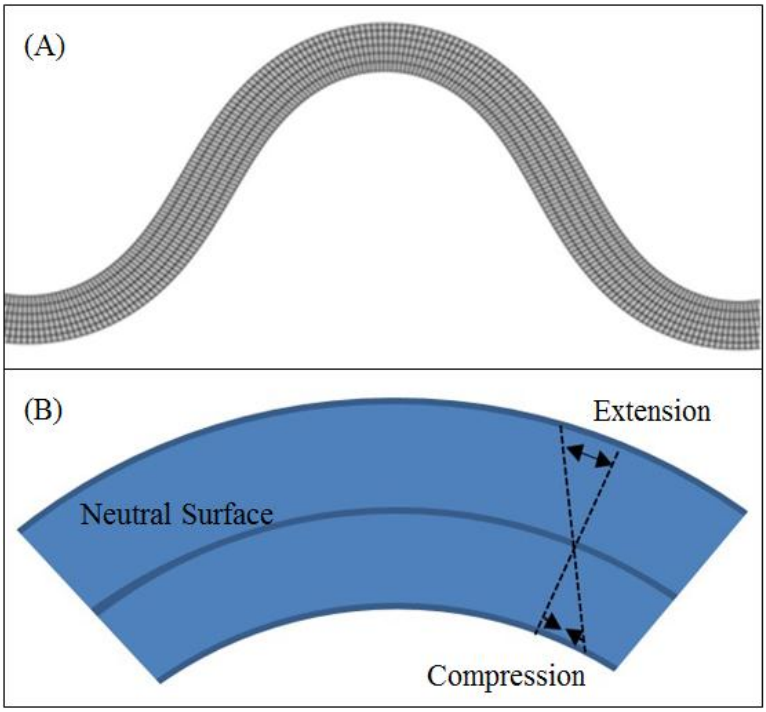

Figure 1.4: Strain distribution of folding layer. (A) Tangential longitudinal strain of folding layer under layer-parallel compression. (B) Tangential longitudinal strain reduces the stress above the neutral surface (Ramberg, 1964).

In addition to tensile strain, tensile failure can also be generated by pre-existing fractures, which formed during the rock geological history before buckling. Subjected to a variety of tectonic stress, the initial sets of fractures caused by tensile stresses are usually planar and parallel to each other (Harrison and Hudson, 2000). Assumed to be cohesion-less, pre-existing tensile fractures can be easily reactivated during folding and have a significant effect on the rock strength, permeability and deformability. The reactivation of pre-existing tensile fracture can also lead to new tensile fracture near them (Twiss and Moores, 2007).

The influence of pore pressure has also been characterized and considered in the tensile failure generation during rock buckling. This influence can be described by effective stress, which is the difference of total stress and pore pressure (Hubbert and Rubey, 1959). Tension failures form when the minimum effective stress reaches the rock tensile strength. This will happen if the minimum total stress is reduced by significant pore pressure (Watts, 1987).

1.2.4. Fold Curvature Analysis. Fold curvature analysis has been used to analyze the relations between the folded layer geometry and folding related fractures, including fracture density and fracture orientation (Lisle, 1994; Fischer and Wilkerson, 2000; Hennings et al., 2000). For cylindrical fold structures, curvature is expressed as the reciprocal of the radius of curvature which is perpendicular to the fold axis. As a parameter to describe the bending degree of fold surface, fold curvature has been recognized that may result in fracturing. Murray (1968) studied the relations between the radius of a competent unit's curvature to the fracture porosity in an oilfield at North Dakota. Stearns and Friedman (1972) presented models of fracture orientation and distribution for non-cylindrical folds. Narr (1991) related the fracture density to the plunging fold in the Point Arguello oilfield, California. And Ericsson et al. (1988) discovered a relationship between the fold curvature and fracture density for the Fateh Field. Generally, the fractures density increases with the increment of the curvature value (Suo, et.al. 2011). Considering the significant influence on rock's anisotropic permeability, fold curvature analysis has been applied in reservoir modeling (e.g. Stewart and Podolski, 1998). However, a recent fold curvature study shows that the strains analysis from geomechanical model may not be sufficient to interpret fracture characteristics such as density and orientation (Fischer and Wilkerson, 2000; Bergbauer and Pollard, 2004;Smart et al., 2009).

1.2.5. Limitations of Existing Literature. While a great amount of knowledge has been gained on the evolution of folds and their stress and strain history, lots of assumptions and simplifications are made. Only few studies consider the influence of gravity (Schmalholz et al., 2002) and the influence of pore pressure (Stephansson, 1974; Schmalholz and Podladchikov, 1999; Mancktelow, 2002). While the influence of the physical parameters on fold deformation is well understood from a collection of studies, the prediction of the timing and evolution of fold related fractures has not been fully studied yet. The relations between stress and strain result from flexural deformation due to bulking and the tensile failure distribution at the hinge and in the limbs of folded layer needs future investigation. Frehner's (2011) study relates the occurrence of tensile failure with the occurrence of extensional strains. However, the extensional stain is not necessary to cause tensile fractures which only develop when the minimum effective

principal stress exceeds the tensile strength of the rock (Jaeger and Cook, 1979). Thus, for tensile failure to occur at depth where stresses are compressive due to overburden stress, field observations from outcrops exhibiting tensile failure may not be a valid sample with which to confirm tensile failure at depth. The importance of overburden stress and pore pressure has been addressed by Frehner (2011). However, the quantitative description of the importance of these parameters is lacked due omission of these parameters in Frehner's (2011) modeling study. Hence, a more thorough understanding of tensile fracture generation and evolution in folded layers under realistic in situ stress conditions is necessary.

1.3. RESEARCH OBJECTIVES

The objective of this study is to apply 2D plane strain Finite Element Analysis (FEA) to simulate 2D single-layer buckle folding under realistic stress magnitudes. The stress and strain evolution modeled is used to provide a better understanding on the occurrence and spatial distribution of tensile fractures associated to buckle folding. In this study 2D linear visco-elastic rheology including pore pressure for a visco-elastic consolidation analysis is used which enables to study the effect of pore pressure and permeability during the fold development. These parameters are only included in "selected" studies (e.g. Ladeira, 1978; Davis et al., 1983) and a more thorough understanding of their influence is necessary.

Specific objectives to be addressed include the following:

(1) Setup 2D finite element models to simulate single-layer buckle folding using realistic in situ stress magnitudes.

(2) Perform sensitivity analysis on variety of input parameters (e.g. competence contrast, viscosity, strain rate, overburden pressure and hydraulic conductivity) to study their influence on the stress history during the folding process.

(3) Relate state of stress during the various folding stages to the occurrence of folding related tensional fractures.

1.4. RESEARCH QUESTIONS

The following questions related to tensile failure during the development of a folding structure are being addressed:

- What are the conditions for tensile failure to occur during folding? In particular, is flexure due to buckling the only physical process that explains tensile failure at the hinge and in the limbs of buckle folds?
- At which locations within the fold does tensile failure occur?
- At which stages during the fold development does tensile failure occur?
- What is the influence of material parameters (viscosity, permeability) and model boundary conditions (strain rate, burial depth) on the occurrence of tensile failure?
- For specific conditions, can tensile failure at depth be expected for low amplitude, low permeability shale layers?

2. THEORETICAL BACKGROUND

2.1. ROCK PROPERTIES

Reservoir rocks represent a geologic material including a network of interconnected pores for storing the fluids (gases, liquid hydrocarbons, water and other solutions) and allowing for their motion within the rocks. As the material forming a reservoir, reservoir rock properties and their effects on fluid motion are very important to the petroleum industry. These properties, such as density and permeability, are influenced by the state of stress acting on the rock. In return, rock properties can also have impact on the state of stress and the relationship between stress and strain.

2.1.1. Rock Density. Rock density is defined as mass per unit volume. Because the different phases are present in the material, several forms of rock densities are used in geotechnical research. Bulk density (ρ_b), is the most common one of these densities. It stands for the total (or wet) density calculated as total mass (M_t) divided by the total volume (V_t)

$$\rho_b = \frac{M_t}{V_t} \tag{1}$$

Dry density (ρ_d) is defined as the density of the rock at the same volume without either fluid or air in the material. The relationship between dry density and bulk density is given as (Chapman, 1983):

$$\rho_b = (1-\phi)\rho_d + \phi\rho_w \tag{2}$$

where ϕ represents rock porosity and ρ_w represents water density.

2.1.2. Rock Porosity. Porosity (ϕ) is the magnitude of reservoir rock's storage capacity of fluid. It is defined as the ratio of void space (V_{void}) to bulk volume (V_{bulk}) and can be expressed as either a percent or a fraction

$$\varphi = \frac{V_{void}}{V_{bulk}} \quad (3)$$

The void space generated in rocks is called pore space and filled with fluid. Many of the pores connect to each other in reservoir rocks, whereas others are completely isolated. When the volume of these pore spaces are determined by the interconnected pore spaces, the rock porosity is called effective porosity. The effective porosity represents the rock material ability to allow the fluid to circulate and ranges from 5% to 30% in petroleum reservoirs (Tiab and Donaldson, 2012). Low porosity means the effective porosity is lower than 5% and high porosity is above 20%.

2.1.3. Rock Permeability. Rock permeability refers to a rock's ability to allow fluid to flow through its pores. Permeability can be determined or obtained directly by either core analysis, well testing or well logging interpretations. Because rock permeability is seldom uniform throughout a petroleum reservoir, the average permeability of the reservoir layers must be determined.

Isotropic permeability is uncommon in most reservoir rocks. Permeability typically varies significantly between the vertical and horizontal planes within a formation (Jaeger and Cook, 1979). It is especially important when horizontal or partially penetrated wells are designed in the reservoir. The permeability in one horizontal direction is not always close to that in another perpendicular, horizontal direction. Permeability in the vertical direction, however, is typically different. It is usually much smaller than horizontal permeability. Based on small-scale probe permeability measurements on differently oriented faces of highly cemented sandstones, Meyer (2002) obtained the ration between vertical permeability and horizontal permeability. The ratio ranges from 0.1 to 1.0.

2.1.4. Reduction in Density, Porosity and Permeability with Depth. The reduction of density, porosity, and permeability as depth increases has been found in various basins and regions around the world (Twiss and Moores, 2008). This reduction results from mechanical compaction and the impact of post-depositional events.

Effective stress is defined as the difference between overburden stress and hydrostatic pressure in normally pressured rock. Plumley (1980) suggested that the

increment in effective stress usually leads to rock compaction along pore volume reduction and formation fluids. The rate of porosity change varies in different types of rock. Medina and Rupp (2011) studied both porosity versus depth and the permeability-porosity relationship. The conclusion is based on porosity values obtained from geophysical loges and porosity values form core analyses in different areas in the U.S. They described the regional trend of decreasing porosity with depth as follows:

$$\phi(d) = 16.39\ e^{-0.00039\ d} \tag{4}$$

where ϕ is the porosity and d is the depth in m.

To understand the relationship between density and porosity, we must first examine both the void ratio and the specific gravity of soil first. The void ratio (e) is used to express the void content of soil. It is expressed as the ratio of the volume of voids to the volume of the soil solids

$$e = \frac{V_{voids}}{V_{solids}} \tag{5}$$

The relationship between porosity and void ratio can be derived as:

$$e = \frac{V_{voids}}{V_{soild}} = \frac{V_{voids}}{V_{bulk} - V_{voids}} = \frac{\frac{V_{voids}}{V_{bulk}}}{1 - \frac{V_{voids}}{V_{bulk}}} = \frac{\phi}{1-\phi} \tag{6}$$

The specific gravity of soil solids (G_s) is introduced here to express the dry density of soil. It is defined as the mass of a volume of material over the mass of the same volume of water. Once calculated, the dry density can be derived as

$$\rho_d = \frac{G_s \rho_w}{1+e} = G_s \rho_w (1 - \Phi) \tag{7}$$

The dry density will increase as a result of the porosity reduction when the depth increases.

2.1.5. Hooke's Law and Elastic Moduli. The material ability to resist and recover from deformation is called elasticity. The theory of linear elasticity is the simplest type of response in which the strain is a function of stress without depending on the stress history or stress path. For elastic materials, stress (σ) and strain (ε) are related to each other by Hooke's Law where stress and strain depend linearly on each other. The general form of Hooke's law is as:

$$\sigma_{ij} = C_{ijkl}\varepsilon_{kl} \qquad (\text{with i, j, k, l=1,2,3}) \qquad (8)$$

where C_{ijkl} is the stiffness tensor with 81 entries. The stiffness tensor contains the elastic constants of a medium and relates the medium deformation to the applied stress.

For isotropic media in which the elastic properties at any point are independent from direction, the stiffness tensor can be expressed as:

$$C_{ijkl} = \begin{pmatrix} C_{33} & C_{12} & C_{12} & 0 & 0 & 0 \\ C_{12} & C_{33} & C_{12} & 0 & 0 & 0 \\ C_{12} & C_{12} & C_{33} & 0 & 0 & 0 \\ 0 & 0 & 0 & C_{55} & 0 & 0 \\ 0 & 0 & 0 & 0 & C_{55} & 0 \\ 0 & 0 & 0 & 0 & 0 & C_{55} \end{pmatrix} \qquad (9)$$

In a uniaxial state of stress (e.g., $\sigma_{11}= 0$, $\sigma_{22} =\sigma_{33}= 0$), the linear relation between applied stress σ and corresponding strain ε in the same direction can be represented by the equation

$$\sigma_{ii} = E\varepsilon_{ii} \qquad (10)$$

where E is the Young's modulus. Young's modulus is the rock resistance against compression by a uniaxial stress (Jaeger and Cook, 1979).

Another elastic parameter, Possion's ratio, is defined as the negative of the ratio of the transverse strain (j-direction) and the axial strain (i-direction). Possion's ratio (ν) can be expressed as

$$\nu = -\frac{\varepsilon_{jj}}{\varepsilon_{ii}} \tag{11}$$

For a liner elastic material, Possion's ratio is a function of stress and in the range 0 to 0.5 (Jaeger and Cook, 1979).

2.1.6. Two-dimensional Formulation. Because of the complexity of the three-dimensional elasticity field equations, analytical solutions are very difficult to obtain. Thus, many problems are simplified and solved by plane theory of elasticity in two-dimension. By removing one coordinate (e.g. the z-axis), all the dependent variables are independent of the z-axis and applied only in the x-y plane. The related general basic theories are plane strain and plane stress theory.

2.1.6.1 Plane strain theory. Plane strain is an approximation which is applicable to thick plane. If the problem is described in x-y plane, plane stain theory assumes that the strain normal to the x-y plane, ε_z, and shear strains (ε_{xz} and ε_{yz}) to be zero. From isotropic form of Hook's law, the stress can be expressed as (Sadd, 2009):

$$\varepsilon_{xx} = \frac{(1-\nu^2)}{E}\left[\sigma_{xx} - \frac{\nu}{1+\nu}\sigma_{yy}\right] \tag{12}$$

$$\varepsilon_{yy} = \frac{(1-\nu^2)}{E}\left[\sigma_{yy} - \frac{\nu}{1+\nu}\sigma_{xx}\right] \tag{13}$$

$$\sigma_{zz} = -\nu\left(\sigma_{yy} + \sigma_{xx}\right) \tag{14}$$

$$\varepsilon_{xy} = \frac{E}{2(1+V)}\sigma_{xy} \tag{15}$$

2.1.6.2 Plane stress theory. The second type for 2D system is plane stress theory. If the problem is described in x-y plane, this theory assumes that the stress normal to the x-y plane, σ_{zz}, and shear stresses (τ_{xz} and τ_{yz}) to be zero. From isotropic form of Hook's law, the stress can be expressed as (Sadd, 2009):

$$\varepsilon_{xx} = \frac{1}{E}\left[\sigma_{xx} - v\sigma_{yy}\right] \tag{16}$$

$$\varepsilon_{yy} = \frac{1}{E}\left[\sigma_{yy} - v\sigma_{xx}\right] \tag{17}$$

$$\sigma_{zz} = -\frac{v}{E}\left(\sigma_{xx} + \sigma_{yy}\right) \tag{18}$$

$$\varepsilon_{xy} = \frac{1+v}{E}\sigma_{xy} \tag{19}$$

2.1.7. Inelastic Rock Phenomenon and Properties. The assumption of the elastic behavior is that there is no internal and microscopic degradation developed in the rock. This implies that the rock will return to its initial state once the acting force is removed and there is no time-depend behavior. However, rock deforms irreversibly under most situations, which can be referred as inelastic behavior. Inelastic properties include plasticity and viscoelasticity. Along with inelastic behavior, there are some time-depend effects, including creep. Creep is the phenomenon in which rock continues to deform under constant applied stress (Harrison and Hudson, 2000).

2.1.7.1 Folding and pressure solution creep. The minerals solubility in water is determined by pressure and temperature. In rocks saturated with water, minerals are dissolved at high stress grain boundaries and precipitated at the low stress grain boundaries. This is referred as pressure solution creep (Karato, 2008). Such mass transfer by pressure around various sizes of grains (from microns to decimeters) in rock allows major internal deformation to be performed along with folding processes in the upper crust. This type of deformation evidence is found in sedimentary and metamorphic rocks (Dick and Sinton, 1979). Observations of geological structures exhumed from depth in compacted fold zones indicate the ductile material behavior throughout the upper crust. The ductile processes controlled by pressure solution creep take place in the crust over

much longer time scales. Pressure solution creep is thought to be crucial for rocks to generate folds rather than fractures at relatively low temperatures (Turcotte and Gerald, 2002).

Sedimentary rocks subjected to pressure solution creep can have a Newtonian fluid behavior because a linear relationship between strain rate and stress is followed. Thus, pressure solution creep, a viscous rheology, is the mechanism that can explain the development of folds in crustal rocks at low temperatures and pressures and pressure solution creep laws are used to model the rock viscous behavior in folding processes (Laubshe, 1975).

2.1.7.2 Strain rate. The rate at which a rock is either shortened or stretched during the deformation must also be investigated. Thus, the strain rate ($\dot{\varepsilon}$) during deformational development is introduced. Strain rate is the rate of deformation change with respect to time.

$$\dot{\varepsilon} = \frac{d\varepsilon}{dt} \tag{20}$$

Most rock deformation occurs at a very slow rate. Pfiffner and Ramsay (1982) concluded that based on the finite strain analysis, the strain rates should fall within a range form 10^{-13} and 10^{-15} s^{-1}. More recently, both Passchier and Trouw (2005) as well as Twiss and Moores (2008) suggested that natural geological strain rates vary between 10^{-12} and 10^{-15} s^{-1}.

2.1.7.3 Viscosity. Viscosity is used to describe the fluid resistance to load. The simplest fluid is Newtonian fluid, in which the strain rate is proportional to the stress. Thus, viscous deformation is time depended and strain accumulates over time. For a Newtonian fluid, the viscous deformation is irreversible since there is no participating elastic deformation and the material fails to recover to its original state. Relating the shear stress and shear strain rate, viscosity for a Newtonian fluid is expressed as:

$$\sigma = 2\mu \frac{d\varepsilon}{dt} \tag{21}$$

Where μ is the viscosity.

2.1.7.4 Viscoelasticity. Viscoelasticity represents the property of the materials that can exhibit both viscous and elastic characteristics when undergoing deformation. Among the rock viscoelastic models, the Maxwell model is the most widely used. In this model, the material is viewed as a combination of a spring (which represents the elastic element) and a dashpot (which signifies a Newtonian viscous element, see Figure 2.1). During deformation, the rapid elastic response is coupled with the viscous response. The total strain (ε_{ij}) is the sum of the elastic strain (ε_{ij}^{e}) and the viscous strain (ε_{ij}^{v})

$$\varepsilon_{ij} = \varepsilon_{ij}^{v} + \varepsilon_{ij}^{e} \tag{22}$$

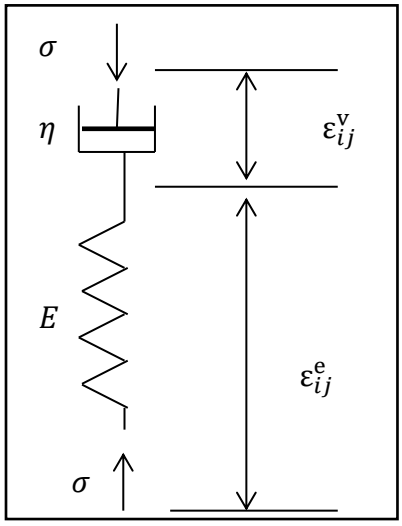

Figure 2.1 Maxwell Elastic-viscous model

Jaeger and Cook (1979) show the relationship between the elastic strain (ε_{ij}^{e}) and the stress (σ_{ij})

$$\sigma_{ij} = 2G\varepsilon_{ij}^{e} + (k - \frac{2}{3}G)\delta_{if}\varepsilon_{kk}^{e} \tag{23}$$

where G is the shear modulus and K is the bulk modulus. The Kronecker delta function (δ_{ij}) is defined as

$$\delta_{if} = \begin{cases} 0 & i \neq j \\ 1 & i = j \end{cases} \tag{24}$$

The relationship between viscous strain rate ($\dot{\varepsilon}_{ij}^{e}$) and stress ($\sigma_{ij}$) can be expressed as:

$$\sigma_{ij} = 2\mu\dot{\varepsilon}_{ij}^{v} - \frac{2}{3}\mu\delta_{ij}\dot{\varepsilon}_{kk}^{v} \tag{25}$$

where μ represents viscosity. The rock behavior described in Equations (20) and (25) illustrate the immediate elasticity and flow viscosity under stress over a long period of time. The elastic-viscous material is used to predict the unrecoverable behavior in rock deformation at a high temperature, a low strain rate and a high confining pressure. This model has been widely used in modeling of folding (e.g. Zhang et al., 1996, 2000; Mancktelow, 1999; Price, 1990).

2.2. BASIC THEORY OF ROCK MECHANICS

Rock mechanics represents the mechanics concerned with the rock response to the physical environment. Many basic mechanical concepts, such as force and motion, need to be adjusted when they are applied to deformable rocks. Reservoir stresses, rock deformations and failure have significant influence on the structural development of a geological formation. The existence of fractures in folded layers, such as sets of joints of limited continuity, constrains the equilibrium state of stress in the rocks. By applying rock mechanics, different sets of fractures can be related to the characteristics of the stress field in folded layers. Besides, the analysis of folding associated fractures is complicated by the fact that some joint sets developed pre-folding, while others accompanied the fold formation or were generated afterwards. Thus, the mechanical

behavior of folded layer rocks (and the surrounding formations) is important to assess geomechanical risks.

The following theoretical concepts can be found in extensive detail in standard text book such as Jaeger and Cook (1979) and Twiss and Moores (2007).

2.2.1. Traction Vector and Stress Tensor. Crustal deformations are due to the action of body forces and surface forces. Body forces are proportional to the volume or mass of the body. Surface forces act on arbitrarily oriented surfaces bounding rock units. The resistance against surface forces is termed stress and is expressed by the traction vector T. If the force acting through the plane is denoted as force vector $\boldsymbol{F}$, the tractor vector $\boldsymbol{T}$ averaged on the area can be expressed as:

$$\boldsymbol{T} = \frac{1}{\mathrm{A}}\boldsymbol{F} \tag{26}$$

where the area of a rock plane is A. The traction vector $\boldsymbol{T}$ acting on a point at the plane is defined by the limit:

$$\boldsymbol{T} = \lim_{d\mathrm{A}\to 0} \frac{1}{d\mathrm{A}} d\ \boldsymbol{F} \tag{27}$$

The standard unit of stress is the Pascal (1Pa =1N/m^2). In general, the traction vector $\boldsymbol{T}$ is a function of location and varies from point to point, Cauchy first introduced the concept of stress (Davis and Selvadurai, 1996). The totality of all traction vectors passing through all surfaces at a single point is termed the state of stress. If $\boldsymbol{n}$ represents a unit vector normal to the plane, the traction vector can be determined by:

$$\boldsymbol{T} = \boldsymbol{\sigma}^{T}\boldsymbol{n} \tag{28}$$

where the matrix $\boldsymbol{\sigma}$ without the transpose operator is the stress tensor. The stress tensor can be written as:

$$\boldsymbol{\sigma} = \begin{bmatrix} \sigma_{xx} & \sigma_{xy} & \sigma_{xz} \\ \sigma_{yx} & \sigma_{yy} & \sigma_{yz} \\ \sigma_{zx} & \sigma_{zy} & \sigma_{zz} \end{bmatrix} \tag{29}$$

A total of nine stress components exist for a complete description of the stress state at a point. The subscripts i and j may be any of x, y, and z, which represent the x, y and z axis respectively. The first subscript (i) identifies the axis normal to the actual surface, while the second subscript (j) identifies the direction of the force. Thus, σ_{xx} represents normal stress on a surface normal to the x direction. σ_{xy} and σ_{xz} represent the shear stress on the same plane perpendicular to the y-direction and z-direction, respectively (see Figure 2.2). The stress tensor is a symmetric matrix. Thus, σ_{xy} equals to σ_{yx} and equation 28 can be rewritten as:

$$\boldsymbol{T} = \boldsymbol{\sigma}\ \boldsymbol{n} \tag{30}$$

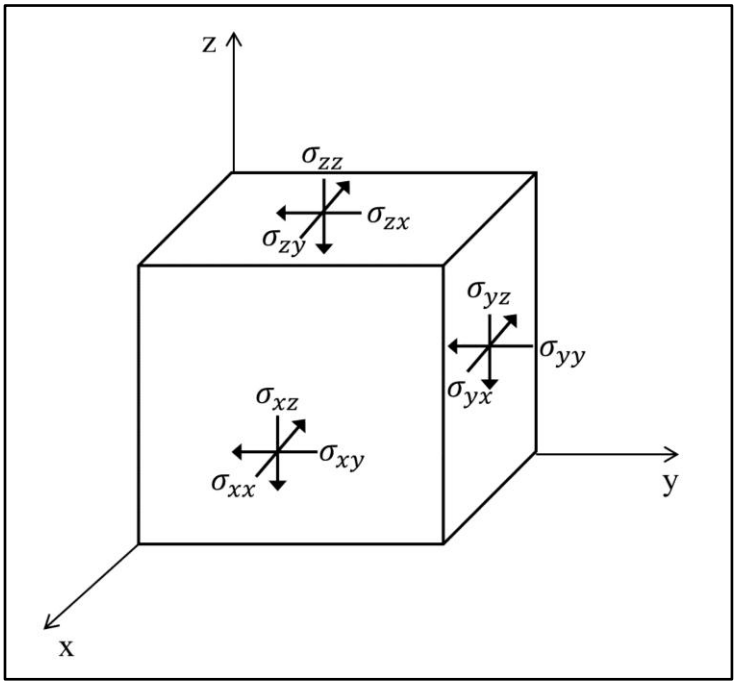

Figure 2.2 Stress components in three dimensions

2.2.2. Principal Stresses and Effective Stress. If the selected coordinate system shown in Figure 2.2 is rotated in three-dimensional space, a unique orientation can be found in which all of the shear stress components vanish from all of the surfaces. This unique orientation without any shear stress on any elemental cube face is defined as the principal orientation. The normal stresses on these planes of zero shear stress are known as principal stresses. The stress tensor for three-dimensional principal stresses can be expressed as

$$\sigma = \begin{bmatrix} \sigma_1 & 0 & 0 \\ 0 & \sigma_2 & 0 \\ 0 & 0 & \sigma_3 \end{bmatrix} \tag{31}$$

For a rock at certain depth below the water table, the pore space in it is filled with fluid under pressure. The pore fluid, which may be water, oil or gas, may affect the rock strength due to the existence of pore fluid press or the chemical interactions between the fluid and the rock. Considering the mechanical effect of pore fluid, the rock failure would be controlled by the effective stress (σ′), which can be expressed as (Terzaghi, 1936):

$$\boldsymbol{\sigma}' = \boldsymbol{\sigma} - \alpha P_p I \tag{32}$$

where P_P is pore fluid pressure and I is the identity tensor. The parameter α is referred as the effective stress coefficient. Following Terzaghi's effective stress principle, an increase in pore pressure effectively shifts the Mohr circle to the left, thus increasing the likelihood of failure.

2.2.3. Rock Failure. Failure can occur when rock is subject to sufficiently large stresses, followed by permanent shape change. To understand this complex behavior, rock failure is analyzed by combining the state of stress with the rock strength. As a main objective of this study is to predict the occurrence of rock failure associated to buckle folding, it is important to understand the conditions under which rock fail. For this study we assume homogeneous and isotropic rocks and follow and apply the standard failure for tensile and shear failure.

The fundamental modes of rock fracture are characterized as mode I (opening), mode II (sliding), and mode III (scissoring) (Fjar, et al., 2008). Mode I fractures represent pure extension opened by tensile stresses which are perpendicular to the fracture plane. There is no shear traction component in this fracture model (see Figure 2.3 A). Mode II is in plane shear fracture with shear traction parallel to both the fracture surface and the fracture propagation direction (see Figure 2.3 B). Mode III is lateral shear model with shear traction parallel to the fracture surface. Mode III fracture is characterized as a scissors-like movement perpendicular to the fracture propagation direction (see Figure 2.3 C). In reality, mixed mode failure, which refers to the combination of mode I and mode II, or mode I and mode III occurs during geological time scales (Fjar, et al., 2008).

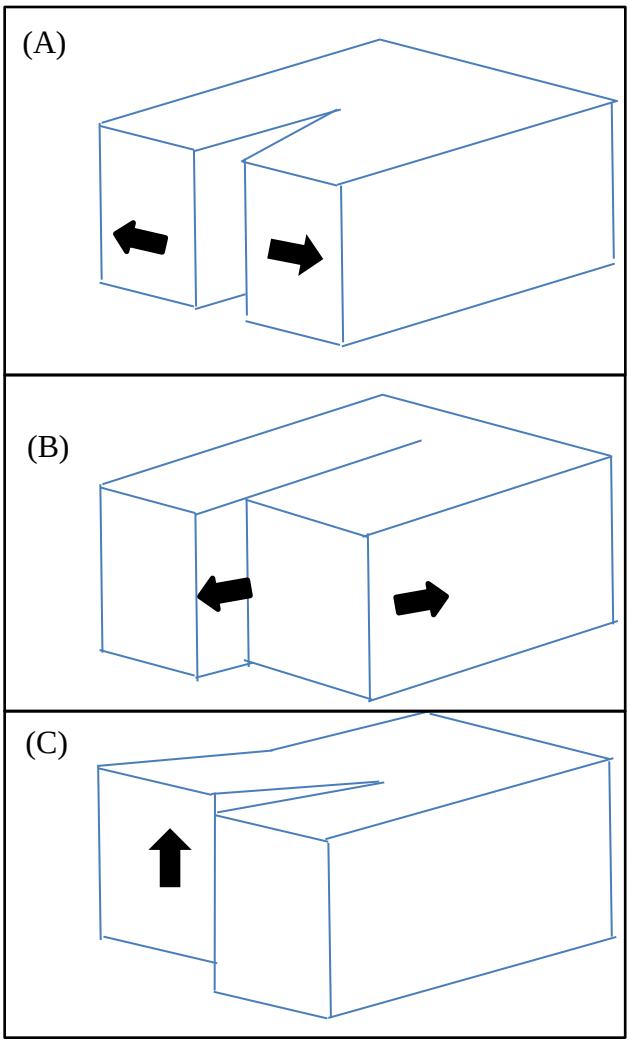

Figure 2.3 The three fundamental fracture modes: (A) Mode I opening perpendicular to the the fracture surface. (B) Mode II sliding parallel to the fracture surface (C) Mode III scissoring parallel to the fracture surface (Fjar, et al., 2008).

2.2.3.1 Tensile failure. Tensile failure occurs when a rock is subject to an effective tensile stress that exceeds a critical limit. This limit, which is viewed as a characteristic property of the rock, is referred as the tensile strength (T_0). Most rocks have a low tensile strength, as low as a few MPa (Kocher, et al., 2008). Tensile strength is sensitive to the existence of preexisting failures and the fracture planes often develop from preexisting failures, with right angle to the tensile stress direction. The specific stress condition at which tensile failure will first occur is referred to as tensile failure criterion and is given as (Jaeger and Cook, 1979):

$$\sigma_{\text{tensile}} = -T_0 \tag{33}$$

This failure is helpful to locate the failure surface. For isotropic rocks, the tensile strength will always be reached first by effective minimum principal stress (σ_3'), so that the tensile failure criterion is expressed as:

$$\sigma_3' = -T_0 \tag{34}$$

In a Mohr diagram, the tensile failure criterion represents the boundary between an unstable area and a stable area (Figure.2.4). Once the Mohr circle touches the tensile failure line, tensile failure will occur in the rock. The orientation of the failure plane is always perpendicular to σ_3'.

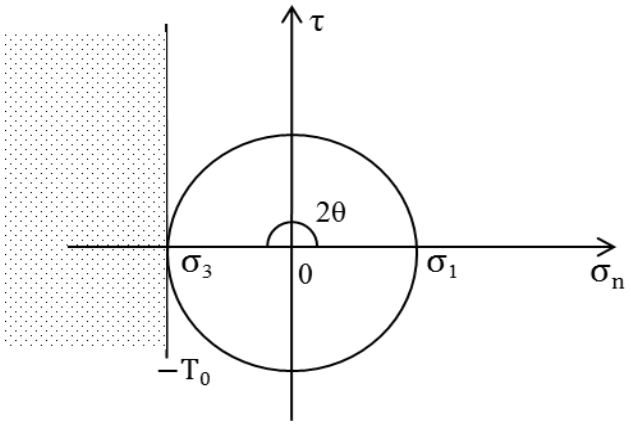

Figure 2.4 Tensile failure criterion and Mohr circle. Dark area stands for unstable area which tensile failure will occur.

2.2.3.2 Shear failure. Shear failure occurs in the rock when the shear stress on a specific plane inside the rock exceeds the strength of the material. The two parts of the shear failure plane will move relative to each other when shear failure occurs. This relative movement is resisted by the frictional force on the failure plane which depends

on the stress state of the plane. Thus, the critical shear stress (τ_{max}) which determines the occurrence of shear failure is assumed to be a function of the normal stress (σ_n) acting over the failure plane (Fjar, 2008):

$$\tau_{max} = f(\sigma_n) \tag{35}$$

In a Mohr stress diagram, this relationship is represented by a failure line. Shear failure occurs when the Mohr circle touches the failure line which indicates that the shear stress reaches τ_{max}. Considering that the Mohr circle is dependent on the principal stresses σ_1 and σ_3, the shear failure is governed by the two extreme principal stresses. Various shear failure criteria can be acquired by choosing different forms of the function in equation (40).

2.2.3.3 The Mohr-Coulomb failure criterion. The most widely used failure criterion to describe shear failure is the Mohr-Coulomb failure criterion (Fjar, 2008) which is based on rock mechanical testing under compression and the assumption that $f(\sigma_n)$ is a linear function. Coulomb postulated that shear failure on a surface will occur if the shear stress acting on that plane exceeds the cohesive strength of the rock plus the frictional resistance to movement (Coulomb, 1776).

$$|\tau| = S_0 + \mu\sigma_n \tag{36}$$

$$\mu = \tan\varphi \tag{37}$$

Where τ is the critical shear stress required for shear failure, σ_n is the normal stress, S_0 represents the rock cohesion, and μ is the coefficient of internal friction. This coefficient is also expressed by a constant $\tan\varphi$ where φ is called the angle of internal friction. Both S_0 and μ represent rock strength properties. For loose sand, these properties are related to sand grains and sand slope angles. For solid rocks, μ varies from 0.47 to 0.7 (Fjar, 2008) and for rocks in the upper crust, μ varies from 0.6 to 0.84 (Byerlee, 1978). In a Mohr stress diagram, the Mohr-Coulomb's failure criterion is represented by a straight line with slope angle ϕ. The cohesion (S) indicates the rock's resistance to shear fracture when the normal stress

becomes zero (Figure. 2.5). Based on Coulomb failure criterion, a certain plane in a rock can generate shear failure if the state of stress on that plan satisfies Equation (36).

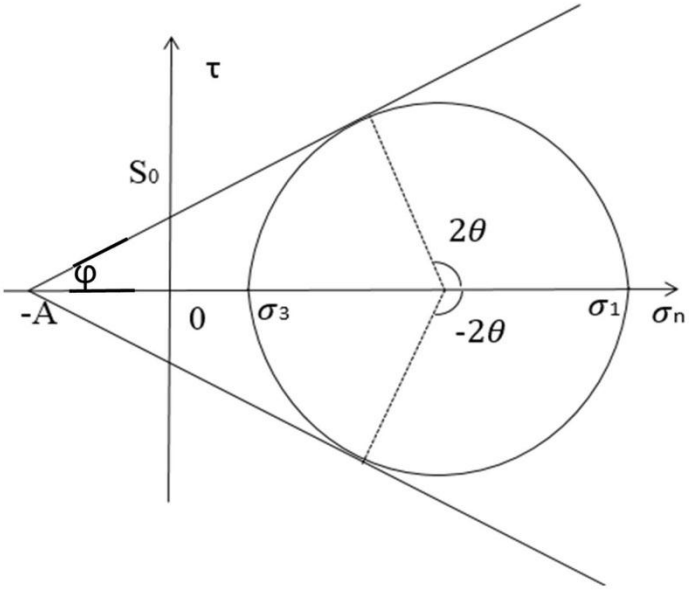

Figure 2.5 Shear failure criterion and Mohr circle. Failure will occur on a specific plane with angle θ to the maximum principal stress direction.

The angle 2θ indicates the point where the Mohr's circle touches the failure envelope and is termed the failure angle. The normal stress (σ_n) and shear stress (τ) of this point can be calculated by the maximum principal stress (σ_1) and minimum principal stress (σ_3):

$$\sigma_n = \frac{1}{2}(\sigma_1 + \sigma_3) + \frac{1}{2}(\sigma_1 - \sigma_3)\cos(2\theta) \tag{38}$$

$$\tau = \frac{1}{2}(\sigma_1 - \sigma_3)\sin(2\theta) \tag{39}$$

Since θ is the angle for the orientation of the failure plane, it is related to the internal friction angle φ as:

$$\theta = \frac{1}{2}\varphi + \frac{\pi}{4} \tag{40}$$

The possible range for θ is from 45° and 90° since the internal angle is between 0° and 90° (mostly the internal friction angle is around 30°). It is obvious that that the angle between the failure plane and the orientation of σ_1 is smaller than 45° (Figure 2.6). Most rocks establish shear fractures on planes oriented approximately thirty degrees to the direction of maximum principal stress (Byerlee, 1978, Fjar, 2008). The two surfaces in Figure 2.6 are referred as the conjugate shear planes or conjugate faults, which is a pair of faults formed during a compression test (Twiss and Moores, 1992). The failure planes of conjugate faults are bisected by the direction of maximum principal stress (σ_1), and have an acute angle of (π-2θ). The Mohr–Coulomb criterion indicates that the orientation of the shear failure plane is independent of the stress state of the rock if the internal angle is constant.

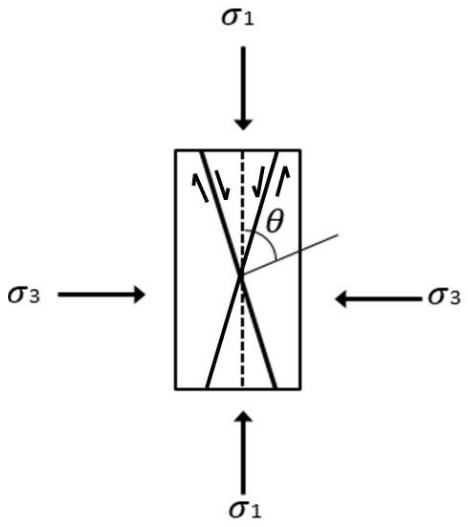

Figure 2.6 Orientation of the failure plane relative to the principal stresses. The thick solid line shows the failure plane.

2.3. THEORY OF FOLDING.

2.3.1. Single Layer Fold Theory. Single layer fold theory focuses on isolated layers buckling under compression. For a single layer designed with small perturbations of various initial wavelengths Biot's classical theory (1961) indicates that one of the wavelengths will develop with a greater enlargement factor than the others during folding. This wavelength is referred to as the dominant wavelength (λ_d). This theory is characterized by the viscosity difference between the embedded layer and the matrix (the material surrounding the layer). The competence contrast (R) between the single layer and the matrix is an important factor to the folding. It is defined as the ratio of viscosity between the layer and the matrix.

$$R = \frac{\mu(\text{layer})}{\mu(\text{matrix})} \tag{41}$$

For a viscous layer and a viscous matrix (in plane strain), the dominant wavelength only depends on the contrast (R) if both the gravity and the inertial effects in the rock are ignored. The thin-plate approximation for λ_d is

$$\frac{\lambda_d}{h} = 2\pi \left(\frac{\mu_L}{6\mu_M} \right)^{1/3} = 2\pi \left(\frac{R}{6} \right)^{1/3} \tag{42}$$

where h is the layer thickness, μ_L is the layer viscosity and μ_M is the matrix viscosity (see Figure 2.7). Free-slip contacts between the layer and the matrix are considered in this approximation. Based on the standard geometric classification, the folding layer geometry generated here is a parallel fold, which has constant thickness measured orthogonally across the layer (Price and Cosgrove, 1990). Equation (56) is accurate when the ratio R is bigger than 100. However, the accuracy decreases when R declines.

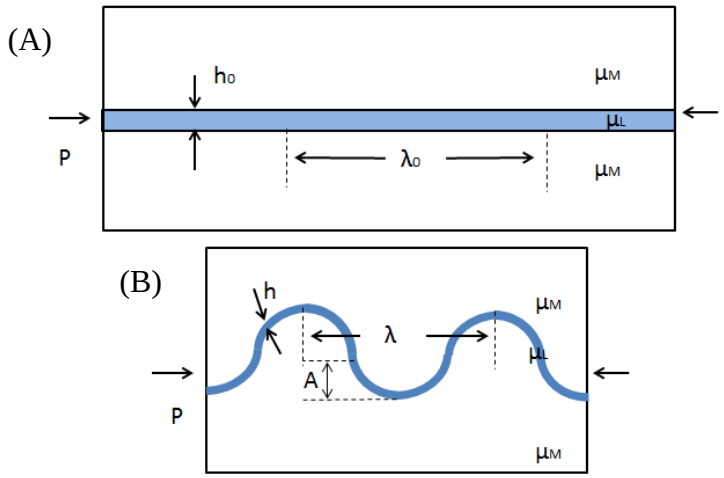

Figure 2.7 Description of terms used to determine folds development: (A) Initial state with h_0 as the initial embedded layer thickness and λ_0 as the initial embedded layer wavelength. μ_L and μ_M represent the embedded layer's viscosity and matrix's viscosity respectively. P is the load applied on the stiff layer; (B) After generating large amplitude A with shorter wavelength λ. h is the new layer thickness.

If the embedded layer features elastic material properties and the matrix material is viscous, the dominant wavelength is determined by the applied load on the boundary:

$$\frac{\lambda_d}{h} = \pi \left(\frac{E_L}{P(1-\nu_L^2)} \right) \tag{43}$$

where P represents the load applied on the stiff layer of the boundary, v_L is Poisson's ratio of the layer, and E_L is the elastic moduli of the layer. In this instance, the dominant wavelength no longer relates to the matrix viscosity.

The folding model with viscoelastic material properties of the folding layer and low viscous material properties of the matrix has been studied by Schmalholz and Podladchikov (2000). The ratio of the dominant wavelength predicted by equation (42) to the one predicted by equation (43) is referred as R_S. The ratio (R_S) is found to be instrumental in determining whether or not the folding is controlled by either viscous or elastic properties. If R_S is smaller than 1, equation (42) is more accurate. If it is larger than 1, Equation (43) should be used to calculate the dominant wavelength.

The development of the single layer with respect to different values of R under the same boundary conditions has been studied by Ramberg (1960). Ramberg shows that the layers appear to develop different degrees of folding as the viscosity contrasts changes.

When considering the effect of layer-parallel shortening, the folds with the greatest cumulative amplification is a function of shortening. In this instance, the wavelength is known as the preferred wavelength (λ_p) (Price and Cosgrove, 1990). The approximate expression for λ_p is

$$\frac{\lambda_p}{h} = 2\pi \left(\frac{\mu_L}{6\mu_M} \frac{S_x^2(S_x^2+1)}{2} \right)^{1/3} \tag{44}$$

where h is the final thickness of the layer. S_x represents the stretch in the horizontal direction. The stretch is the ratio of final length to initial length on line element. If L is finial wavelength and L_0 is initial wavelength, the horizontal stretch is given by:

$$S_x = \frac{L}{L_0} \tag{45}$$

2.3.2. Theory of Finite Amplitude Single-layer Folds. The conclusion that amplitude increases with time and shortening is applicable only for infinitesimal amplitudes. A higher waveform influences the fold shape and limits the growth rate of the waveform. Johnson and Fletcher have developed a simple modification of the previous theory for single layers (Price and Cosgrove, 1990). The modification considers the fact that stretching of the competent layer would occur and slow the fold growth in the folding development. A solution based on the strain relating the further development of the fold amplitude is given by (Johnson and Fletcher, 1994):

$$A(\varepsilon_l) = A_0 e^{(1+\alpha_0)\varepsilon_l} \left(\frac{\hat{L}_{arc0}}{\hat{L}_{arc}} \right)^{\alpha_0} \tag{46}$$

where A the is amplitude and A_0 is the initial amplitude. $\hat{L}_{arc}$ is the fold arc length normalized over the fold wavelength, ε_l is the logarithmic strain defined as $\ln(\lambda_0/\lambda)$ and, α_0 is the initial growth rate. Schmalholz and Podladchikov (2000) compare the small amplitude theory (thin-plate theory) and the predictions of finite amplitude theory. With an initial perturbation of the dominant wavelength ($\lambda_d/h = 12.75$) and an initial amplitude ($A_0/h = 0.02$), the finite amplitude theory fits closely to numerical simulations of buckling.

2.3.3. Stress Distribution. The stress orientations and magnitudes vary in space and time during the buckling progress. Dieterich and Carter (1969) have used the finite element method to study a two-dimensional large amplitude fold. A viscous layer in a less viscous matrix is compressed to analyze the stress history of folding. Figure 2.8 shows the orientation of maximum principal stress σ_1 at different stages. During the early periods of buckling, the maximum principal stress within the folding layer is parallel to the layer having large magnitudes. As the fold grows, the orientation of σ_1 rotates to a large angle to the folding layer with a decrease in the stress magnitude. In the fold crest area, the orientation of σ_1 is parallel to the layer on the concave sides of folds because of the layer-parallel shortening, and the magnitude of σ_1 decreases with buckling. On the convex sides, the orientation of σ_1 is approximately perpendicular to the layer as a result of layer-parallel elongation. Their result shows that low magnitude tensile stress is expected to develop at the outer part of the fold crest.

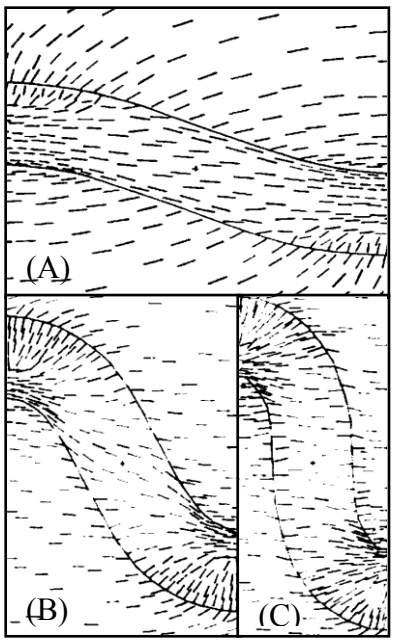

Figure 2.8 Orientations of maximum principal stress in the layer and matrix at different amounts of shortening. (A) 20% shortening. (B) 60% shortening. (C) 80% shortening (after Dieterich and Carter, 1969).

2.3.4. Strain Distribution. Deformation during folding leads to variable strain states throughout the layer. It is known that buckling of a competent layer, embedded in an incompetent matrix, produces parallel folds (fold layers which maintain parallel shape when buckled) (Price, 1966). For parallel folds, there are two classic theories to describe the strain distribution: flexural flow theory and tangential-longitudinal strain theory. Both of them are able to produce parallel folds with no change in orthogonal thickness (perpendicular distance between the inner and outer fold surfaces) (Ramsay, 1967). These two theories are described in most structural geology text book (e.g. Price and Cosgrove, 1994; Twiss and Moores, 2007; Fossen, 2010).

2.3.4.1 Flexural flow theory. Flexural flow theory demonstrates that anisotropic viscosity in rocks leads to flexural flow and the strain distribution is governed by homogeneous but anisotropic layers buckling with bedding-parallel slip (Johnson and Fletcher, 1994). There is no strain at the layer crest and the maximum layer-parallel shear strain is developed at the middle of the limb (see figure 2.9). For any surface parallel to the layer, the length remains unchanged and the shear strain is zero at the crest and

increases to a maximum at the inflexion point. The central surface is parallel to the fold shape.

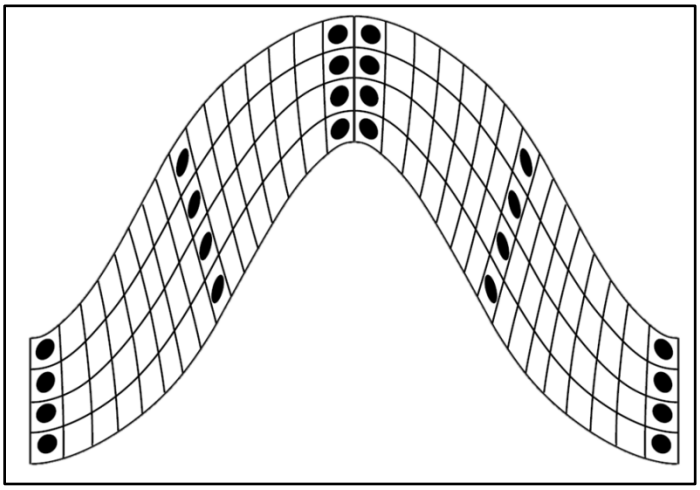

Figure 2.9 Deflections of originally square gridlines and strain pattern (black ellipses) in parallel folds by flexural flow (after Johnson and Fletcher, 1994).

2.3.4.2 Tangential longitudinal strain. Tangential longitudinal strain is characterized by tangential, layer-parallel extension at outer crest arc and tangential, layer-parallel compression at the inner crest arc. The folding layer thickness is constant and the principal strains are parallel and perpendicular to the layering (Figure 2.10). The surface near the center of the layer characterized by zero principal stain is termed as the neutral surface and it separates layer-parallel extension from layer-parallel compression in the hinge zone (Ramsay, 1967). Unlike the center surface in flexural flow folds, the neutral surface fails to divide the folding layer into two parallel fold halves. The migration of the neutral surface in the hinge zone indicates the neutral surface's non-parallelism to the outer and inner fold surfaces. The tangential longitudinal strain theory illustrates that the layer-perpendicular tension fractures on the convex side of the fold crest, i.e. on the upper side of the neutral surface, can be generated by layer-parallel shortening.

The tangential-longitudinal strain is successfully approximated in laboratory experiments (Hudleston, 1973) and corresponds with most strain patterns in natural folds (Shimamoto and Hara, 1976). Finite element analysis of stress and strain pattern shows that this theory is the dominant mechanism for viscous single and multilayer folds (Dieterich and Carter, 1969; Hudleston, 1973.). However, this theory is not perfect to explain the area change in the hinge regions in nature (Hudleston and Holst, 1984; Bobillo-Ares and Bastida., 2000).

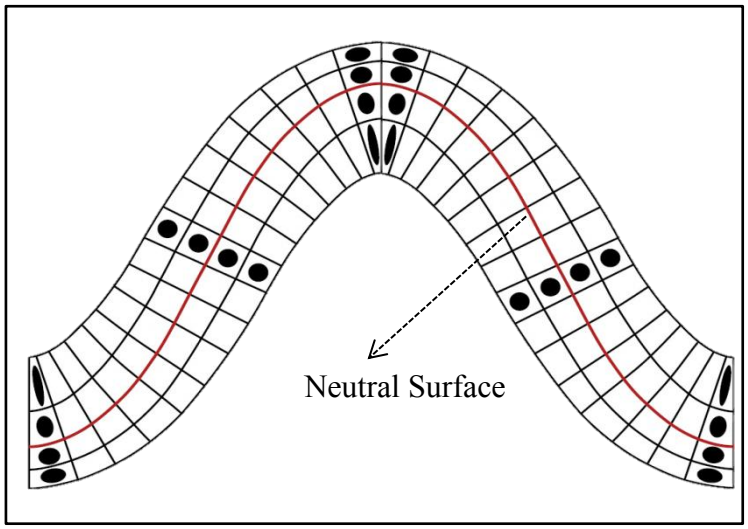

Figure 2.10 Deflections of originally square gridlines and strain pattern (black ellipses) in parallel folds by tangential longitudinal strain. The red line represents the neutral surface (after Johnson and Fletcher, 1994).

2.4. MATHEMATICAL DESCRIPTION OF FOLDING.

2.4.1. Differential Equation of Single Layer Folding in Elastic Medium. By analyzing the forces acting on a very small element, the differential equation which governs the deflection of a single layer folding in elastic medium can be expressed as (Johnson and Fletcher, 1994).:

$$\frac{dM}{dx} + P_L \frac{dw}{dx} - Q = 0 \tag{47}$$

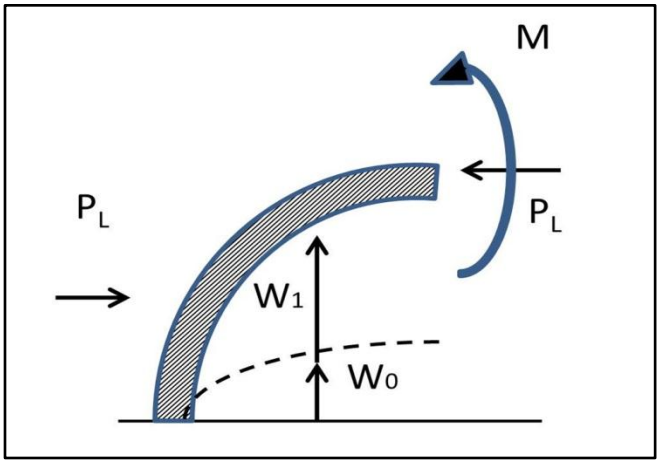

Figure 2.11 Buckling of a single layer (after Johnson and Fletcher, 1994).

where P_L represent the axial load, Q represent shear force and M represent bending moments (see Figure 2.11). The deflection (w) is used to describe the mathematical formula of folding. Combined with the theory of elasticity, the differential equation of folding in elastic medium can be expressed as (Johnson and Fletcher, 1994):

$$M = \frac{IE}{1-\nu^2}\left(\frac{d^2w}{dx^2}\right) \tag{48}$$

$$I\frac{E}{1-\nu^2}\frac{d^4w}{dx^4} + P\frac{d^2w}{dx^2} + \frac{2\pi hE_0}{\lambda_0\left(1-\nu_0^2\right)}w = 0 \tag{49}$$

where I is the moment of inertia, λ_0 is the wavelength of the initial perturbation. E is the Young's modulus and ν is the Poisson's ratio for the folding layer. E_0 is the Young's modulus and ν_0 is the Poisson's ratio for the matrix. The single layer thickness is expressed as h. The deflection w can be expressed as

$$w = w_0 + w_1 \tag{50}$$

where w_1 is the deflection caused by the axial load, and w_0 is the deflection of the folding layer in the unloaded state and can be calculated as:

$$w_0 = \lambda_0 \sin\left(\frac{2\pi x}{\lambda_0}\right) \tag{51}$$

The entire deflection equation can now be rewritten as

$$I\frac{E}{1-\nu^2}\frac{d^4 w_1}{dx^4} + P\frac{d^2(w_1 + w_0)}{dx^2} + \frac{2\pi h}{\lambda_0}\frac{E_0}{1-\nu_0^2}w_1 = 0 \tag{52}$$

2.4.2. Differential Equation of Single Layer Folding in Viscous Medium. For a viscous medium, the stress is not only dependent on the applied strain but also on the strain rate. If sufficient time is allowed, even a small load can produce large folds in viscous material layers. The coefficient of viscosity for a viscous material is defined as

$$\eta = \frac{\sigma_s}{\dot{\varepsilon}} \tag{53}$$

For a viscous material, the bending moment is (Johnson and Fletcher, 1994):

$$M = 4\eta\frac{\partial}{\partial t}\left(I\frac{d^2 w_1}{\partial x^2}\right) \tag{54}$$

The differential equation for the deflection of a viscous layer bedding in a viscous matrix given by Johnson and Fletcher (1994) is :

$$4\eta I \frac{\partial^5 w_1}{\partial x^4 \partial t} + P \frac{\partial^2 (w_1 + w_0)}{\partial x^2} + \frac{8\eta_0 \pi h}{\lambda_0} \frac{\partial w_1}{\partial t} = 0 \tag{55}$$

or

$$\frac{4\eta I}{P} \frac{\partial^5 w_1}{\partial x^4 \partial t} + \frac{\partial^2 w_1}{\partial x^2} + \frac{8\eta_0 \pi h}{P\lambda_0} \frac{\partial w_1}{\partial t} = \frac{\partial^2 w_0}{\partial x^2} \tag{56}$$

where η is the coefficient of viscosity under the axial load, and η_0 is the coefficient of viscosity in the unloaded state.

2.5. CONSTITUTIVE MODEL FOR VISCOELASTIC FOLDING

In order to solve equation 70 numerically, a constitutive model relating stress and strain rate need to be defined for the viscoelastic medium.

2.5.1. Navier - Stokes Equations for Slow Linear Viscous Flow. As many folds display a cylindrical form (Dick and Sinton, 1979), a two-dimensional (2D) numerical model under plane-strain loading is applicable to study their formation. This model consists of an incompressible material in an x-z coordinate system; the z axis is vertical and mass is conserved everywhere. The stain normal to the x-z plane, ε_y, and the shear stain ε_{xy} and ε_{yz} , are assumed to be zero**.** The displacements of all points in the model are assumed to be parallel to a give plane.

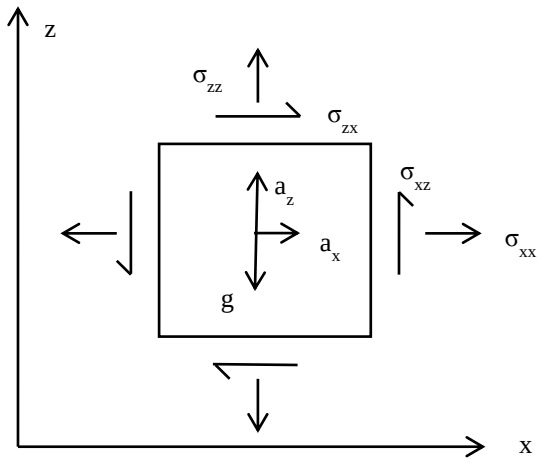

Figure 2.12 Stresses and accelerations acting on a basic fluid element.

Considering the incompressibility of the material, the development of folding is assumed as a constant-volume deformation progress and the density (ρ) at any point in the model remains constant. In order to describe the buckling process numerically the conservation equations for slow, incompressible viscous flow need to be solved. The conservation of mass at a point in a continuum can be expressed as

$$\frac{\partial \rho}{\partial t} + \rho \left(\frac{\partial v_x}{\partial x} + \frac{\partial v_z}{\partial z} \right) = 0 \tag{57}$$

where v_x and v_y are the velocities along the x and z axes respectively.

Since the density is independent of space and time, the continuity equation can be arranged as

$$\frac{\partial \rho}{\partial t} = 0 \tag{58}$$

$$\frac{\partial v_x}{\partial x} + \frac{\partial v_z}{\partial z} = 0 \tag{59}$$

The conservation of momentum is given by Newton's second law of motion (considering gravity):

$$\frac{\partial \sigma_{xx}}{\partial x} + \frac{\partial \sigma_{zx}}{\partial z} + \rho g_x = \rho a_x \tag{60}$$

$$\frac{\partial \sigma_{zz}}{\partial z} + \frac{\partial \sigma_{xz}}{\partial x} + \rho g_z = \rho a_z \tag{61}$$

where a_x and a_z represent the accelerations at x and z axes respectively. Gravitational acceleration has been considered, where g_x and g_z represent the gravitational accelerations along the x and z axes respectively.

$$g_x = 0 \tag{62}$$

$$g_z = g \tag{63}$$

Because the strain rates of geologic progress are as slow as 10^{-12} s^{-1} (Karato, 2008), a steady flow condition can be applied:

$$\frac{\partial v_x}{\partial t} = \frac{\partial v_z}{\partial t} = 0 \tag{64}$$

$$a_x = v_x \frac{\partial v_x}{\partial x} + v_z \frac{\partial v_x}{\partial z} + \frac{\partial v_x}{\partial t} = v_x \frac{\partial v_x}{\partial x} + v_z \frac{\partial v_x}{\partial z} \tag{65}$$

$$a_z = v_x \frac{\partial v_z}{\partial x} + v_z \frac{\partial v_z}{\partial z} + \frac{\partial v_z}{\partial t} = v_x \frac{\partial v_z}{\partial x} + v_z \frac{\partial v_z}{\partial z} \tag{66}$$

Pore pressure within a petroleum reservoir rock is very important because the entire reservoir is treated as a porous, fluid-filled rock system. Considering pore pressure in equations (60) to (66), the equation of motion at each point of the model can be arranged as

$$\frac{\partial(\sigma_{xx} - P_p)}{\partial x} + \frac{\partial \sigma_{zx}}{\partial z} = \rho(v_x \frac{\partial v_x}{\partial x} + v_z \frac{\partial v_x}{\partial z}) \tag{67}$$

$$\frac{\partial(\sigma_{zz} - P_p)}{\partial z} + \frac{\partial \sigma_{xz}}{\partial x} - \rho g = \rho(v_x \frac{\partial v_z}{\partial x} + v_z \frac{\partial v_z}{\partial z}) \tag{68}$$

The constitutive equations are used to describe the mechanical behavior of a constant-volume deformation of viscoelastic material. They can be derived from the relationship between stress and velocity. In general, this relationship can be expressed as:

$$\sigma_{xx} = -P - \frac{2}{3}\mu(\frac{\partial v_x}{\partial x} + \frac{\partial v_z}{\partial z}) + 2\mu \frac{\partial v_x}{\partial x} \tag{69}$$

$$\sigma_{zz} = -P - \frac{2}{3}\mu\left(\frac{\partial v_x}{\partial x} + \frac{\partial v_z}{\partial z}\right) + 2\mu\frac{\partial v_z}{\partial z} \tag{70}$$

$$\sigma_{xz} = \mu\left(\frac{\partial v_x}{\partial z} + \frac{\partial v_z}{\partial x}\right) = \sigma_{zx} \tag{71}$$

where P is the static pressure or negative mean normal stress, and expressed as

$$P = -\frac{\sigma_{xx} + \sigma_{zz}}{2} \tag{72}$$

Accounting for pore pressure, this relationship can be written as:

$$\sigma_{xx} - P_P = -P - \frac{2}{3}\mu\left(\frac{\partial v_x}{\partial x} + \frac{\partial v_z}{\partial z}\right) + 2\mu\frac{\partial v_x}{\partial x} \tag{73}$$

$$\sigma_{zz} - P_P = -P - \frac{2}{3}\mu\left(\frac{\partial v_x}{\partial x} + \frac{\partial v_z}{\partial z}\right) + 2\mu\frac{\partial v_z}{\partial z} \tag{74}$$

$$\sigma_{xz} = \sigma_{zx} = \mu\left(\frac{\partial v_x}{\partial z} + \frac{\partial v_z}{\partial x}\right) \tag{75}$$

The Navier-Stokes equations are derived by combining the equation of motion (equation 67 and 68) and the rheological equations (equation 73, 74 and 75):

$$-\frac{\partial P}{\partial x} + \frac{1}{3}\mu\frac{\partial^2 v_z}{\partial z \partial x} + \frac{4}{3}\mu\frac{\partial^2 v_x}{\partial x^2} + \mu\frac{\partial^2 v_x}{\partial z^2} = \rho\left(v_x\frac{\partial v_x}{\partial x} + v_z\frac{\partial v_x}{\partial z}\right) \tag{76}$$

$$-\rho g - \frac{\partial P}{\partial z} + \frac{1}{3}\mu\frac{\partial^2 v_x}{\partial z \partial x} + \frac{4}{3}\mu\frac{\partial^2 v_z}{\partial z^2} + \mu\frac{\partial^2 v_z}{\partial x^2} = \rho\left(v_x\frac{\partial v_z}{\partial x} + v_z\frac{\partial v_z}{\partial z}\right) \tag{77}$$

They can be rearranged as:

$$-\frac{\partial P}{\partial x}+\frac{1}{3}\mu\frac{\partial}{\partial x}(\frac{\partial v_z}{\partial z}+\frac{\partial v_x}{\partial x})+\mu(\frac{\partial^2 v_x}{\partial x^2}+\frac{\partial^2 v_x}{\partial z^2})=\rho(v_x\frac{\partial v_x}{\partial x}+v_z\frac{\partial v_x}{\partial z}) \tag{78}$$

$$-\rho g-\frac{\partial P}{\partial z}+\frac{1}{3}\mu\frac{\partial}{\partial z}(\frac{\partial v_x}{\partial x}+\frac{\partial v_z}{\partial z})+\mu(\frac{\partial^2 v_z}{\partial z^2}+\frac{\partial^2 v_z}{\partial x^2})=\rho(v_x\frac{\partial v_z}{\partial x}+v_z\frac{\partial v_z}{\partial z}) \tag{79}$$

Substituting equation 58 into these results in:

$$-\frac{\partial P}{\partial x}+\mu(\frac{\partial^2 v_x}{\partial x^2}+\frac{\partial^2 v_x}{\partial z^2})=\rho(v_x\frac{\partial v_x}{\partial x}+v_z\frac{\partial v_x}{\partial z}) \tag{80}$$

$$-\rho g-\frac{\partial P}{\partial z}+\mu(\frac{\partial^2 v_z}{\partial z^2}+\frac{\partial^2 v_z}{\partial x^2})=\rho(v_x\frac{\partial v_z}{\partial x}+v_z\frac{\partial v_z}{\partial z}) \tag{81}$$

These are the Navier-Stokes equations for steady, in-plane flow of an incompressible, linear viscous fluid.

2.5.2. Governing Equations for Slow Linear Viscous Flow. The right hand sides of the conservation of momentum equations (equations 67 and 68) are assumed to be negligible as the natural geological deformation rates are very small. Thus these equations are reduced to:

$$\frac{\partial(\sigma_{xx}-P_p)}{\partial x}+\frac{\partial(\sigma_{zx}-P_p)}{\partial z}=0 \tag{82}$$

$$\frac{\partial(\sigma_{zz}-P_p)}{\partial z}+\frac{\partial(\sigma_{xz}-P_p)}{\partial x}-\rho g=0 \tag{83}$$

The sum of equations (95) and (96) is zero and expressed as:

$$\frac{\partial(\sigma_{xx}-P_p)}{\partial x}+\frac{\partial(\sigma_{zx}-P_p)}{\partial z}+\frac{\partial(\sigma_{zz}-P_p)}{\partial z}+\frac{\partial(\sigma_{xz}-P_p)}{\partial x}-\rho g=0 \tag{84}$$

Substituting equation 72, 73 and 74 into equation 83, the governing equations for this numerical model can be expressed as:

$$\frac{\partial(2\mu\frac{\partial v_x}{\partial x}-P)}{\partial x}+\mu\frac{\partial\left(\frac{\partial v_x}{\partial z}+\frac{\partial v_z}{\partial x}\right)}{\partial z}+\frac{\partial(2\mu\frac{\partial v_z}{\partial z}-P)}{\partial z}+\mu\frac{\partial\left(\frac{\partial v_x}{\partial z}+\frac{\partial v_z}{\partial x}\right)}{\partial x}-\rho g=0 \tag{85}$$

Thus

$$\frac{\partial P}{\partial x}+\frac{\partial P}{\partial z}+\rho g=\mu(2\frac{\partial^2 v_x}{\partial x^2}+2\frac{\partial^2 v_z}{\partial z^2}+\frac{\partial^2 v_x}{\partial z^2}+\frac{\partial^2 v_z}{\partial x^2}+\frac{\partial^2 v_z}{\partial x\partial z}+\frac{\partial^2 v_x}{\partial z\partial x}) \tag{86}$$

To simplify, the governing equation 85 is rearranged as:

$$\frac{\partial P}{\partial x}+\frac{\partial P}{\partial z}+\rho g=\mu(\frac{\partial^2 v_x}{\partial x^2}+\frac{\partial^2 v_z}{\partial z^2}+\frac{\partial^2 v_x}{\partial z^2}+\frac{\partial^2 v_z}{\partial x^2})+\mu\left(\frac{\partial}{z}(\frac{\partial v_x}{\partial x}+\frac{\partial v_z}{\partial z})+\frac{\partial}{x}(\frac{\partial v_x}{\partial x}+\frac{\partial v_z}{\partial z})\right) \tag{87}$$

Substituting equation (58) into this result, the final differential equation is

$$\frac{\partial P}{\partial x}+\frac{\partial P}{\partial z}+\rho g=\mu(\frac{\partial^2 v_x}{\partial x^2}+\frac{\partial^2 v_z}{\partial z^2}+\frac{\partial^2 v_x}{\partial z^2}+\frac{\partial^2 v_z}{\partial x^2}) \tag{88}$$

This is the governing equation for steady, in-plane flow of an incompressible, linear viscous fluid.

3. MODELING METHOD

3.1. FINITE ELEMENT METHOD

The finite element method (FEM) is a general and powerful numerical method to obtain approximate solutions of complex problems that involve complicated geometry and boundary conditions. This method was firstly developed to study air-frame structures stability (Clough, 1960) and was extended to other engineering field later.

3.1.1. Partial Differential Equations and Numerical Methods. Most of the governing equations can be represented by partial differential equations. A partial differential equation （PDE） is defined as an equation including an unknown function of two or more variables and certain of its partial derivatives. The governing PDEs are viewed as the mathematical description of continuous physical phenomenon in which a dependent variable is a function of more than one independent variable. For the steady, in-plane flow of an incompressible, linear viscous fluid, the governing PDEs are presented in Chapter 2.

Unlike the derivation of the governing equations which is not excessively difficult, the exact solutions are difficult to obtain due to complex geometries and complex boundary conditions. Thus, numerical methods are introduced to achieve approximate solutions. The basic idea in a typical numerical method for solving the governing PDEs is to discretize the given continuous problem into subdomains or elements to obtain a discrete system, containing equations with unknowns that can be solved by computer.

3.1.2. Finite Element Method and ABAQUS™. The finite element method (FEM) offers a numerical approximation method to solve for the governing PDEs in problems with complicated geometries, loadings and material properties where analytical solutions are impossible to achieve. The continuum of the object is divided into an equivalent system with finite small units (elements) which are interconnected at points (nodes) and boundary lines. The characteristic relationship between force $\boldsymbol{q}$ and displacements $\boldsymbol{u}$ will always be of the form (Zienkiewicz, et al., 2005):

$$q^e = K^e u^e + f^e \tag{89}$$

where K^e is the element stiffness matrix, f^e is the element loading, and q^e is the internal force at the element nodes.

By inducing the shape functions, N_a, prescribed in terms of independent variables, the displacements u at any point within the element be approximated as a column vector (Zienkiewicz, et al., 2005):

$$\vec{u} \approx \hat{u} = \sum_a \vec{N}_a \tilde{u}_a^e \tag{90}$$

The shape functions are expressed as polynomial forms of the independent variables and derived to satisfy certain conditions at the nodes. Combing the equations for all the elements in the discrete system, a global matrix equation system of the physical problem is obtained if the approximating equations are in integral form. The boundary conditions, which are the specified field values on the boundaries, are inserted into the final assembled global matrix. Thus the numerical results, such as the stress history of folding layers in this study, can be solved from the resulting equation system. The theoretical concepts and methods for FEM can be found in extensive detail in standard text books (e.g. Zienkiewicz, et al., 2005; Bathe, 2008; Dhatt and Touzot, 2012).

The FE analysis (FEA) in this research is performed using the general-purpose finite element code, ABAQUS/Standard. ABAQUS™ is a commercial program that is capable and suitable for analyzing and solving geotechnical problems involving two- and three-dimensional models (e.g., Smart, et al., 2004, 2010a, 2010b). ABAQUS™ is efficient for simulating the complicated physical response of rocks due to nonlinear material behavior and complex geometry. The built-in material library consists of several constitutive material models that are capable to simulate different rock behavior, including liner elastic models to viscoelastic models. ABAQUS™ also has automatic and adaptive choice of time incrimination which provides accurate stress evolution during folding development (Dassault, 2011).

3.2. MATERIAL PROPERTIES

For a realistic simulation of in-situ stresses in crustal rocks appropriate material properties need to be introduced. For the viscoelastic simulation in ABAQUS^{TM} using a *SOILS, CONSOLIDATION analysis including rock creep behavior the following material properties need to be defined: (a) Young's Modulus, (b) Poisson's Ratio, (c) viscosity, (d) density, (e) permeability, and (f) porosity.

In the presented model, standard values for sedimentary rocks' Poisson's Ratio (ν=0.25 for all rocks considered) are chosen.

In many sedimentary basins an increase in depth is associated with a reduction in of porosity, and permeability and an increase in density (Chapman, 2000). This behavior is the result of mechanical compaction, and the duration and history of post-depositional events (Twiss and Moores, 2007). Plumley (1980) suggests that the increasing effective stress leads to rock compaction along pore volume reduction and formation fluid movement. The rate of porosity change varies in different types of rock. Medina and Rupp's (2011) study on porosity values obtained from geophysical logs and porosity values form core analyses in different areas in U.S.A. gives the following porosity-depth and low permeability-porosity relationship:

$$\phi(z) = 16.39\ e^{-0.00039\ d} \tag{91}$$

$$k = 7.583\times10^{-17} e^{0.283\ \phi} = 7.583\times10^{-17} e^{4.63\ e^{-0.00039\ d}} \tag{92}$$

where ϕ is the porosity (%), d is the depth in meters, and k is permeability in m^2. For example, permeability at 1000 meters depth is 1.75×10^{-15} m^2.

Furthermore, isotropic permeability is uncommon in most sedimentary rocks. Permeability typically varies significantly between the vertical and horizontal planes within a formation. This variation in permeability in different directions is known as anisotropic permeability. Based on small-scale probe permeability measurements on differently oriented faces of highly cemented sandstones, the ratio between vertical permeability and horizontal permeability is discovered to vary between 0.1 and 1.0

(Chapman, 2000). For material in this numerical model, the ratio is assumed to be 0.2 in the model material.

The specific gravity of soil/rock solids is introduced here to express the dry density of rock. The specific gravity of solids (G_s) is defined as the mass of a volume of material over the mass of the same volume of water. Dry density used in the model can be derived as

$$\rho_d = G_s \rho_w (1-\phi) = G_s \rho_w (1 - 0.1639 \times e^{-0.00039d}) \tag{93}$$

where G_s is 2.75 (Turcotte and Schubert, 2002).

The relation between the elastic moduli and the seismic waves' velocity enables the Young's Modulus to be calculated by S-wave velocity if the rock density is known. For a homogeneous isotropic rock, the Young's Modulus is estimated using the following equation (Fjar et al., 2008):

$$E = 2V_S^2 (1+\nu)\rho_d \tag{94}$$

where E is the Young's Modulus (Pa) , Vs is S-wave velocity (m/s) and ν is Possion's ratio. Thus, the rock Young's Modulus has a liner relation with dry density with a constant S-wave velocity and Possion's ratio. The S-wave velocity is assigned as 400m/s for the rock in the matrix, which is typical for saturated sandstone (Buchmann, 2007).

As many fold and buckling processes are the result of pressure solution creep during compressional loading (Dick and Sinton, 1979; Turcotte and Schubert, 2002), viscoelastic material response is considered in the numerical models. Pressure solution creep follows the linear slow viscous flow relationship derived in chapter 2.1.6. Rocks behave as a so-called Newtonian fluid and the stress strain relationship is given by equation:

$$\sigma = 2\mu\dot{\varepsilon} \tag{95}$$

where σ is stress, μ is viscosity and $\dot{\varepsilon}$ is the strain rate. The modeling approach is utilizing geological strain rate varying between 10^{-12} and 10^{-15} s^{-1} (Watts, 1987; Kocher, et al., 2006).

The visco-elastic material is used to predict the unrecoverable behavior in rock deformation; it has been widely used in the modeling of folding (e.g. Biot, 1959; Chapple, 1968; Dieterich and Carter, 1969; Williams, et al., 1978).

As described in chapter 2.3 another important parameter is the competence contrast R between the folding layer and the matrix, where competence may be described as a measure of material strength (Chapple, 1969). For the viscoelastic materials simulated here, both the viscosity ratio and the elastic strength ratio define the competence contrast because they control the viscous part and the elastic part of deformation, respectively. A constant contrast R is assumed throughout the entire model and is defined as

$$R = \frac{E_{folding}}{E_{matrix}} = \frac{\mu_{folding}}{\mu_{matrix}} \tag{96}$$

To produce a folding layer with constant orthogonal thickness (perpendicular distance between the inner and outer fold surfaces), the initial R value is chosen as 42 in these numerical models (Zhang, et al., 1996).

All of the material properties of the numerical model are listed in Table 3.1.

Table 3.1 Material prosperities of layer and matrix

Properties	Folding Layer	Matrix
Specific Gravity	2.75	2.75
Viscosity	10^{19} [Pa s]	$10^{19} / R$ [Pa s]
Young's Modulus	$23(1-0.1639e^{-0.00039z})$ [GPa]	$(23/R)(1-0.1639e^{-0.00039z})$ [GPa]
Poisson Ratio	0.25	0.25
Permeability (at 1000m)	1.75×10^{-15} [m^2]	1.75×10^{-15} [m^2]
Strain Rate	10^{-12} [s^{-1}]	10^{-12} [s^{-1}]

In order to simulate realistic effective stresses in an ABAQUS^{TM} *SOILS analysis, initial pore pressure and water saturation have to be defined. Water saturation is assumed to be 1 throughout the model domain and pore pressure is assumed to be hydrostatic. At depth h, the hydrostatic pressure is equal to the weight of a pure water column from sea level with the water density (ρ_w)

$$P_P = \int_0^z g\,\rho_w\,dz \tag{97}$$

The pore pressure can be predicted to increase to a certain number during the fold development due to horizontal compression which is a kind of tectonic loading.

3.3. REALISTIC STRESS MAGNITUDES: PRE-STRESSING APPROACH.

The rock in nature is in equilibrium with all loads present and this state of equilibrium is represented by the in-situ state of stress (Twiss and Moores, 2007). For a numerical simulation of the kinematic behavior of a tectonic system such as folding, it is insufficient to only apply the boundary conditions during the shortening period without considering the initial equilibrium state of stress. Thus, defining an appropriate initial state of stress and then applying appropriate boundary conditions on the pre-stressed

model is necessary for a finite element model to simulate realistic stress magnitudes. For all the numerical models in this study, gravity is applied both before and during layer-parallel shortening, in order to approximate a realistic in-situ stress state in the model and counteract excess elastic compaction in rock layers. This is termed as pre-stressing (Buchmann, 2008).

In the first step, only the gravitational acceleration load and appropriate boundary conditions without shortening are utilized (see Figure 3.1A). For this 2-D model, all the boundaries are constrained and only allow in-plane displacements except for the top boundary, which remains unconstrained and acts as a free surface. The pore pressure in the pre-stressing step is assumed to be hydrostatic. As a result, an elastic compaction in the vertical direction and the gravity-induced state of stress, which changes with depth, are obtained. The vertical compaction is a function of the model depth and rock density with a constant Young's Modulus. For a numerical model with 1000 meters depth and rock density as described in the chapter 3.2, the vertical displacement is as much as 52 meters. However, the vertical elastic compaction due to gravity is neither realistic nor necessary because of the initial state of stress is in equilibrium with the gravity load acting as a body force, resulting in no vertical displacement.

In the second step, the resulting stress state from the gravitational compaction is applied to the model as an initial state of stress. The second step is a tectonic pre-stressing step with gravity and layer-parallel shortening as boundary conditions to simulate the stress change during single-layer folding. Because of the initial state of stress generated during the first step, realistic stress magnitudes related to depth have been established and excess elastic compaction along the vertical direction has been counteracted before buckling.

By combing the two steps, it is possible to simulate realistic stress history during the folding and correct the vertical displacements caused by the rock gravity using pre-existing state of stress. The simulation results can not only reveal the stress evolution during buckling, but also be compared to geological observations.

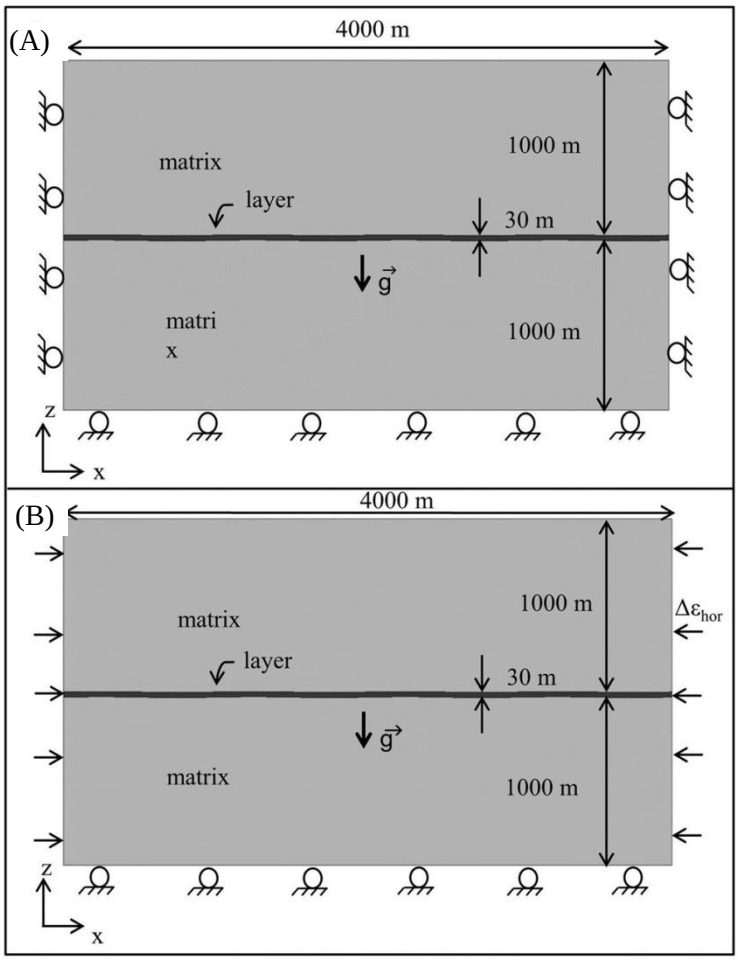

Figure 3.1 Boundary conditions for 2D numerical models. A) Gravitational pre-stressing numerical model where only gravity is acting and the model sides are constrained such that only in-plane displacements are allowed (rollers). B) Numerical model with a constant tectonic strain ε_{hor} added after reaching gravitational equilibrium.

3.4. MODEL GEOMETRY AND BOUNDARY CONDITIONS

The geometry of the numerical model consists of a central folding layer with periodic, small perturbations embedded within the matrix. As shown in Figure 3.1, the length of the folding layer is 4000 meters and the thickness is 30 meters. Folding layers with high viscosity are separated by layers of low viscosity. Models are deformed in plane strain at a constant rate of 10^{-12} s^{-1}. Thus, the geologic time can be obtained by the strain rate and the natural strain which is referred to as shortening in the following parts.

The horizontal compression is achieved by uniform displacement boundary conditions applied over a time period of 15855 years resulting in a strain rate of 10^{-12} s^{-1}.

3.5. MODEL SETUP AND SENSITIVITY

3.5.1. Effect of Perturbation Geometry on Final Fold Shapes. The effect of the perturbation geometry (i.e. whether a horizontal section is added to the folding layer) is investigated in order to find a suitable geometry.. Four different perturbation geometries (on the left and right sides) are designed: (1) no horizontal layer, (2) short horizontal layer (500 m), (3) medium horizontal layer (1000 m), and (4) long horizontal layer (1500 m). The layer thickness is constant at 30 meters.

The geometry has both effects on the final fold shape and the amount of total strain (Figure.3.2 and Table 3.2.). With the horizontal layer existing on the right and left sides of the folding layer, stress concentrations develop during shortening, which reduces the deformation of the folding layer. These stress concentrations have significant influence on the stress distribution in the symmetric part of folding layer which is not the scope of this research (see Figure 3.3). Additionally, determining the length of the horizontal layer next to a fold structure in the field can be difficult. Therefore, for the following parametric studies, no horizontal layer is added to the folding layer.

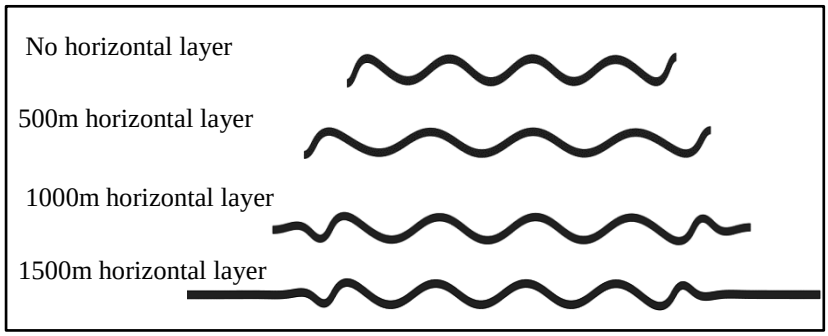

Figure 3.2 Final geometry of the numerical model with

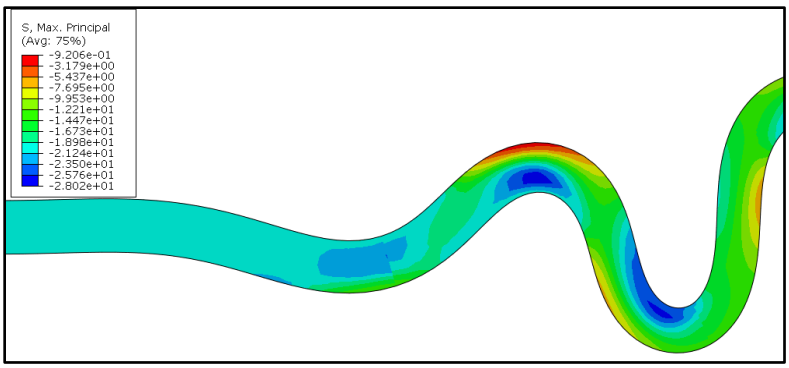

Figure 3.3 Stress concentration (effective minimum principle stress concentration) in the numerical model with 500 meters horizontal layer along the folding layer under 30% shortening.

Table 3.2 Final strain of folding layer under 30% shortening.

Horizontal layer length (m)	Maximum ε_x (%)	Maximum ε_y(%)
0	598.9	392.4
500	617.2	447.4
1000	670.4	502.4
1500	898.4	706.4

3.5.2. Initial Perturbation Geometry. Under horizontal compression a straight layer with no perturbation is shortened, and buckling is not initiated. Therefore, a perturbation is required as an initial condition (Biot, 1961). The initial amplitude in the FE model is 2.5 m, and five different wavelengths are investigated as initial conditions: 1000 m, 1500 m, 2000 m, 2500 m, and 5000 m. The same amount of horizontal compression is applied to all model geometries (40% shortening). The influence can be viewed on both the final deformation and the strain on the crest of the first "perfect" fold shape (see Figure.3.4 and Table 3.3). The initial perturbation wavelength significantly influences both the final deformation and the resulting strain. Rock compression in the middle of the model was offset by the large wavelength. Hence, the initial wavelength of the perturbation was set up as 1000 meters to ensure the shortening effect was maintained throughout the entire folding layer. Such geometric irregularities result in an initial dips

around 2.8° and approximate natural perturbations at a wavelength near the theoretically dominate one (see equation 55).

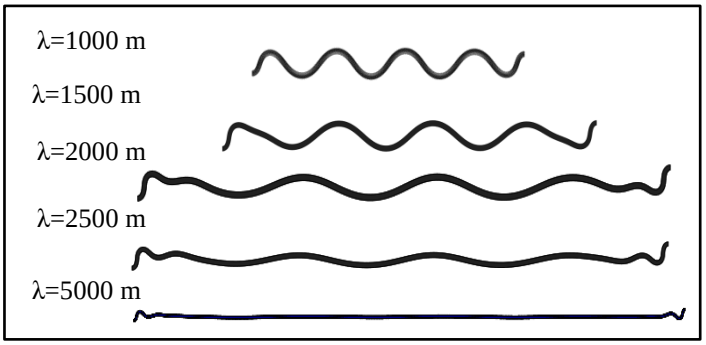

Figure 3.4 Final geometry of the numerical model with different initial wavelength perturbations subjected to 40% shortening.

Table 3.3 Final vertical strain of fold crest under 40% shortening.

Perturbation Wavelength (m)	Crest ε_y (%)
1000	681.3
1500	624.5
2000	341.7
2500	312.9
5000	280.2

3.6. MODEL VERIFICATION

3.6.1. Verification Based on Biot's Folding Theory. In order to validate the modeling approach of single layer buckling a simple model was setup and the results are compared to Biot's single layer folding theory (equation 56).

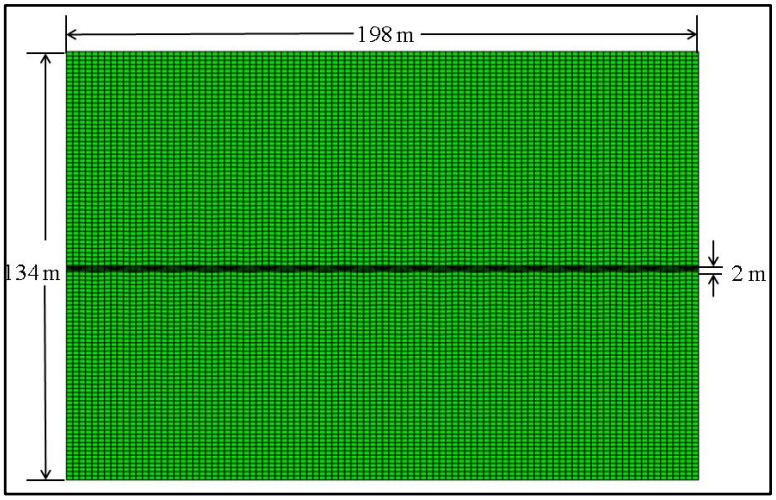

Figure 3.5 Geometry of the verification numerical model

The models' geometry is identical to those adopted by both Zhang et al (1996, 2000) and Mancktelow (1999). The length and width of the model were 198 m and 134 m, respectively. The bedding layer thickness is 2 m and the initial wavelength is 12 m (Figure 3.4). Without either pore pressure or gravity considered, this group of models features the same boundary condition (layer parallel shortening with 20% shortening). The final wavelengths for different competence contrast R tested are listed in Table 3.4.

Table 3.4 Comparison between the wavelength achieved and the dominant wavelength from the Biot-Ramberg equation (Equation 42)

R	Biot dominant wavelength (m)	Average wavelength (m)	Difference
20	18.8	19.8	1.0
42	24.0	22.62	1.38
100	32.1	31.68	0.42
200	40.4	39.6	0.8

The geometry in Biot's theory is a layer with a series of small initial perturbations of various wavelengths. However, the initial condition used here is different because the

perturbation only has one wavelength. This may be the reason for the slight difference between the simulation results and the theory.

3.6.2. Validation Based on Strain. The strain distribution can also be examined to check the simulation results. As mentioned in chapter 2, parallel folds are developed when buckling of a competent layer, embedded in an incompetent matrix. Parallel folds are characterized by a constant orthogonal thickness from crest to limb and an increase in its axial trace thickness (measured parallel to the axial trace) from crest to limb. To describe this phenomenon, Ramsay defines tangential longitudinal strain (Turcotte and Schubert, 2002). Based on this theory, the principal strain is parallel to the folding layering. As described in chapter 2.3.4, the tangential longitudinal strain are found to be close to folds in laboratory simulations (Laubsher, 1975) and match the strain patterns found in field (Prisco and Imposimato, 1996). In this research, tangential longitudinal strain is observed throughout the folding layer in the final deformation of the numerical model. The orthogonal thickness distribution in the folding layer is close to 30 meters which is the initial thickness (see Figure 3.6). And the principal strain distributing in the folding layer are parallel to the folding deformation (see Figure 3.7). Hence, the folding layer in the numerical model is classified as a parallel fold and the simulation results are validated by the observation of tangential longitudinal strain.

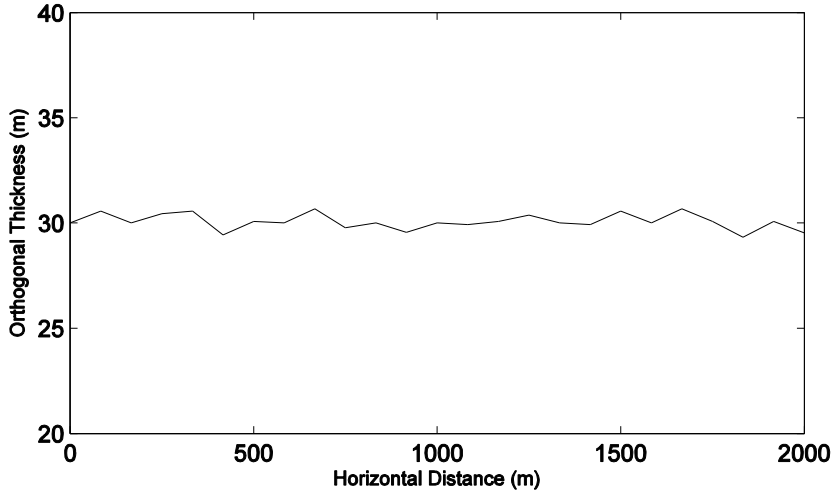

Figure 3.6 Orthogonal thickness distribution in the folding layer.

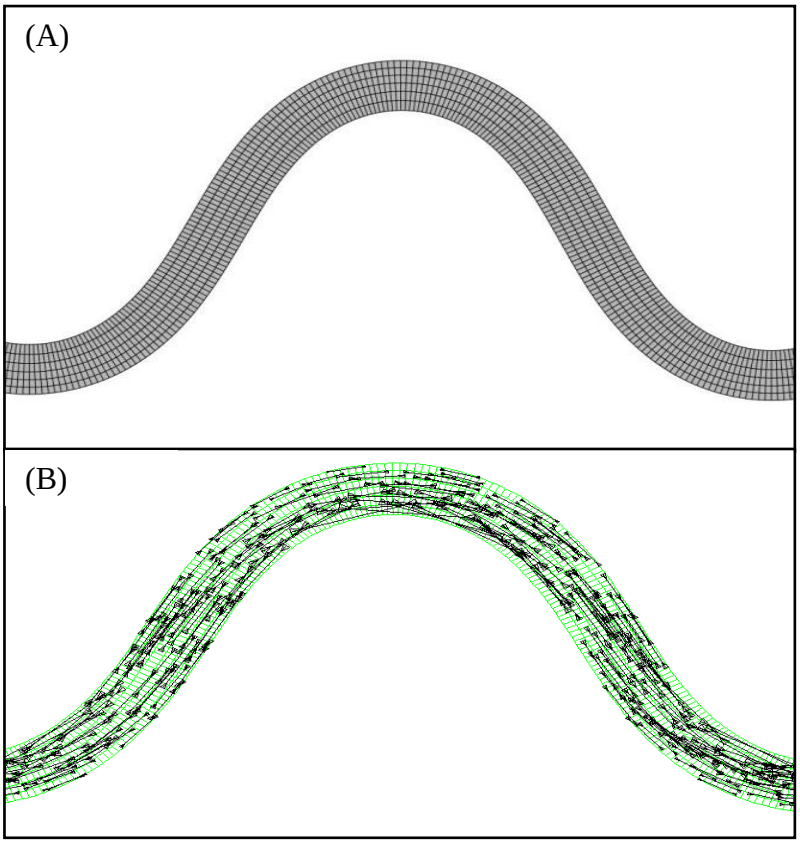

Figure 3.7 Deformation and strain of the numerical model after folding simulation.(A).Final geometry of the numerical model. (B). Distribution of logarithmic strain orientation in the folding layer.

4. RESULTS

In this group of simulations, a series of numerical models are established to investigate the influence of different material properties and boundary conditions on the fold's stress history. In the result analysis, the spatial and temporal evolution of the effective minimum principal stress (σ'_3) is studied in detail, as tensile failure occurs when σ'_3 reaches the tensile strength (T_o). Therefore, the timing of σ'_3 becoming negative is crucial.

For the following results analyses Figure 4.1 shows the numbering of the relevant elements to distinguish the results on the crest and limb of the folding layer. Since the stress distribution is symmetric along the fold structure, for the following results analyses, the stress history of the developing fold fractures at the crest of the fold and along a layer perpendicular cross-section in the limb (see Figure 4.2) is investigated. Based on the stress distribution, these locations are possible to generate tensile fracture.

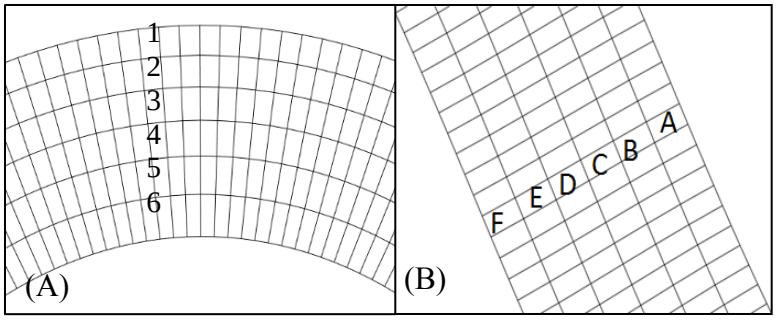

Figure 4.1 Elements numbering and locations. (A). Elements 1 to 6 are placed on the hinge zone of fold from the top to the bottom. . (B). Elements A to F are placed on the crest from the right to the left.

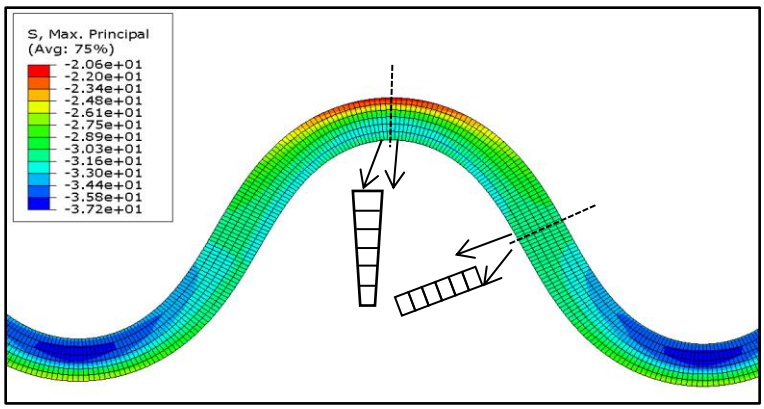

Figure 4.2 Effective minimum principal stress distribution over folding layer and the elements located on both the crest and the limb.

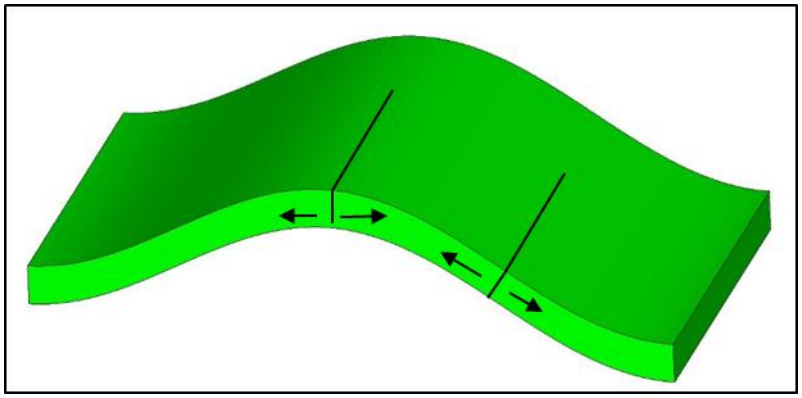

Figure 4.3 Possible tensile fractures at the crest and limb of a major fold based on the stress distributions in figure 4.2.

4.1. BASIC MODEL STRESS HISTORY

A basic model is developed to explore the stress history through the folding layer. The material properties in the folding layer and matrix are listed in Table 3.1. The fold structure has been successfully developed during the simulation progress. Figure 4.4 shows the effective minimum principal stress distribution history with fold development during 15.855 thousand years (i.e. $\dot{\varepsilon}=10^{-12}$ s^{-1}). Because of the symmetry of the model geometry, the stress distribution along the fold structure is symmetric.

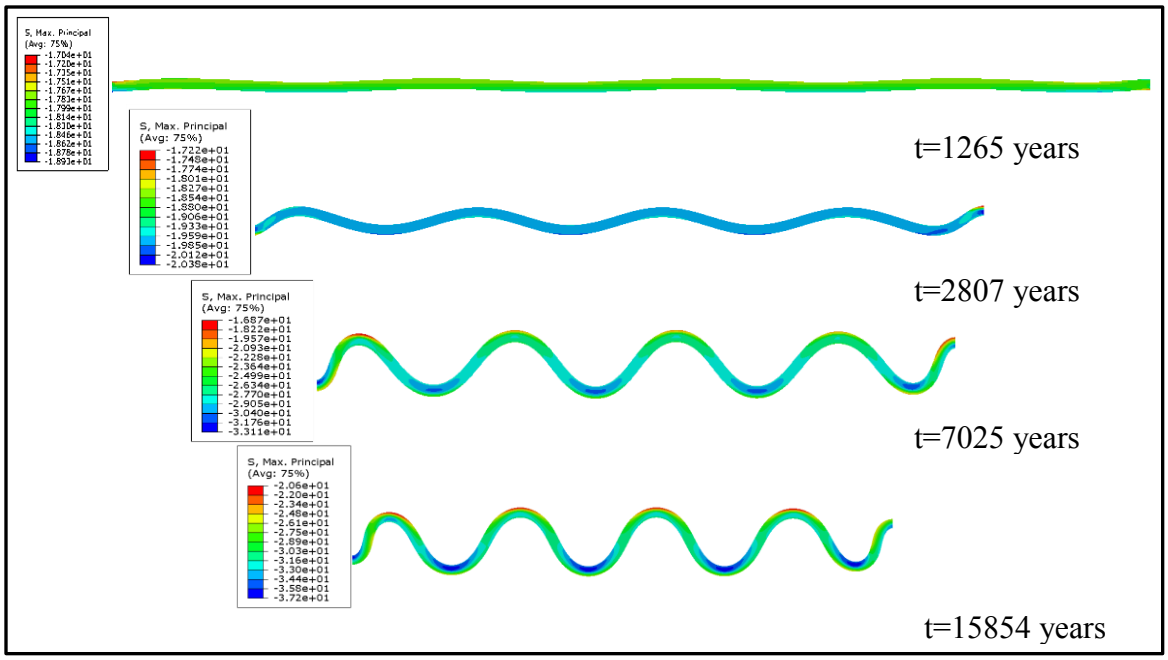

Figure 4.4 Fold/fold development in the numerical model in ~15000 years after 50% shortening is applied as a natural strain.

Figure 4.5 shows how the orientations of the maximum effective principal stress (σ'_1) changes along the folding structure and over time. In the hinge zone of the fold, σ'_1 is parallel to the layer up to 27% overall shortening. At this time, the folding layer undergoes layer-parallel shortening throughout. After that, the orientations of σ'_1 begin to rotate to the direction perpendicular to the layer on the convex side of the fold crest where layer-parallel lengthening occurs, and it remains to be parallel to the layer on the concave side where layer-parallel shortening occurs. In the limbs, σ'_1 rotates with model shortening as the folding angle increase. The orientations of σ'_1 tend to be parallel to shortening direction before the dipping angle of the limb increases to a high value (e.g. 50˚).

The σ'_1 orientation evolution of the crest elements are plotted in Figure 4.6. The effective principal stress magnitudes also vary throughout the folding layer (see Figure 4.2).

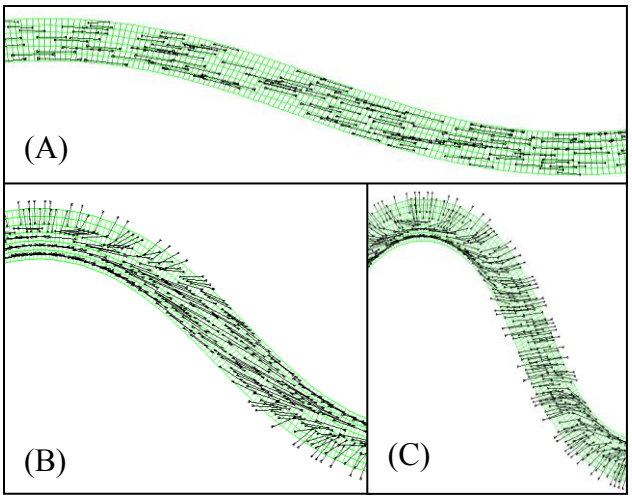

Figure 4.5 Orientations of σ_1´in numerical modeling of single layer folding. (A) 27% overall shortening. (B) 37% overall shortening.(C) 50% overall shortening

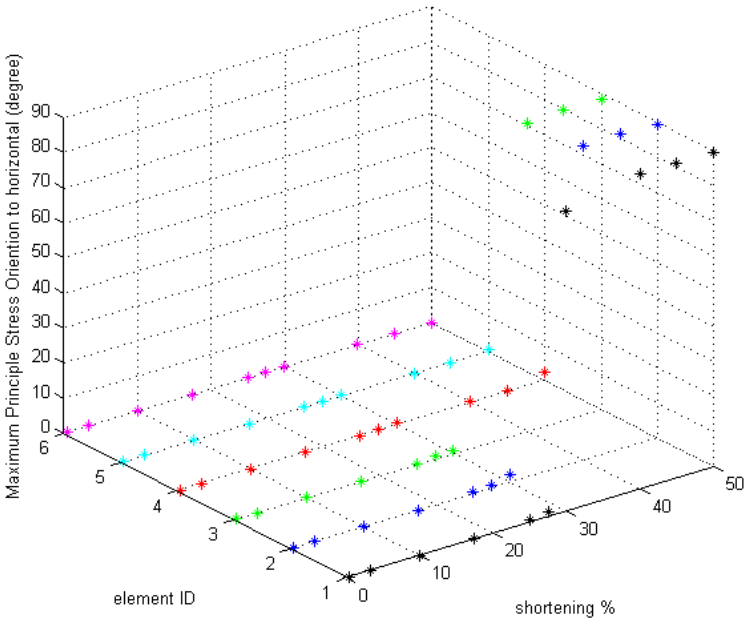

Figure 4.6 Orientations of effective maximum principle stress in crest elements (to horizontal).

The temporal development of the effective principal stresses at the fold's crest and limb are plotted in Figure 4.7 and 4.8. Throughout the limb of the fold, the effective principal stresses are roughly uniform and the minimum effective principal stress (σ'_3) increases at an approximate constant rate (Figure 4.8b). The most interesting result of the stress history is at the top of the fold. Along the hinge zone of the fold, σ'_1 begins to decrease after 17% shortening and increase again after 31% shortening (Figure 4.7c). The lowest value (23.2 MPa) is reached around 31% shortening on the convex side of the hinge zone. σ'_3 along the hinge zone of fold (Figure 4.7b) are initially approximately equal (i.e. before ~27% shortening) and increase constantly. After 27% shortening, σ'_3 decreases (for element 1 at 27%, element 2 at 35%, element 3 at 40 %) and drops to a minimum of 18.7 MPa at 40% shortening for element 1. Figure 4.9 shows the differential stresses history of the fold/fold crest over time. These changes reflect that the top of the crest is characterized by the lowest magnitudes of σ'_3 and σ_d and thus represents the location where tensile stresses are most likely. The bottom element of the crest is characterized by the highest differential stress and thus represents the region of the highest likelihood of shear failure. Thus, the "tensile stress" analysis in the following sections is based on the temporal development of the principal stresses of the element on the top of the crest of the folding layer (Element 1 in figure 4.7A). For comparison, the stress history of the element at the external limb is also investigated (Element *C* in figure 4.8B).

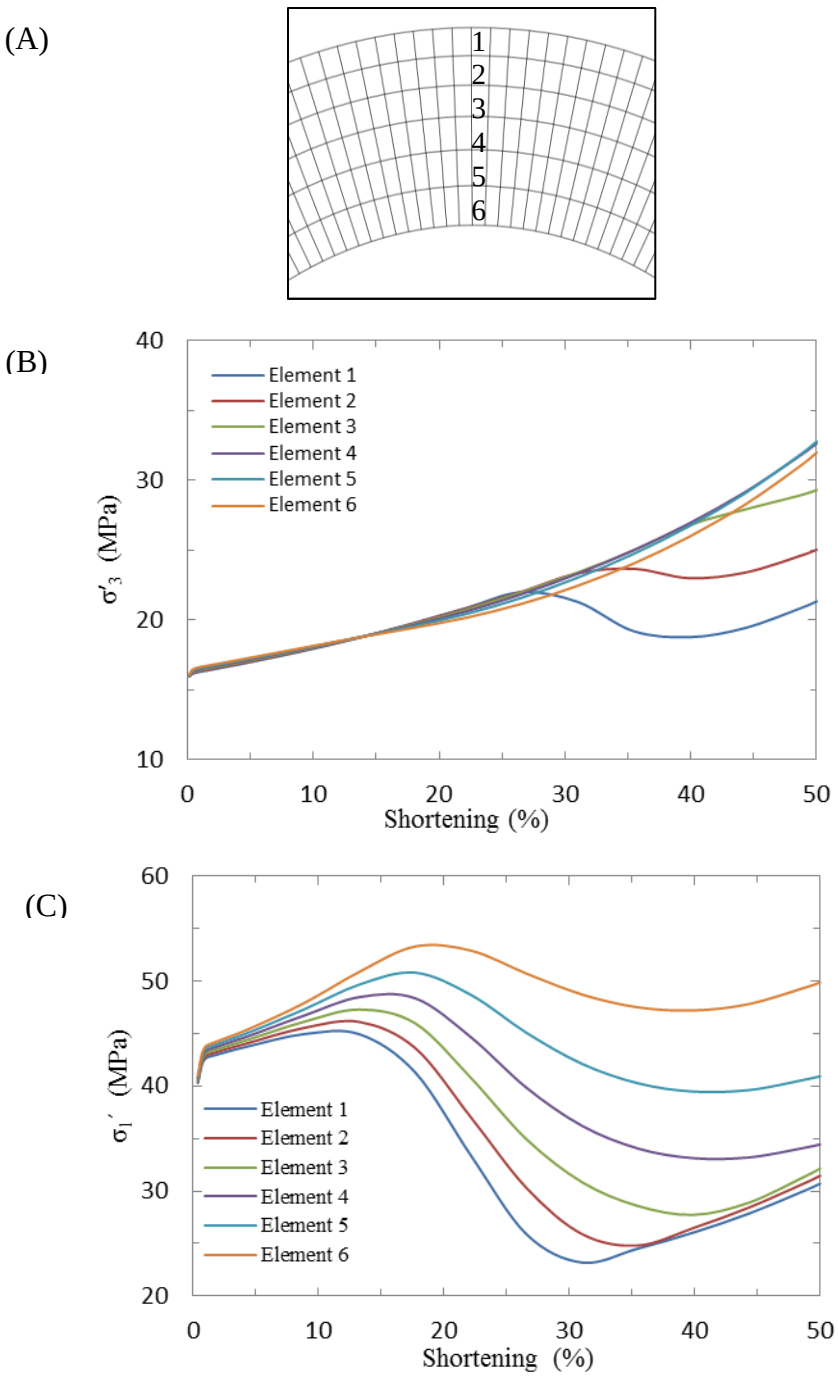

Figure 4.7 Element locations and stress history. (A). Elements 1 to 6 are placed on the hinge zone of fold/fold from the top to the bottom. (B). A plot of the effective minimum principal stress magnitude development for all elements over the period of shortening. (C). A plot of the effective maximum principal stress magnitude development for all elements over the period of shortening.

(A)

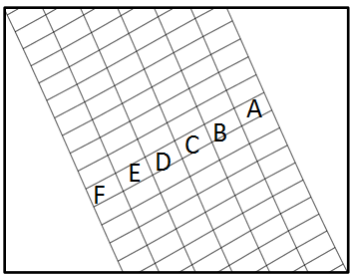

(B)

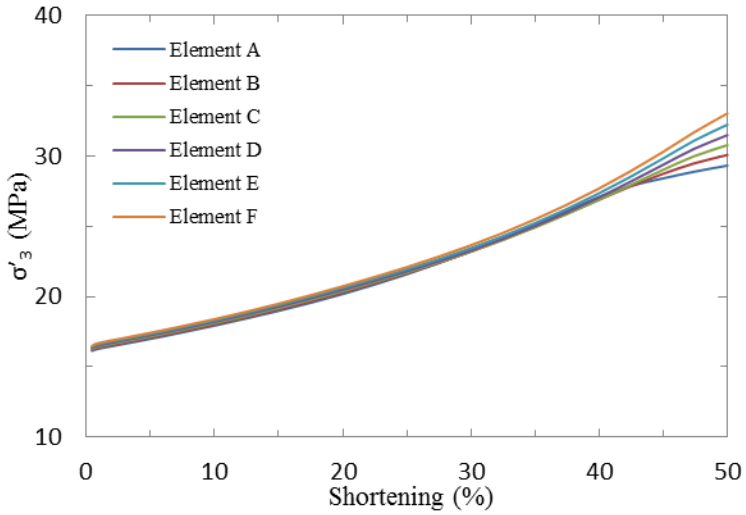

(C)

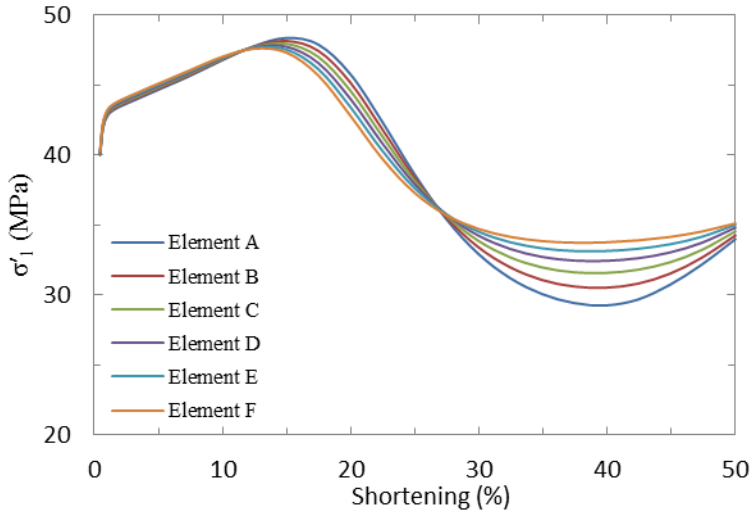

Figure 4.8 Limb elements locations and stress history. (A). Elements A to F are placed on the crest from the right to the left. (B). A plot of the effective minimum principal stress magnitude development for all limb elements over the period of shortening. (C). A plot of the effective maximum principal stress magnitude development for all limb elements over the period of shortening.

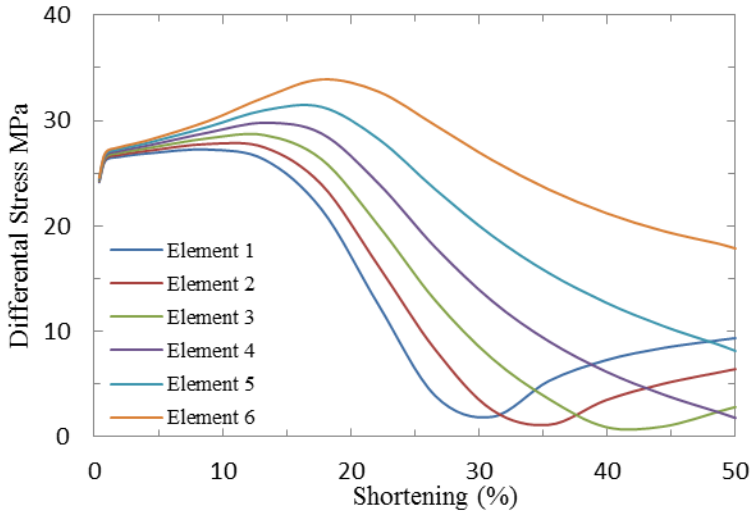

Figure 4.9 Differential stresses history of crest elements over shortening.

4.2. INFLUENCE OF COMPETENCE CONTRAST

Models with different competence contrasts are established to investigate their influence on the stress history of the folding layer. The matrix material properties, as shown in Table 3.1, remain constant and the folding layer material properties (e.g. E and μ) vary as the competence contrast (R) changes. R is assumed to have the same value for the ratios of Young's modulus (E) and viscosity (μ). Figure 4.10A illustrates how fold shape (including amplitude and thickness) changes with R when the matrix contains the same material. The effect performed by R on the fold geometry is consistent with the research of Johnson and Fletcher (1994). Because this group of single layer folds is assigned with the same initial geometry and boundary condition, folds with the same wavelengths are generated. The lowest competence contrast (R=5) shows a low amplification rate of folding and layer thickness increment. The highest competence contrast (R=168) shows a high amplification rate of folding. The amplitude of the fold increases significantly at an inconstant rate as the competence contrast increases (see figure 4.10B). High growth rate is observed before R reaches 40.

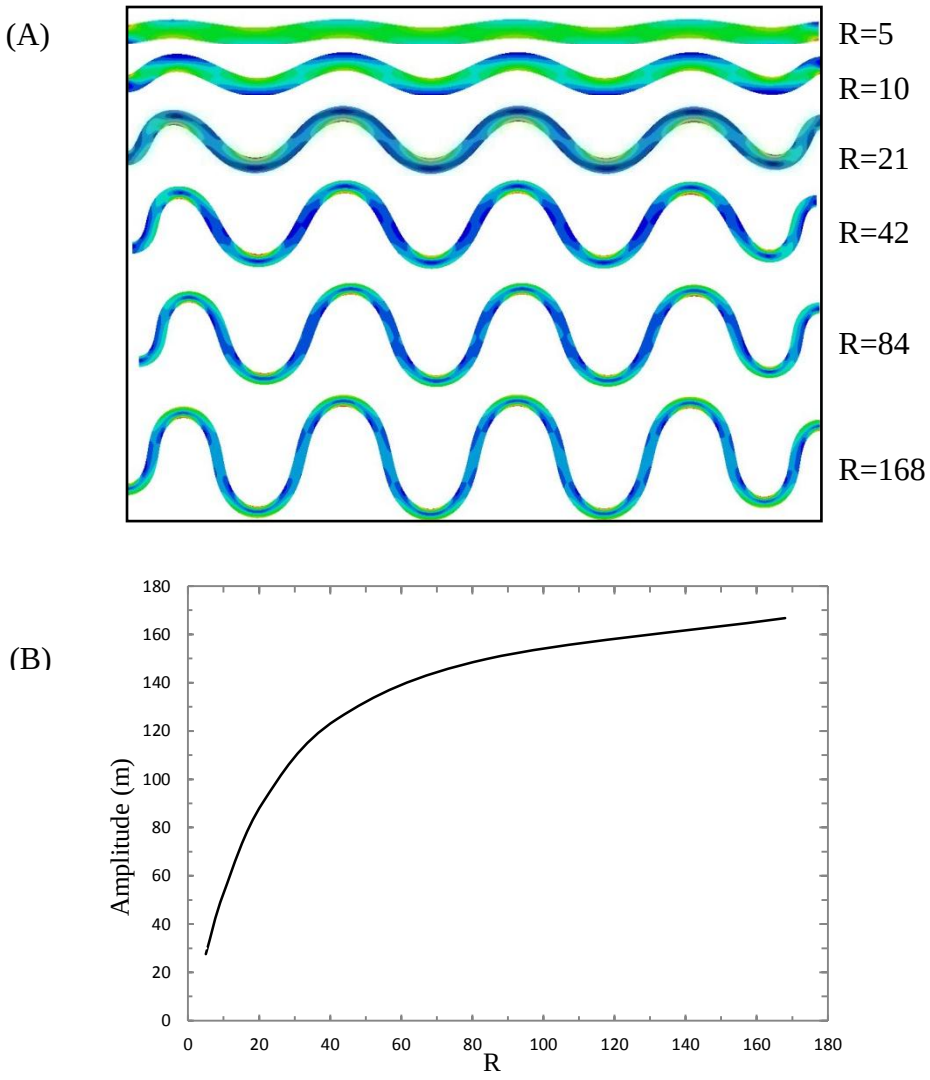

Figure 4.5 Numerical models of folding of a single layer embedded in a matrix with various properties. (A) Final fold forms for a single layer with different competence contrasts. The same initial perturbation is used to initiate all the folds. (B) Relationship between final amplitude and competence contrasts R.

The minimum effective principal stress (σ'_3) histories of the folding layer at the crest and limb for a series of models with different competence contrast are included in the following plots (Figure 4.11 to Figure 4.15). The observations are summarized as follows:

⑴ The stress histories at different locations in both crest and limb are close to each other when the contrast is as low as 5 and 10 (see Figure 4.11 and 4.12). σ'_3 increases with shortening both at the folding layer crest and limb.

⑵ The stress histories at different locations in both crest and limb are close to each other before 40% shortening when the contrast equals to 21 (see Figure 4.13) . After that, σ'_3 decreases with shortening at the top of crest. For the limb, σ_3' increases with time throughout the entire shortening.

⑶ The stress development at the crest and limb are highly dependent on the location at high competence contrast models (e.g. R=84 and R=168). A decrease of σ'_3 is first observed both at the top crest and limb when the contrast is as high as 168. Tensile stress is generated at the top of the crest in the folding layer with the same high contrast (see Figure 4.14 and 4.15).

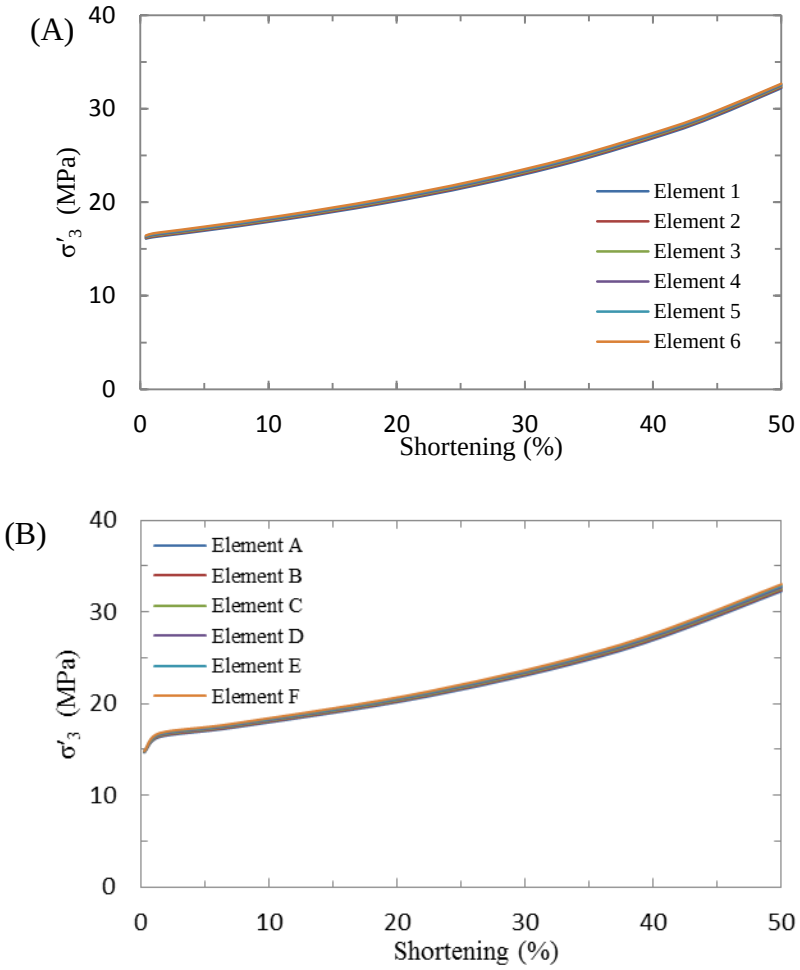

Figure 4.6 Stress history for numerical model with R=5. (A) Effective minimum principal stress development at the crest of the folding layer with R=5. Elements 1 to 6 are located as shown in Figure 4.1. (B) Effective minimum principal stress development at the limb of the folding layer with R=5. Elements A to E are located as shown in Figure 4.1.

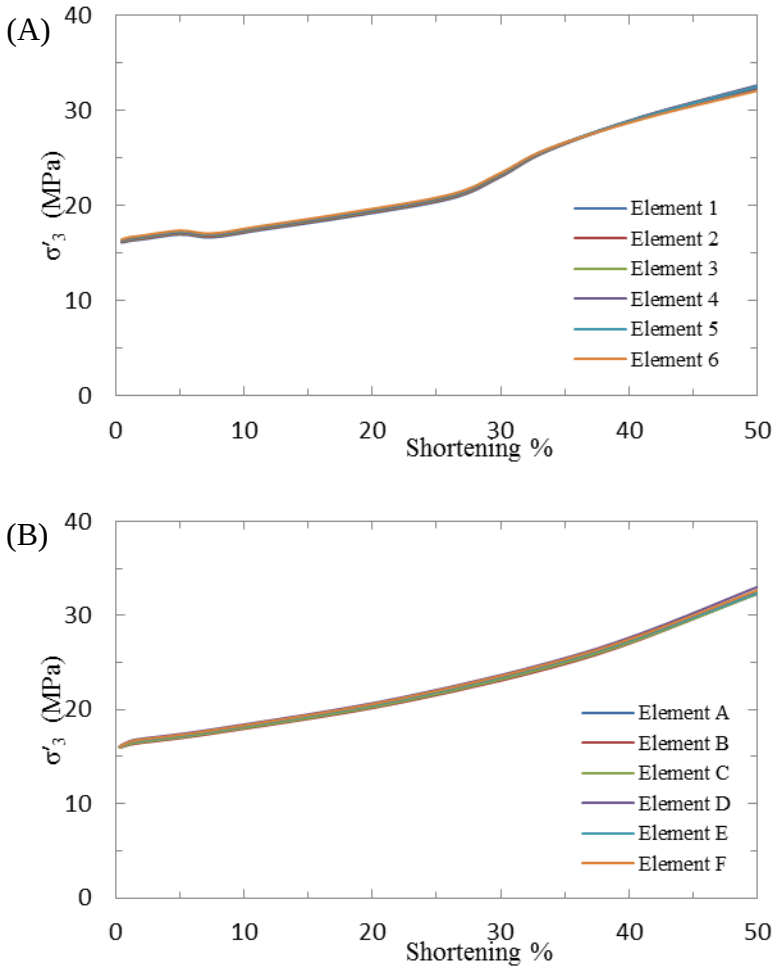

Figure 4.7 Stress history for numerical model with R=10. (A) Effective minimum principal stress development at the crest of the folding layer with R=10. Elements 1 to 6 are located as shown in Figure 4.1. (B) Effective minimum principal stress development at the limb of the folding layer with R=10. Elements A to E are located as shown in Figure 4.1.

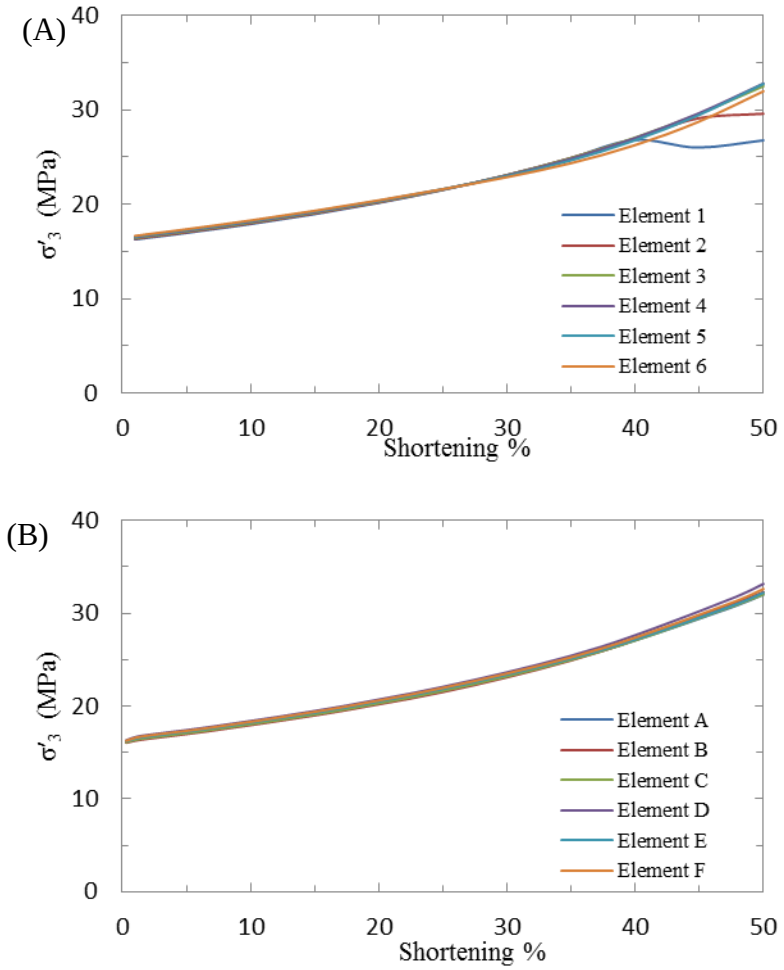

Figure 4.8 Stress history for numerical model with R=21. (A) Effective minimum principal stress development at the crest of the folding layer with R=21. Elements 1 to 6 are located as shown in Figure 4.1. (B) Effective minimum principal stress development at the limb of the folding layer with R=21. Elements A to E are located as shown in Figure 4.1.

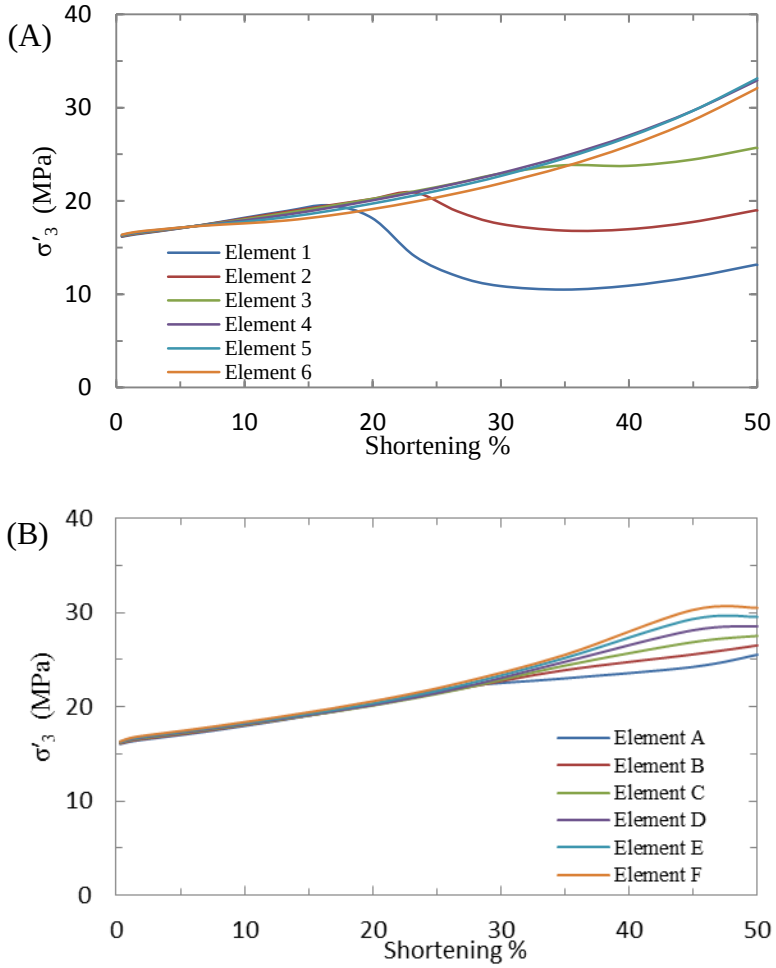

Figure 4.9 Stress history for numerical model with R=84. (A) Effective minimum principal stress development at the crest of the folding layer with R=84. Elements 1 to 6 are located as shown in Figure 4.1. (B) Effective minimum principal stress development at the limb of the folding layer with R=84. Elements A to E are located as shown in Figure 4.1.

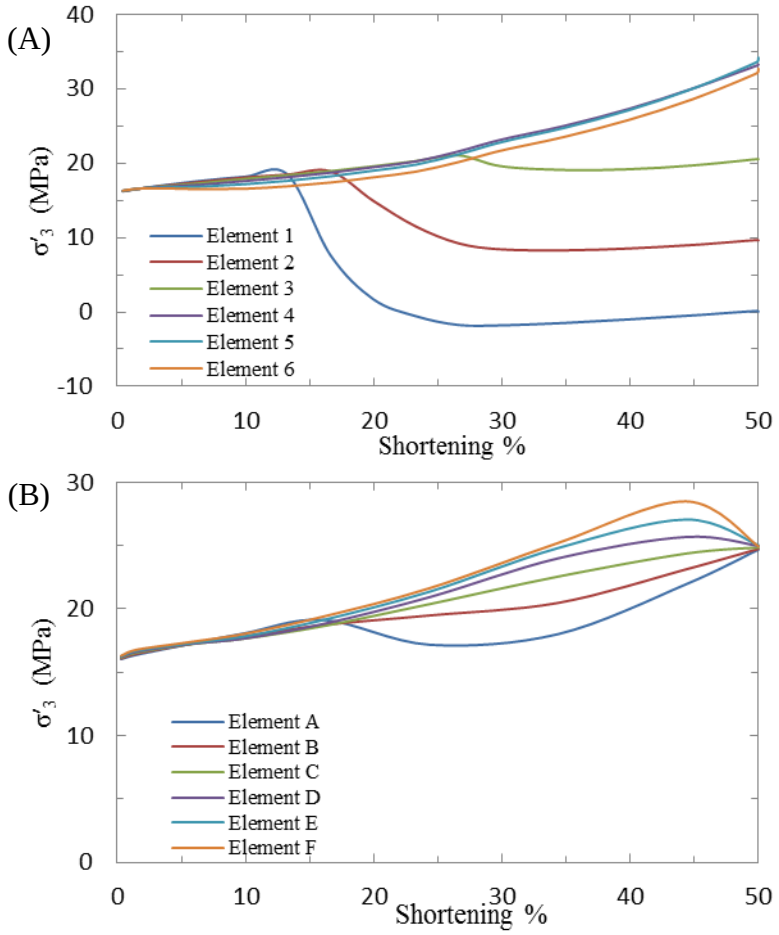

Figure 4.10 Stress history for numerical model with R=168. (A) Effective minimum principal stress development at the crest of the folding layer with shortening when R=168. Elements 1 to 6 are located as shown in Figure 4.1. (B) Effective minimum principal stress development at the limb of the folding layer with R=168. Elements A to E are located as shown in Figure 4.1.

The relationships between the effective minimum principal stress (σ'_3) at the fold crest and shortening are plotted in Figure 4.8 to investigate the influence of R on the stress history. An increase of R has a profound effect on both the time and the degree of the σ'_3 decline. The effect of increasing R resulting in a larger s'3 drop at a smaller shortening stage is illustrated in Figure 4.8. The most interesting result of the competence contrast analysis is the existence of tensional stress after a specific amount of shortening, exemplified by the model with the highest contrast (R=168). For a high contrast between folding layer and matrix material properties, tensile failure can be generated from the

pure tensional stress field on the crest. σ'_3 at the fold limb increases with shortening, and increasing R has only a minor effect on the stress magnitude increment after 40% shortening.

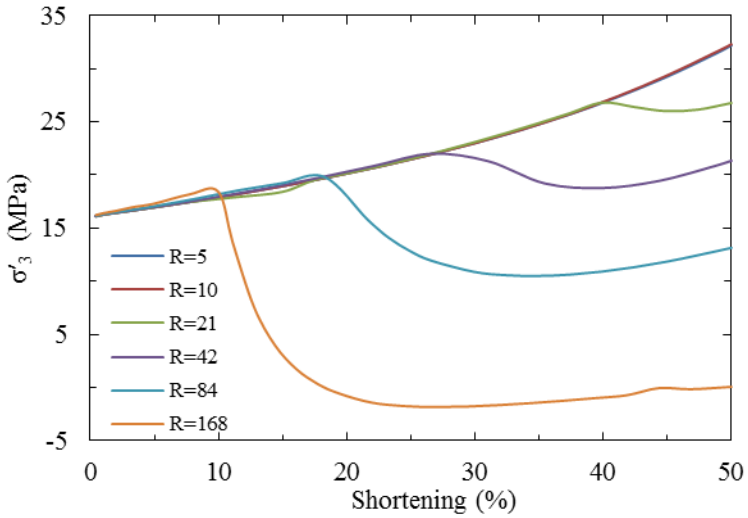

Figure 4.11 Effective minimum principal stress at the crest of fold development with shortening under different competence contrast.

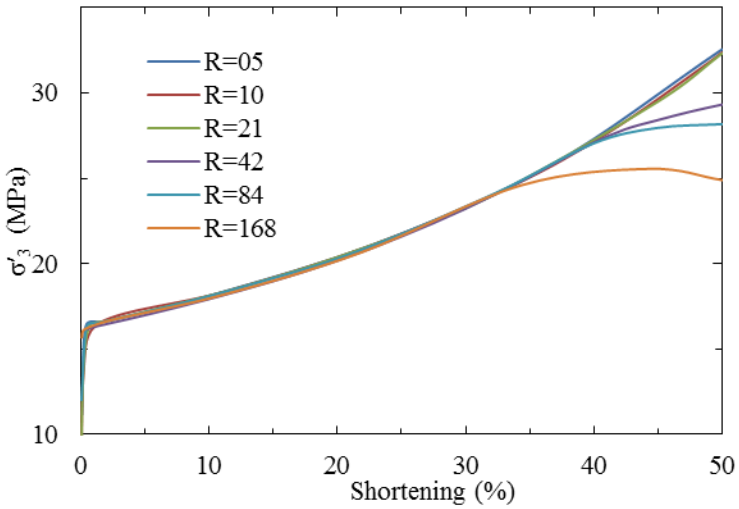

Figure 4.12 Effective minimum principal stress at the limb of the folding layer with shortening for different competence contrasts.

4.3. INFLUENCE OF VISCOSITY

The influence of viscosity on folding shapes is shown in Figure 4.18A. For a constant competence contrast (R=42), the viscosity of the folding layer (μ_f) varies from 5×10^{16} Pa s to 10^{21} Pa s which is a common range of crustal rocks viscosity (Twiss and Moores, 2007). The remaining material properties in these models are assigned as listed in Table 3.1. The inter-limb angle (the angle between the tangents to the folds at the inflection points, see Figure 4.18B) is used here to illustrate the viscosity impact on fold deformation tightness. The effect of increasing μ_f results in folds changing from tight to open (Figure 4.18). High viscosity (e.g. 10^{21} Pa s) has a profound effect on the geometry of folds and leads to asymmetrical deformation. Based on the fold classification, the folding layer geometry is close to a polyclinal fold and its investigation is beyond of the scope of this project. Thus, the single layer numerical model with a viscosity of 10^{21} Pa s is excluded in the following analysis.

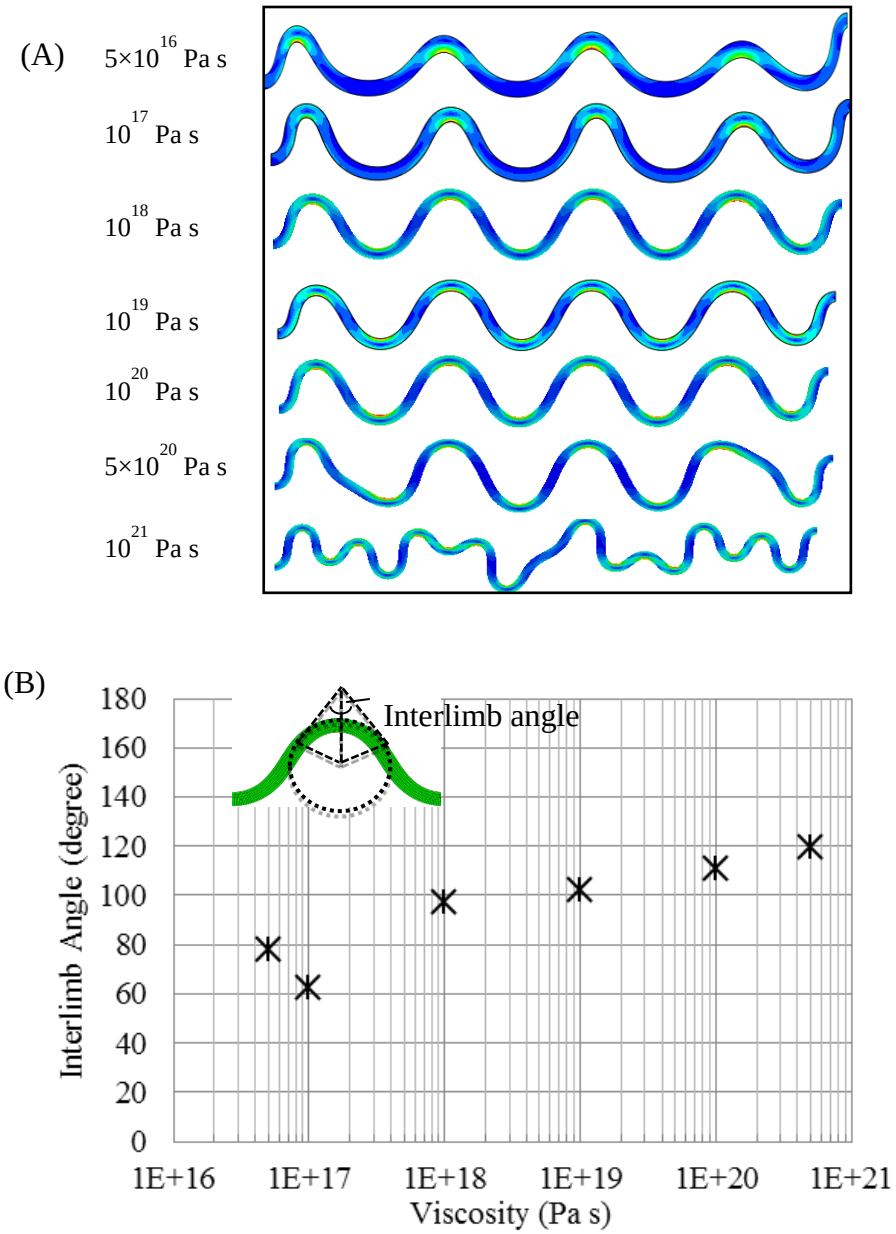

Figure 4.13 Numerical models of folding of a single layer embedded in a matrix with varying viscosity. (A) Final fold forms for a single layer with different viscosity. (B) Interlimb angle at different viscosities.

The history of the minimum effective principal stresses (σ'_3) of the folding layer at the crest and limb in a series of models with different viscosities (5×10^{16} Pa s , 10^{17} Pa s , 10^{18} Pa s, 5×10^{19} Pa s , and 10^{20} Pa s) are included in the following plots (Figure 4.19 to Figure 4.23). The stress development of the folding layer with a viscosity of 10^{19} Pa s

can be found in Section 4.1 (Figure 4.7 and 4.8). The observations are summarized as follows:

(1) The stress histories at different locations in both crest and limb are close to each other when the viscosity is low ($<10^{19}$ Pa s , see Figure 4.19 to Figure 4.21). σ'_3 increases with shortening both at the folding layer crest and limb.

(2) The stress histories at different locations in both crest and limb are close to each other before 15% shortening when the applied viscosity is high ($>10^{19}$ Pa s, see Figure 4.22 and 4.23). During the following buckling period (>15% shortening), the stress development is highly depend on the position. A decrease of σ'_3 can be observed at the top two to three elements of the crest and limb (Figures 4.21 to 4.23). While the decrease of σ'_3 at the crest elements occurs as early as 27 % of shortening, the decrease of $\sigma'3$ in the limb occurs after 40 % of shortening. . Considerable tensile stress (i.e. 55.4MPa) is generated at the top of the crest in the folding layer for high viscosities ($>10^{20}$ Pa s, see Figure 4.23) which is unrealistic and results from not including model plasticity.

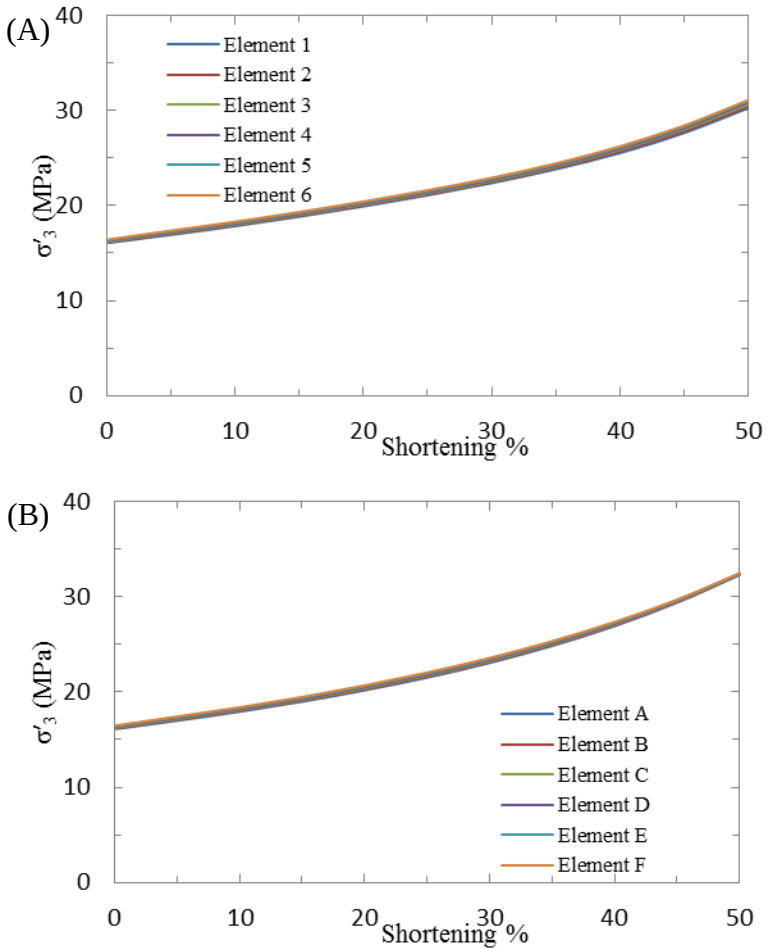

Figure 4.19 Stress history for numerical model with $\mu=5\times10^{16}$ Pa s. (A) Effective minimum principal stress development at the crest of the folding layer with $\mu=5\times10^{16}$ Pa s. Elements 1 to 6 are located as shown in Figure 4.1. (B) Effective minimum principal stress development at the limb of the folding layer with $\mu=10^{17}$ Pa s. Elements A to E are located as shown in Figure 4.1.

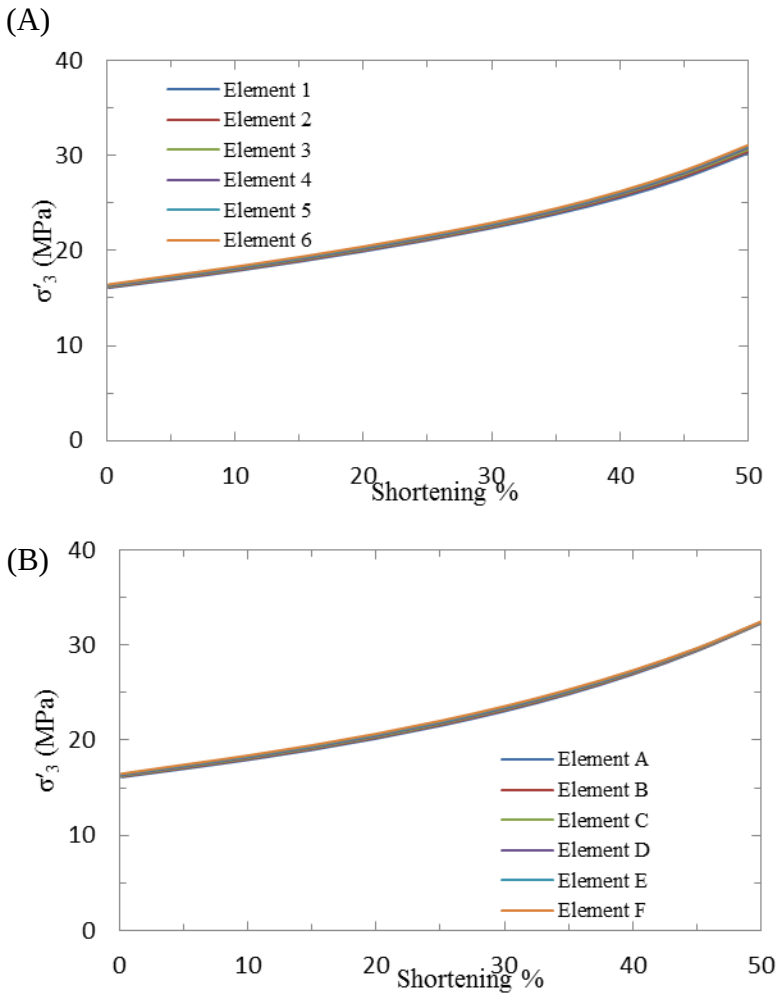

Figure 4.14 Stress history for numerical model with $\mu=10^{17}$ Pa s. (A) Effective minimum principal stress development at the crest of the folding layer with $\mu=10^{17}$ Pa s. Elements 1 to 6 are located as shown in Figure 4.1. (B) Effective minimum principal stress development at the limb of the folding layer with $\mu=10^{17}$ Pa s. Elements A to E are located as shown in Figure 4.1.

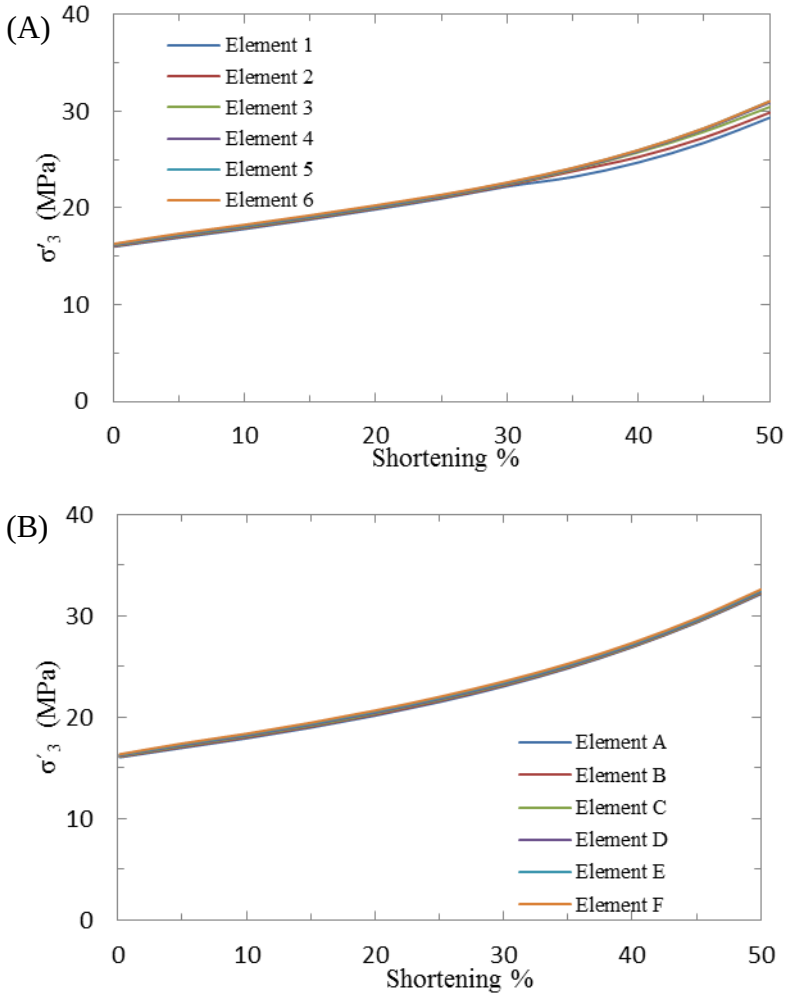

Figure 4.15 Stress history for numerical model with $\mu=10^{18}$ Pa s. (A) Effective minimum principal stress development at the crest of the folding layer with $\mu=10^{18}$ Pa s. Elements 1 to 6 are located as shown in Figure 4.1. (B) Effective minimum principal stress development at the limb of the folding layer with $\mu=10^{18}$ Pa s. Elements A to E are located as shown in Figure 4.1.

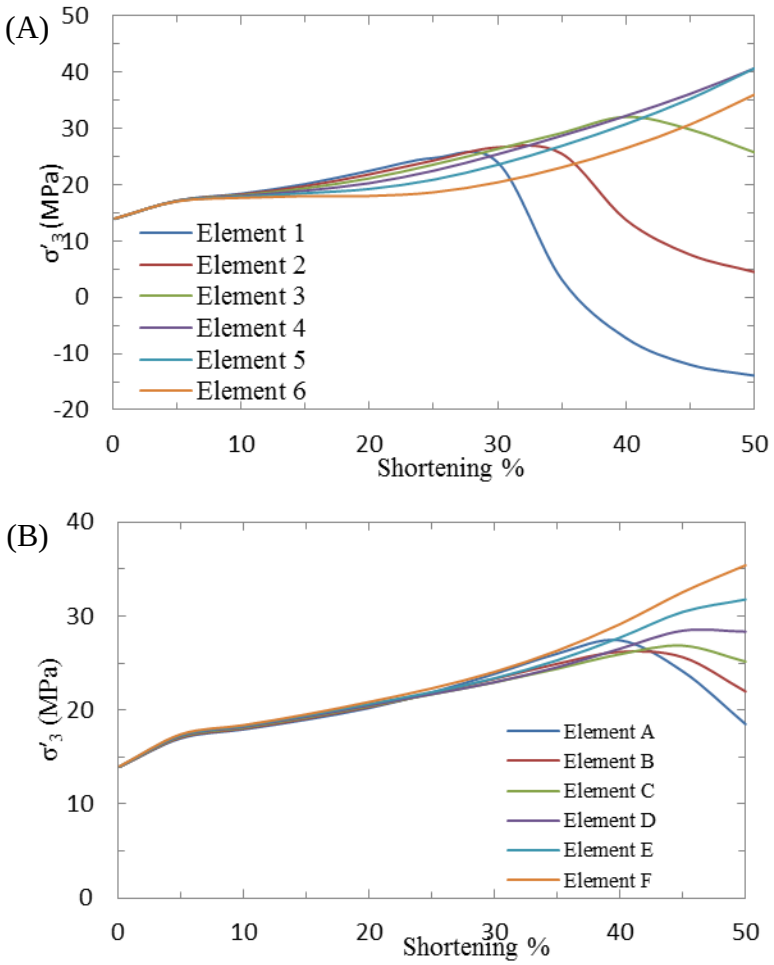

Figure 4.16 Stress history for numerical model with $\mu=5\times10^{19}$ Pa s. (A) Effective minimum principal stress development at the crest of the folding layer with $\mu=5\times10^{19}$ Pa s. Elements 1 to 6 are located as shown in Figure 4.1. (B) Effective minimum principal stress development at the limb of the folding layer with $\mu=5\times10^{19}$ Pa s. Elements A to E are located as shown in Figure 4.1.

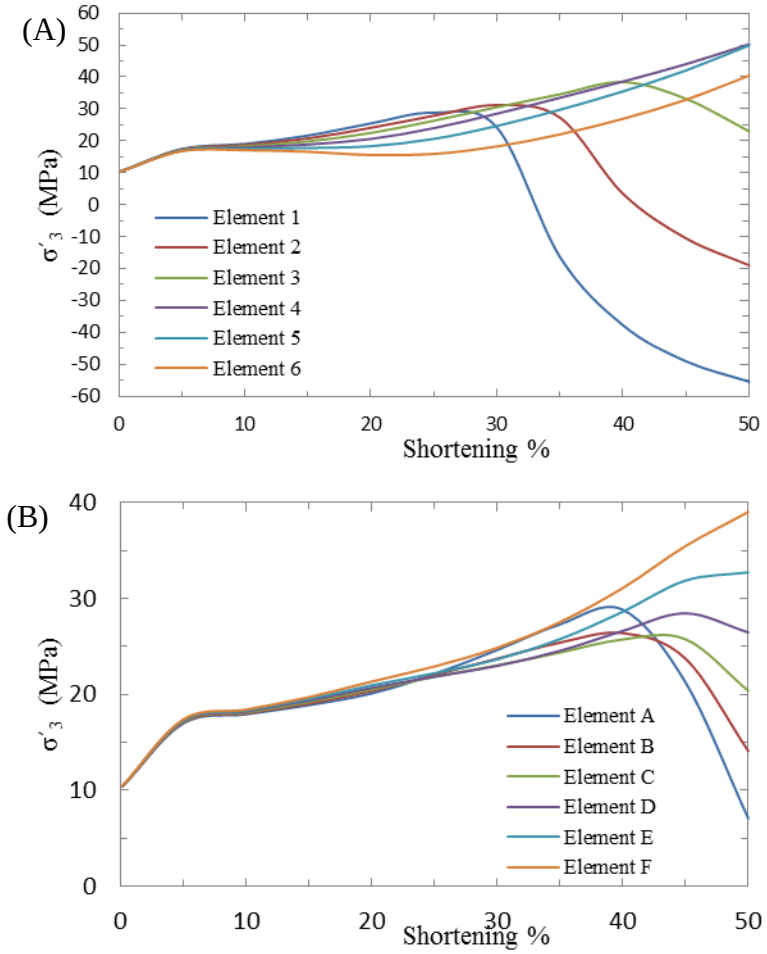

Figure 4.17 Stress history for numerical model with $\mu=10^{20}$ Pa s. (A) Effective minimum principal stress development at the crest of the folding layer with $\mu=10^{20}$ Pa s. Elements 1 to 6 are located as shown in Figure 4.1. (B) Effective minimum principal stress development at the limb of the folding layer with $\mu=10^{20}$ Pa s. Elements A to E are located as shown in Figure 4.1.

Figure 4.24 shows that there are slight difference in the stress evolutions on the crest of the folding layer when viscosity increases from 5×10^{16} Pa s to 10^{19} Pa s. For higher viscosity (>10^{19} Pa s), the effect of increasing μ_f results in significant differences in the stress evolution. It can be observed that the mechanical response to shortening depends on the layer viscosity. The model featuring the highest viscosity ($\mu_f=10^{21}$ Pa s) is removed from this analysis because of the asymmetrical deformation of the folding layer. Figure 4.25 shows that there are slight differences in the stress evolutions on the folding

layer limb between 7% and 32% shortening. For higher viscosities (>10^{19} Pa s), the effect of increasing μ_f causes a significant decrease of σ'_3 after 32% shortening.

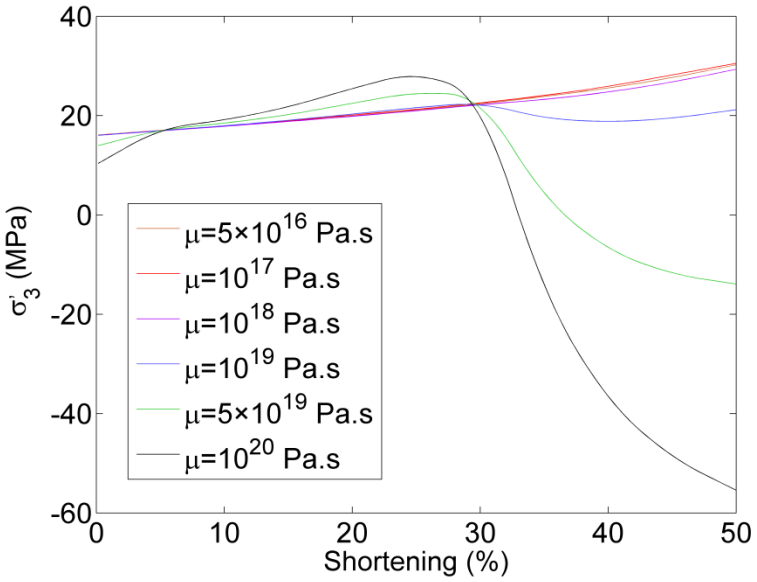

Figure 4.18 Effective minimum principal stress at the crest of the fold with different viscosities.

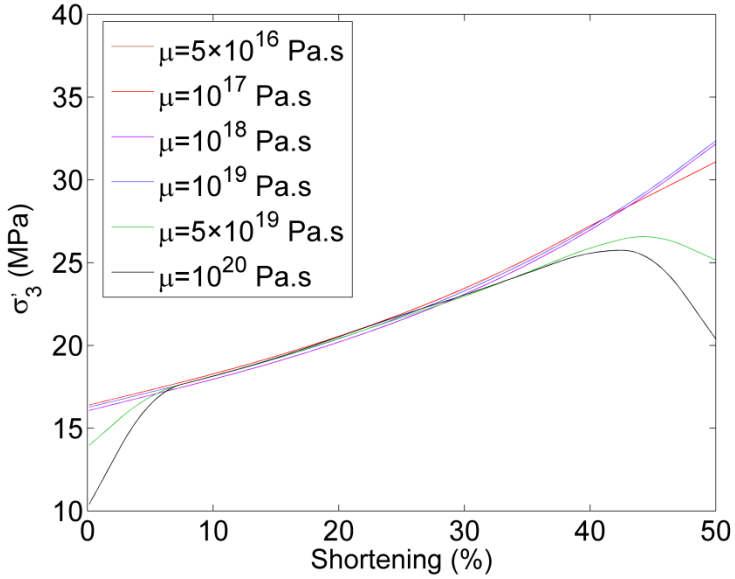

Figure 4.19 Effective minimum principal stress at the limb of the fold for different viscosities.

4.4. INFLUENCE OF STRAIN RATE

Numerical models loaded at various strain rates with the same initial perturbation and material properties are established to investigate the influence of strain rate. The material strain rate varies between 10^{-11} sec^{-1} and 10^{-14} sec^{-1}. The remaining material properties in these models are assigned as listed in table 3.1.

The temporal history of the minimum effective principal stress (σ'_3) at the crest and limb of the folding layer in a series of models with different strain rates (10^{-11} sec^{-1}, 5×10^{-12} sec^{-1}, 10^{-13} sec^{-1} and 10^{-14} sec^{-1}) are included in the following plots (Figure 4.26 to Figure 4.29). The stress development of the folding layer with strain rate as 10^{-12} sec^{-1} can be found in Section 4.1. The observations are summarized as:

(1) The stress histories at different locations in both crest and limb are close to each other before 15% shortening when the applied strain rate is high ($>10^{-12}$ sec^{-1}, see Figure 4.26 and Figure 4.27). During the following buckling period, the stress development at the crest and limb of the folding layer are highly depending on the location. A decrease of σ'_3 can be observed for the top elements (1&2) at the crest and considerable tensile stress is generated for high stain rates ($>10^{-12}$ sec^{-1}). For elements on the limb, a steep decrease of σ'_3 is observed after 40% shortening without reaching tensile magnitudes.

(2) The stresses histories at different locations in both crest and limb are close to each other when the viscosity is low ($<10^{-12}$ sec^{-1} , see Figure 4.28 and 4.29). σ'_3 increases with shortening both at the folding layer crest and limb.

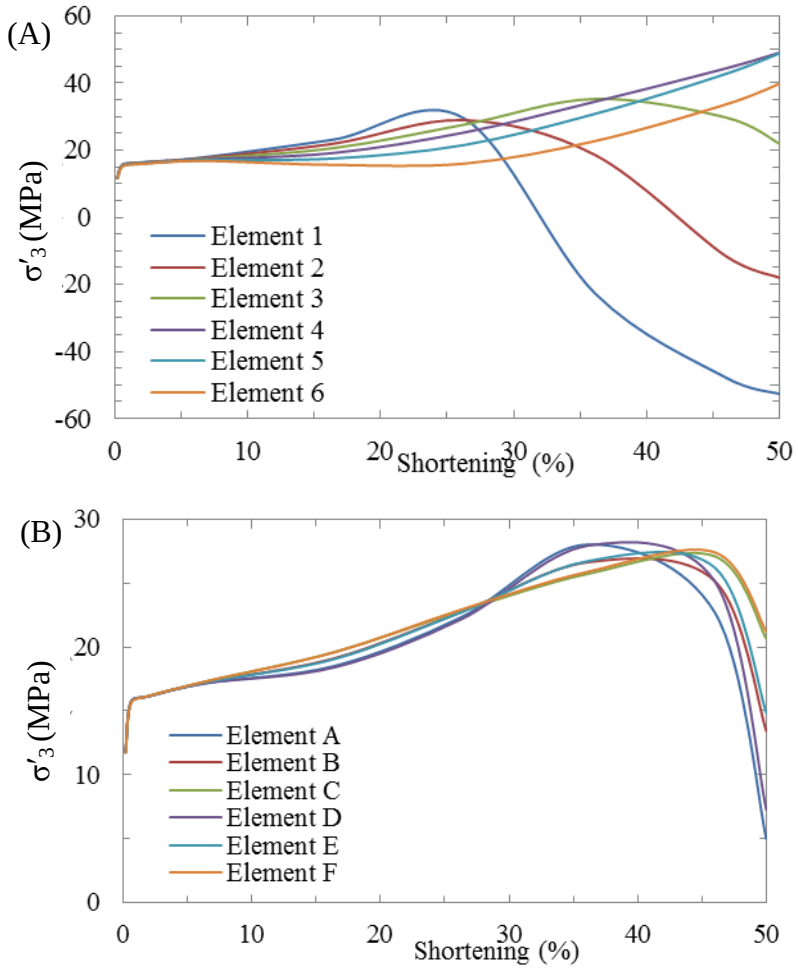

Figure 4.20 Stress history for numerical model with $\dot{\varepsilon}=10^{-11}s^{-1}$. (A) Effective minimum principal stress development at the crest of the folding layer with $\dot{\varepsilon}=10^{-11}s^{-1}$. Elements 1 to 6 are located as shown in Figure 4.1. (B) Effective minimum principal stress development at the limb of the folding layer with $\dot{\varepsilon}=10^{-11}s^{-1}$. Elements A to E are located as shown in Figure 4.1.

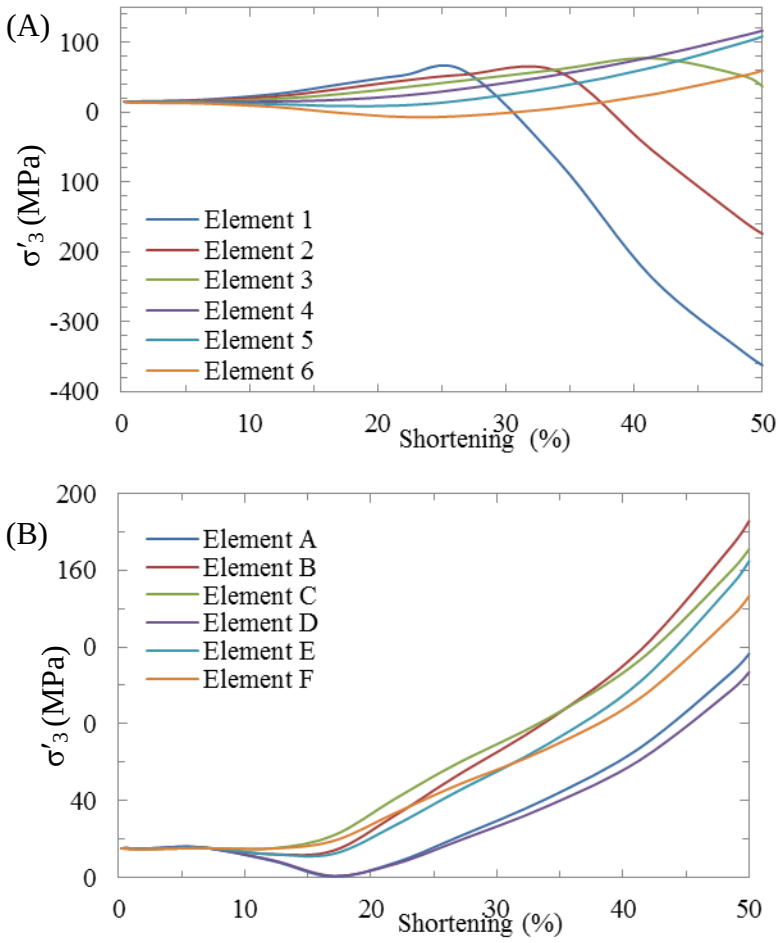

Figure 4.21 Stress history for numerical model with $\dot{\varepsilon}=5\times10^{-12}s^{-1}$. (A) Effective minimum principal stress development at the crest of the folding layer with $\dot{\varepsilon}=5\times10^{-12}s^{-1}$. Elements 1 to 6 are located as shown in Figure 4.1. (B) Effective minimum principal stress development at the limb of the folding layer with $\dot{\varepsilon}=5\times10^{-12}s^{-1}$ Elements A to E are located as shown in Figure 4.1.

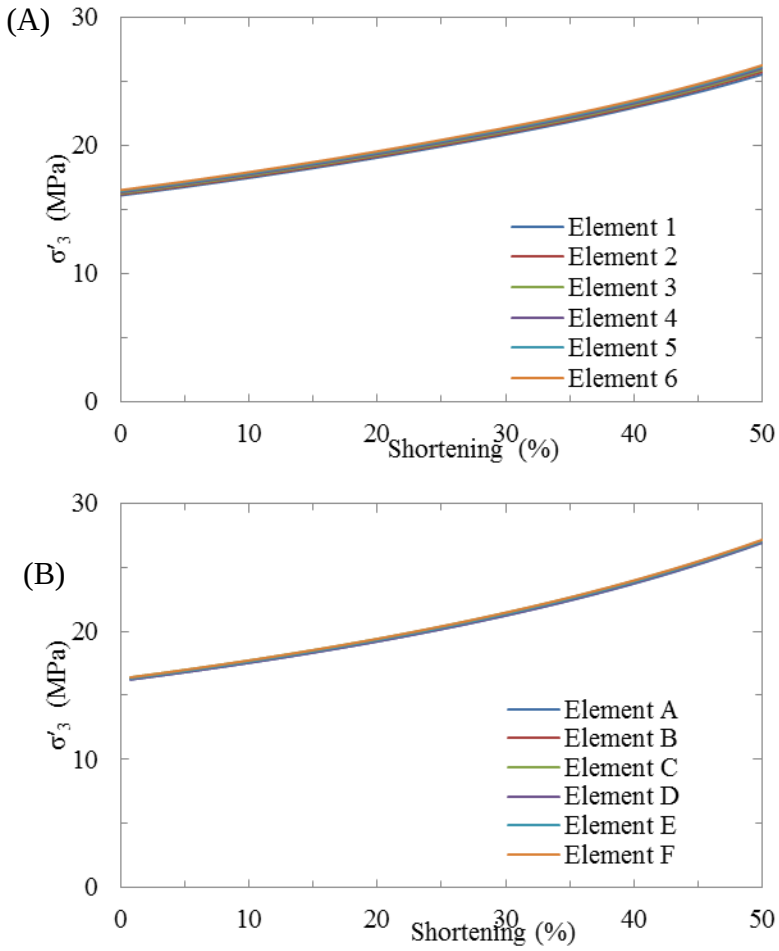

Figure 4.22 Stress history for numerical model with $\dot{\varepsilon}=10^{-13}s^{-1}$. (A) Effective minimum principal stress development at the crest of the folding layer with $\dot{\varepsilon}=10^{-13}s^{-1}$. Elements 1 to 6 are located as shown in Figure 4.1. (B) Effective minimum principal stress development at the limb of folding layer with $\dot{\varepsilon}=10^{-13}s^{-1}$. Elements A to E are located as shown in Figure 4.1.

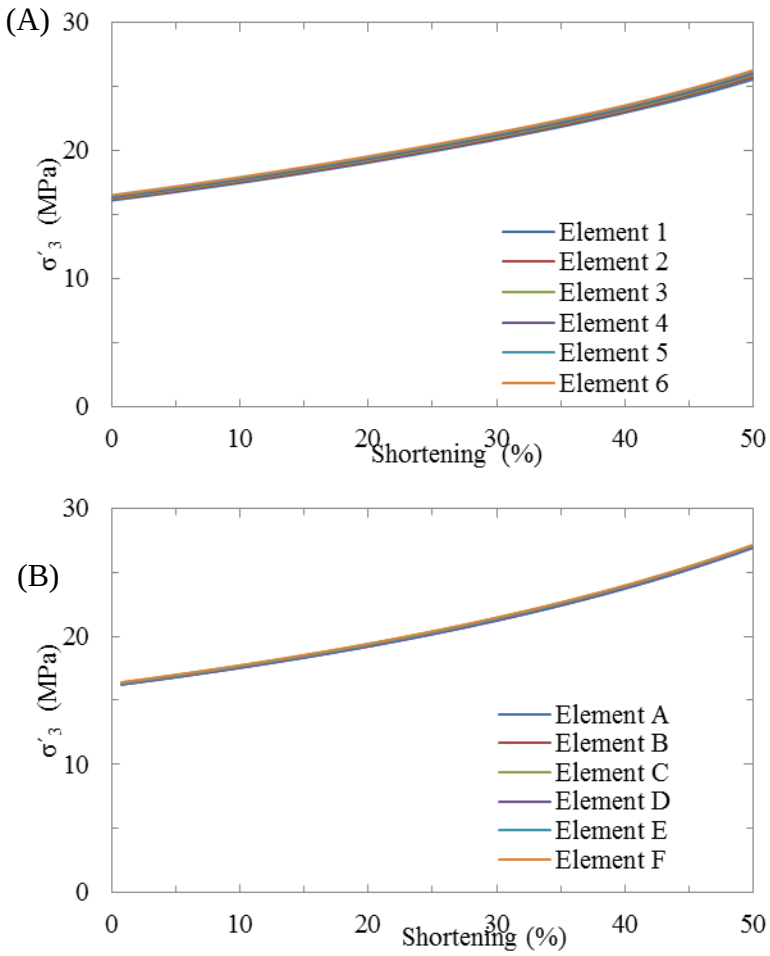

Figure 4.29 Stress history for numerical model with $\dot{\varepsilon}=10^{-14}s^{-1}$. (A) Effective minimum principal stress development at the crest of the folding layer with $\dot{\varepsilon}=10^{-14}s^{-1}$. Elements 1 to 6 are located as shown in Figure 4.1. (B) Effective minimum principal stress development at the limb of folding layer with $\dot{\varepsilon}=10^{-14}s^{-1}$. Elements A to E are located as shown in Figure 4.1.

Figure 4.30 shows the stress histories for different strain rates on the same model and suggests that the strain rate significantly impacts the material behavior. Higher strain rates tend to change the response of the bedding layer within the viscous material to behave elastically. Tensile stress and possible development of tensile failure are found before 32% shortening during the progress at a strain rate of 10^{-11} s^{-1}. After that the stress increases sharply due to the compaction. As an example, the effective minimum principal stress at the crest of the fold begins to drop rapidly after 27% shortening and tensile stress

is exhibited when the rate is decreased to 10^{-11} s^{-1}. For lower strain rates (e.g. 10^{-12} s^{-1}), the folding layer exhibits viscous behavior and tensile stress is less likely to be produced. In contrast to the models with higher strain rate, the difference in the development of σ'_3 becomes ambiguous with the decline of strain rate, exemplified by the models with strain rate as 10^{-13} s^{-1} and 10^{-14} s^{-1}. The stress developments in the two layers exhibit a slight difference in the effective minimum principal stress. The σ'_3 of the fold limb with different strain rates increases with shortening with an analogous rate before 40% shortening. After that, σ'_3 decreases with shortening when the strain rate is high (> 10^{-12} sec^{-1}).

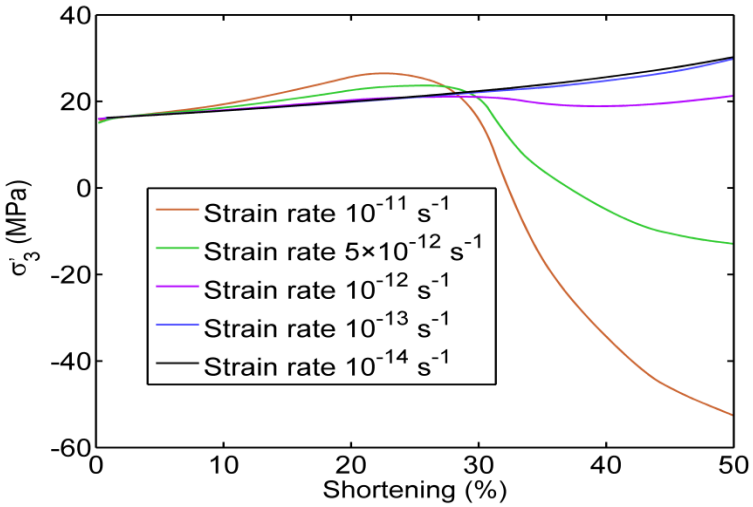

Figure 4.23 Effective minimum principal stress at the crest of the folding layer for different strain rates.

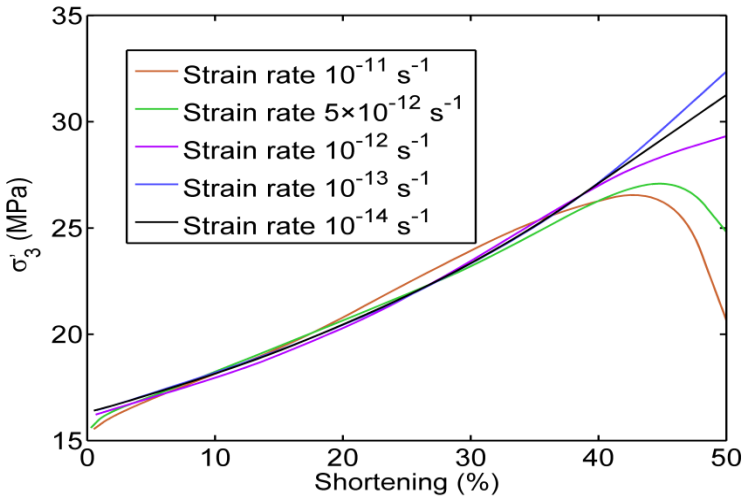

Figure 4.24 Effective minimum principal stress at the limb of the fold for different strain rates.

4.5. INFLUENCE OF OVERBURDEN PRESSURE

Numerical models for different overburden thicknesses are established to investigate the influence of overburden stress on fold development. The overburden pressure at depth z is given as (Jaeger and Cook, 1979):

$$P(z) = P_0 + g\int_0^z \rho(z)dz \tag{112}$$

where ρ (z) is the overlying rock density, g is acceleration due to gravity, and P_0 is the pressure at the surface which is assumed here to be zero (Jaeger and Cook, 1979). However, both the overburden depth and rock density are not constant when the fold develops. When the model is compressed horizontally, the conservation of model volume result in a significant increase in the overburden thickness. Thus, the overburden stress must be obtained from the simulation results instead of calculation. The relationship of the initial overburden depth fold of the folding layer and the finial overburden pressure is illustrated in Figure 4.32 as the initial overburden depth varies between 300 to 3000 meters. After 50% shortening, the overburden pressure increases from 4.69 MPa to 7.82 MPa for the lowest initial depth (300 m) and from 49.2 MPa to 97.1 MPa for the highest

initial depth (3000 m). The remaining material properties in these models are assigned as listed in Table 3.1.

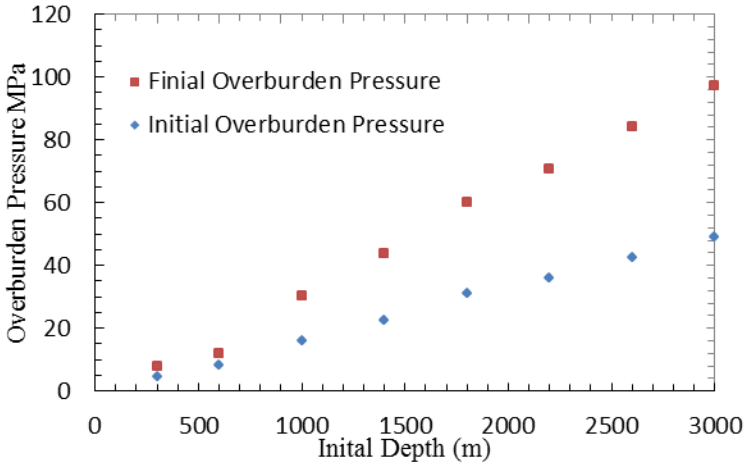

Figure 4.25 Overburden pressure at the crest of fold before and after shortening with different initial depth.

The temporal evolution of the minimum effective principal stress (σ'_3) at the crest and limb of the folding layer in a series of models with different initial overburden depth (300 meters to 3000 meters) are included in the following plots (Figure 4.33 to Figure 4.39). The stress development of the folding layer with initial overburden depth 1000 meters can be found in Section 4.1. The observations are summarized as follows:

(1) The stress histories at different locations in both crest and limb are close to each other before 27% shortening. During the following buckling period, the stress development at the crest and limb of the folding layer are highly dependent on the position for low depth (< 1000 meters). A significant decrease of σ'_3 can be observed for elements 1 and 2 at the crest of the fold for low initial depths (< 1000 meters). Considerable tensile stress is generated at the top of the crest in the folding layer when the initial overburden depth is only 300 meters.

(2) σ'_3 at different locations in both crest and limb become close to each other as initial depth increases (e.g. 3000 meters).

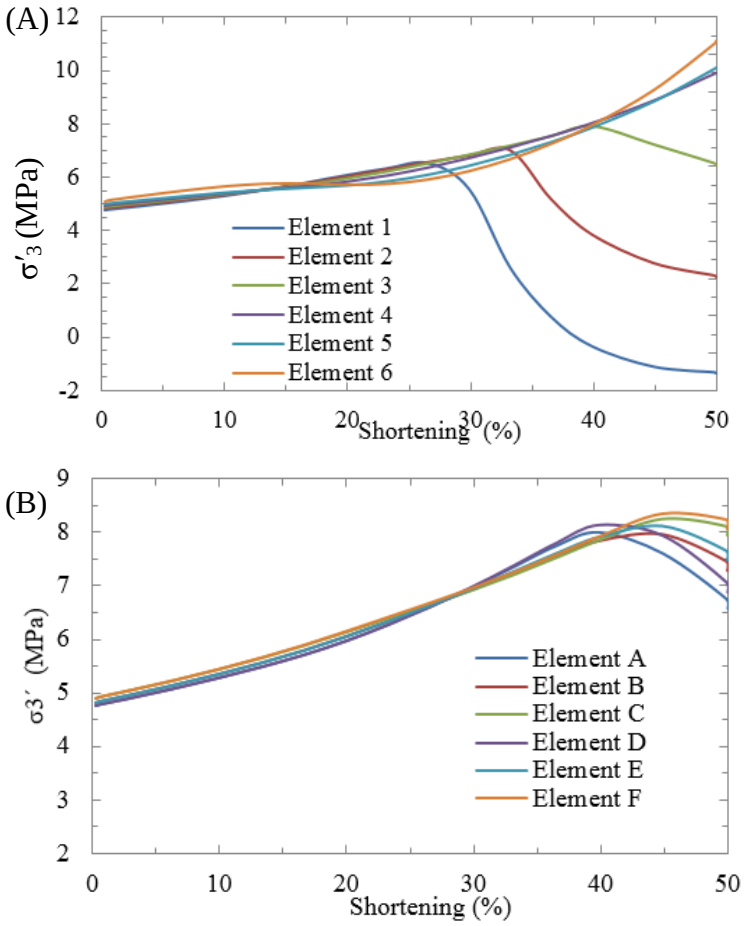

Figure 4.26 Stress history for numerical model with D=300m. (A) Effective minimum principal stress development at the crest of the folding layer with 300m initial overburden depth. Elements 1 to 6 are located as shown in Figure 4.1. (B) Effective minimum principal stress development at the limb of the folding layer with 300m initial overburden depth. Elements A to E are located as shown in Figure 4.1.

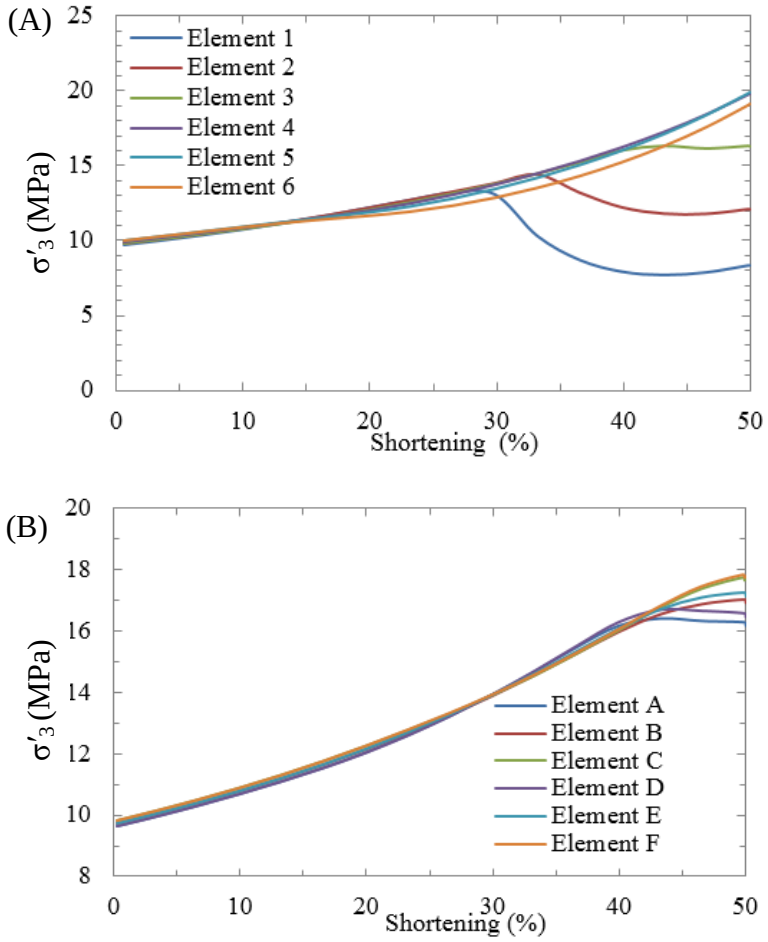

Figure 4.27 Stress history for numerical model with D=600m (A) Effective minimum principal stress development at the crest of the folding layer with 600m initial overburden depth. Elements 1 to 6 are located as shown in Figure 4.1. (B) Effective minimum principal stress development at the limb of the folding layer with 600m initial overburden depth. Elements A to E are located as shown in Figure 4.1.

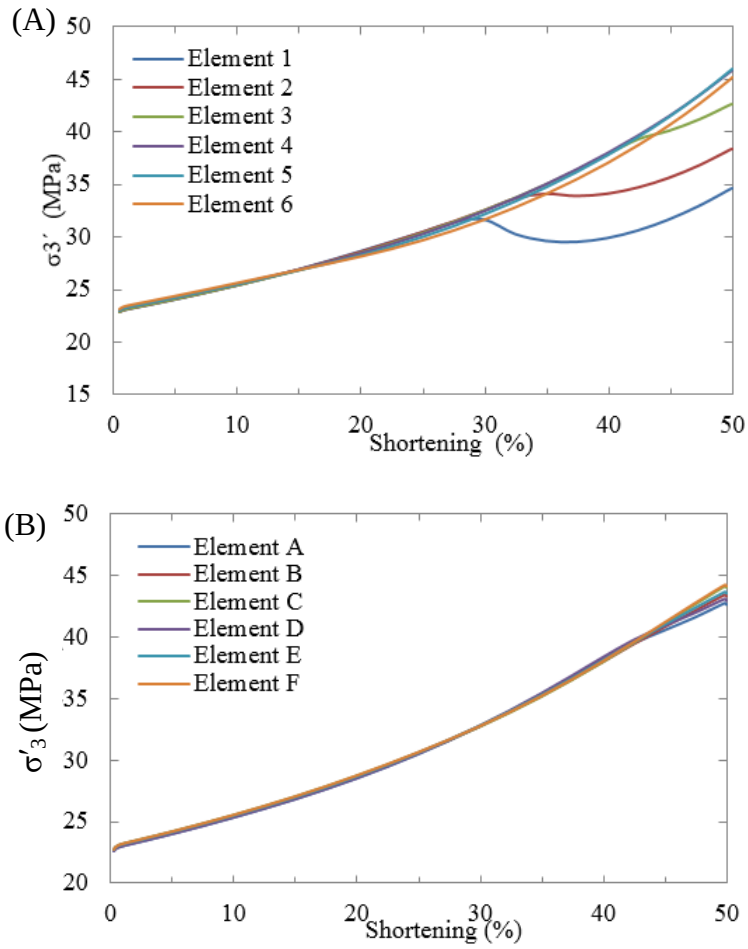

Figure 4.28 Stress history for numerical model with D=1400m. (A) Effective minimum principal stress development at the crest of folding layer with 1400m initial overburden depth. Elements 1 to 6 are located as shown in Figure 4.1. (B) Effective minimum principal stress development at the limb of the folding layer with 1400m initial overburden depth. Elements A to E are located as shown in Figure 4.1.

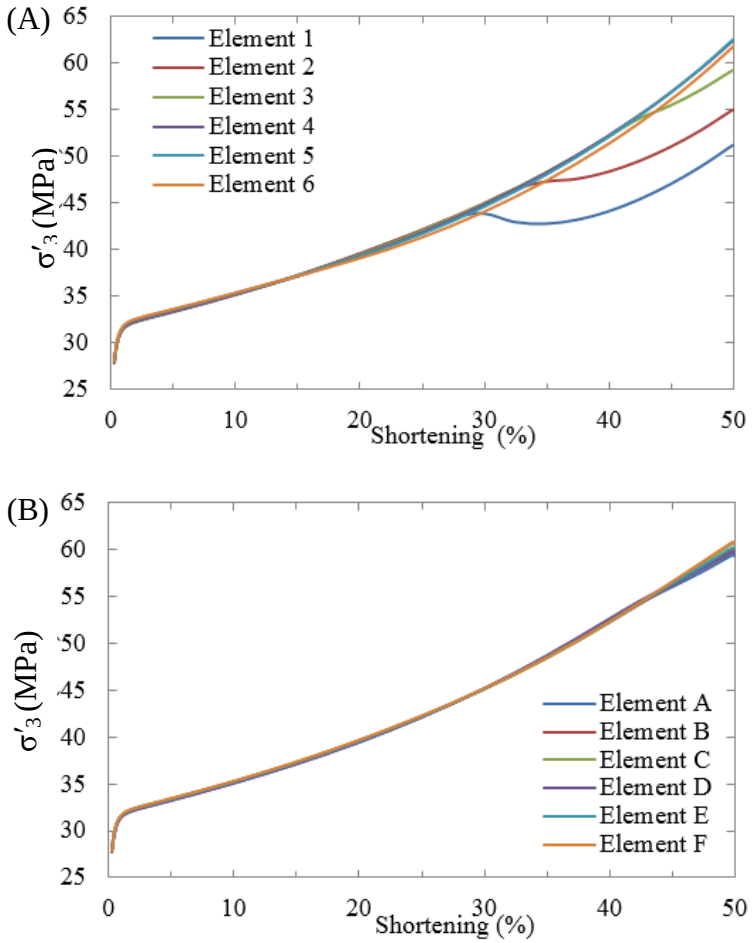

Figure 4.29 Stress history for numerical model with D=1800m. (A) Effective minimum principal stress development at the crest of folding layer with 1800m initial overburden depth. Elements 1 to 6 are located as shown in Figure 4.1. (B) Effective minimum principal stress development at the limb of the folding layer with 1800m initial overburden depth. Elements A to E are located as shown in Figure 4.1.

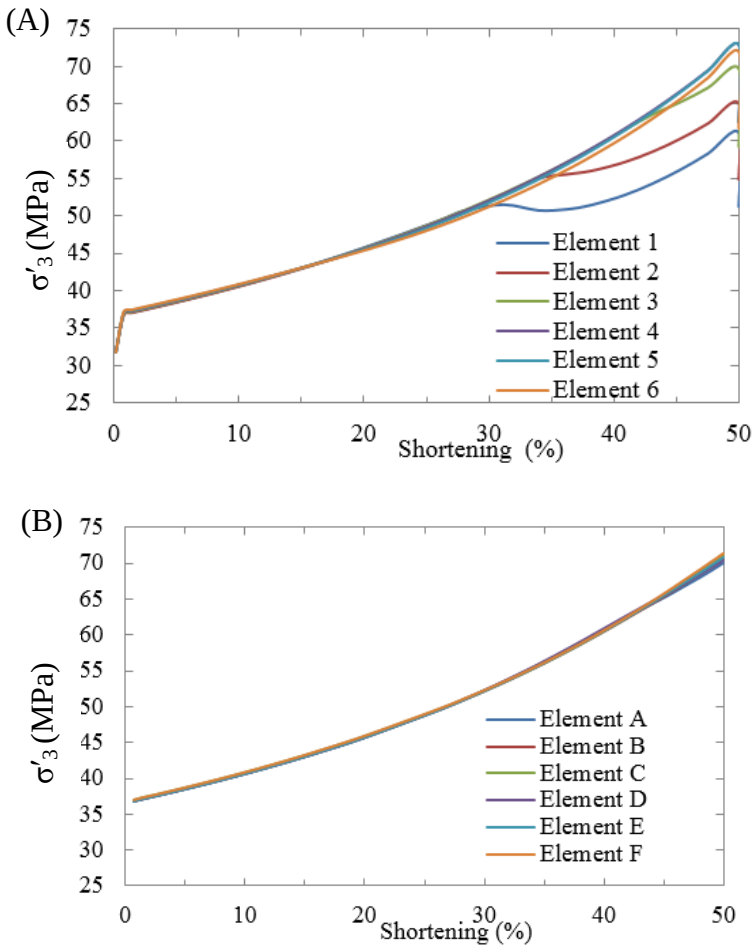

Figure 4.30 Stress history for numerical model with D=2200m. (A) Effective minimum principal stress development at the crest of folding layer with 2200m initial overburden depth. Elements 1 to 6 are located as shown in Figure 4.1. (B) Effective minimum principal stress development at the limb of the folding layer with 2200m initial overburden depth. Elements A to E are located as shown in Figure 4.1.

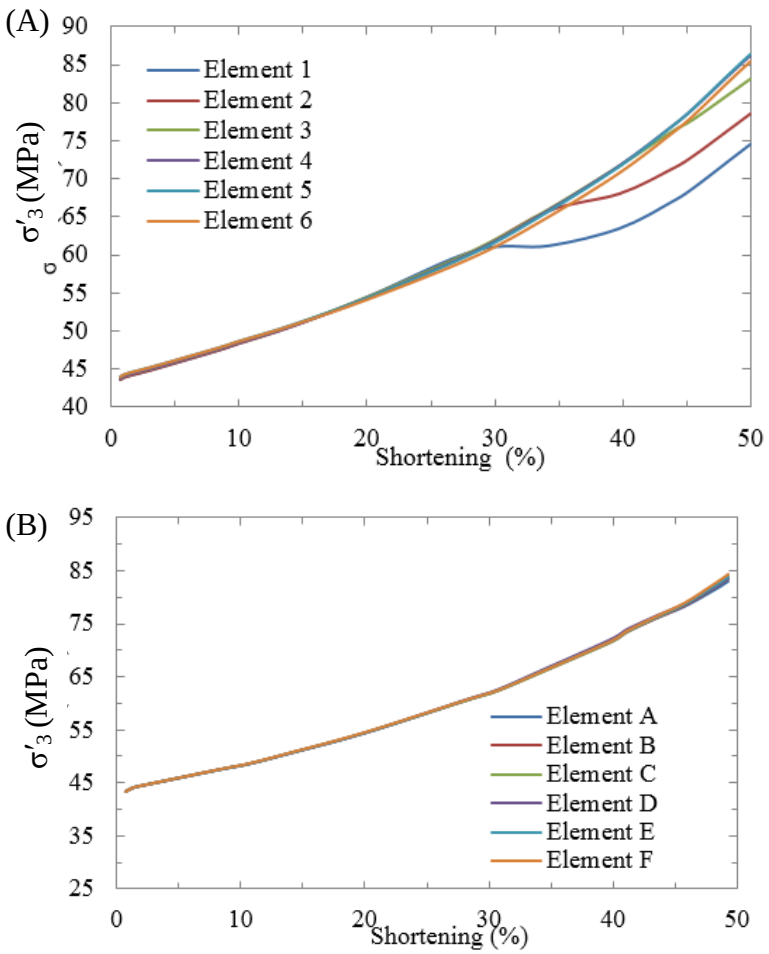

Figure 4.31 Stress history for numerical model with D=2600m.(A) Effective minimum principal stress development at the crest of folding layer with 2600m initial overburden depth. Elements 1 to 6 are located as shown in Figure 4.1. (B) Effective minimum principal stress development at the limb of the folding layer with 2600m initial overburden depth. Elements A to E are located as shown in Figure 4.1.

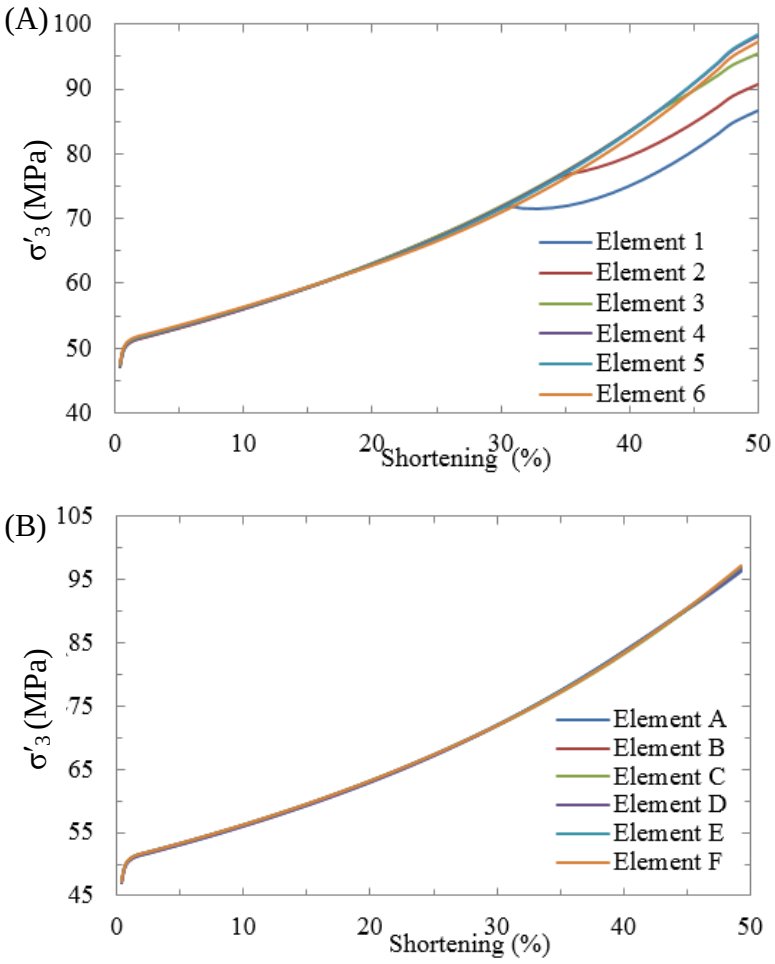

Figure 4.32 Stress history for numerical model with D=3000m. (A) Effective minimum principal stress development at the crest of folding layer with 3000m initial overburden depth. Elements 1 to 6 are located as shown in Figure 4.1. (B) Effective minimum principal stress development at the limb of the folding layer with 3000m initial overburden depth. Elements A to E are located as shown in Figure 4.1.

Figure 4.40 shows the effective minimum principal stress (σ'_3) development at the crest of the fold for different overburden pressures. The most interesting result of is that, the time when σ′3 reduction begins (near 30% shortening) appears to be independent from the overburden pressure. The existence of tensional stress after a specific amount of shortening is observed when the overburden pressure is limited to a certain magnitude, exemplified by the model with lowest overburden stress (7.82 MPa). For σ'_3 in the limb, a significant increase is observed as the depth and shortening increase. Tensile stress is not generated even when the initial depth is limited to 300 meters.

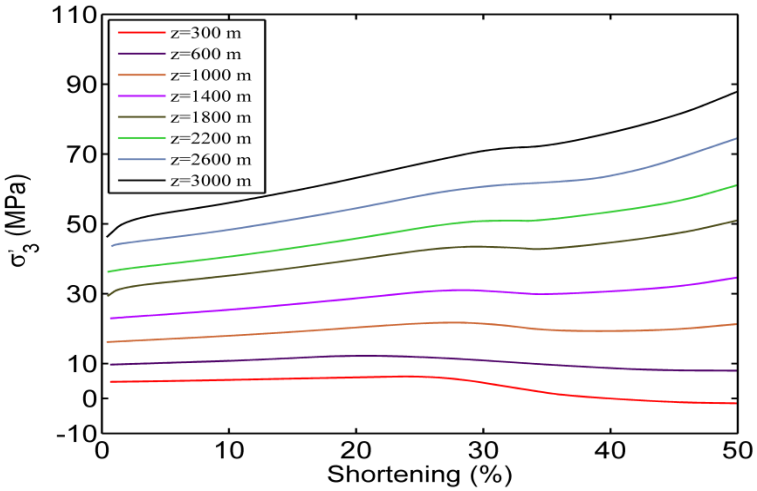

Figure 4.33 Effective minimum principal stress at the crest of foldthe foldfor different overburden stresses. The initial overburden depth changes from 300m to 3000m.

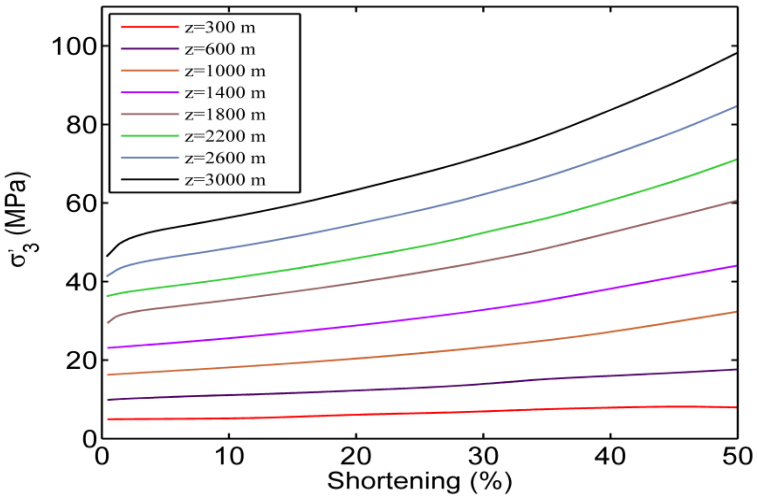

Figure 4.34 Effective minimum principal stress at the limb of foldthe fold for different overburden stresses. The initial overburden depth changes from 300m to 3000m.

4.6. INFLUENCE OF PERMEABILITY

Two different types of rock formations are used to assess the influence of permeability on fold stress history of the fold:

1. Homogeneous and anisotropic formations
2. Two layer (folding layer and matrix) and anisotropic formations

The horizontal permeability (k_h) of the models ranges from high values (10^{-13} m^2) characteristic for sandstone formations to low values (10^{-23} m^2) characteristic for shales (Jaeger and Cook, 1979). The remaining material properties in these models are assigned as listed in Table 3.1

4.6.1. Homogeneous and Anisotropic Formations. With a constant ratio (0.2) of vertical k_v over horizontal k_h the overall horizontal permeability in the model material varies from 10^{-13} m^2 to 10^{-23} m^2. Because the effective principal stress is the difference between the total principal stress and the pore pressure, the relationship between permeability and pore pressure is examined here as well.

The development of the minimum effective principal stress (σ_3') the and pore pressure (P_p) at the crest and the limb of the folding layer in a series of models with different permeabilities (10^{-13} m^2 to 10^{-23} m^2) are included in the following plots (Figure 4.42 to Figure 4.51). The stress development of the folding layer with a permeability of 10^{-15} m^2 can be found in Section 4.1. The observations are summarized as:

(1) The stress histories at different locations in the crest are close to each other before 27% shortening except for the lowest permeability (10^{-23} m^2), where tensile stress is generated throughout the folding layer crest before 10% shortening. During the following buckling period, the stress developments at the crest of the folding layer highly depend on the position. A significant decrease of σ'_3 can be observed at elements 1 & 2 of the fold crest. Considerable tensile stress is generated at the top of the crest in the folding layer when the permeability is low ($<10^{-18}$ m^2).

(2) The stress histories at different locations in the limb are close to each other when the permeability is higher than 10^{-21} m^2. A decrease of σ'_3 is observed at the limb of the folding layer after 40% shortening when the permeability is lower than 10^{-13} m^2. Tensile stress is generated throughout the folding layer limb before 20% shortening when the permeability is low ($<10^{-21}$ m^2).

(3) Except for the lowest permeability (10^{-23} m^2) model, the pore pressure histories at different locations in both crest and limb become close to each other and an increase of pore pressure both at the crest and limb with shortening can be observed. A

complex evolution of pore pressure is developed when the permeability is low (<10^{-21} m^2).

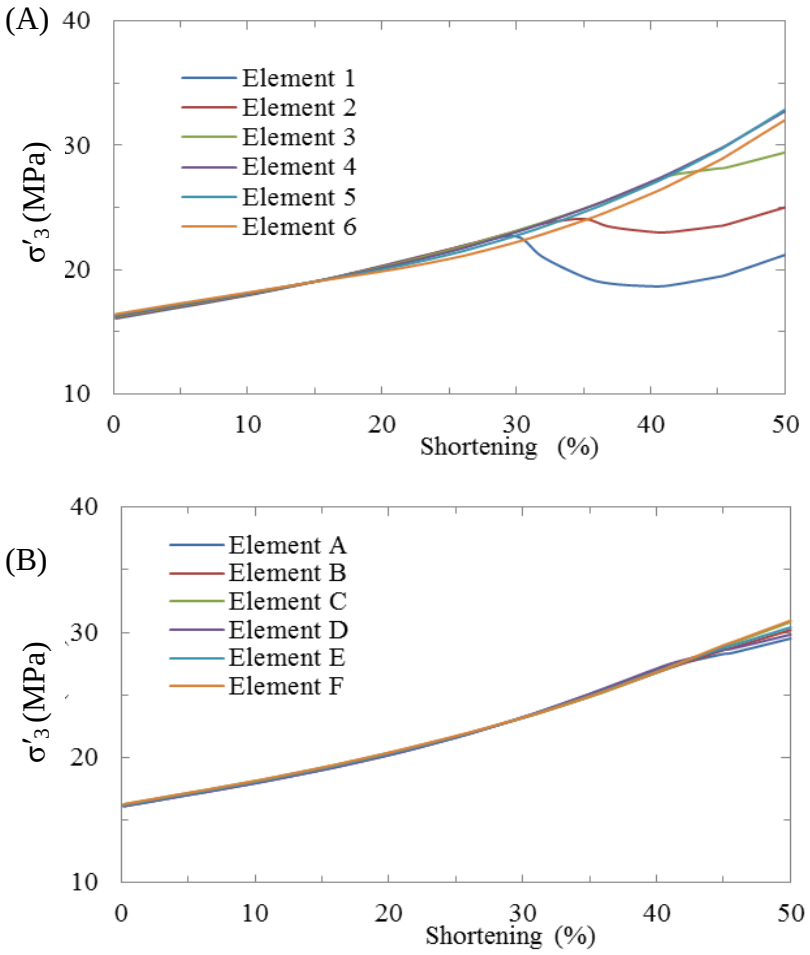

Figure 4.35 Stress history for numerical model with k=10^{-13} m^2. (A) Effective minimum principal stress development at the crest of the folding layer with permeability of 10^{-13} m^2. Elements 1 to 6 are located as shown in Figure 4.1. (B) Effective minimum principal stress development at the limb of the folding layer with permeability of 10^{-13} m^2. Elements A to E are located as shown in Figure 4.1.

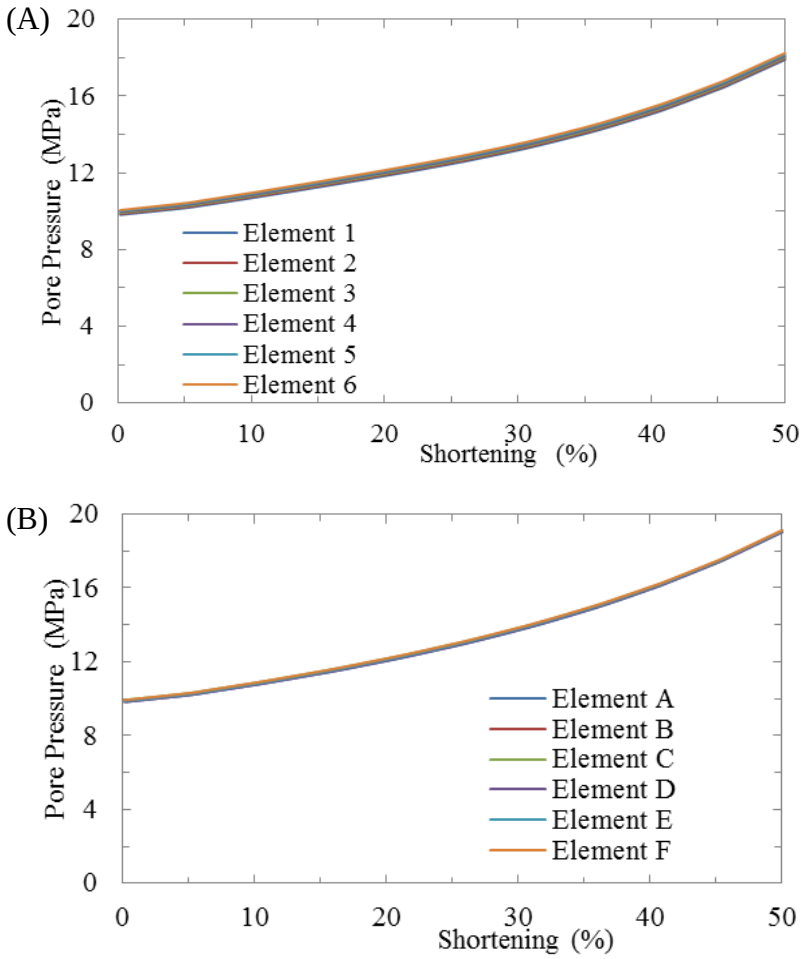

Figure 4.36 Pore pressure history for numerical model with k=10^{-13} m^2. (A) Pore pressure development at the crest of the folding layer with permeability of 10^{-13} m^2. Elements 1 to 6 are located as shown in Figure 4.1. (B) Pore pressure development at the limb of the folding layer with permeability of 10^{-13} m^2. Elements A to E are located as shown in Figure 4.1.

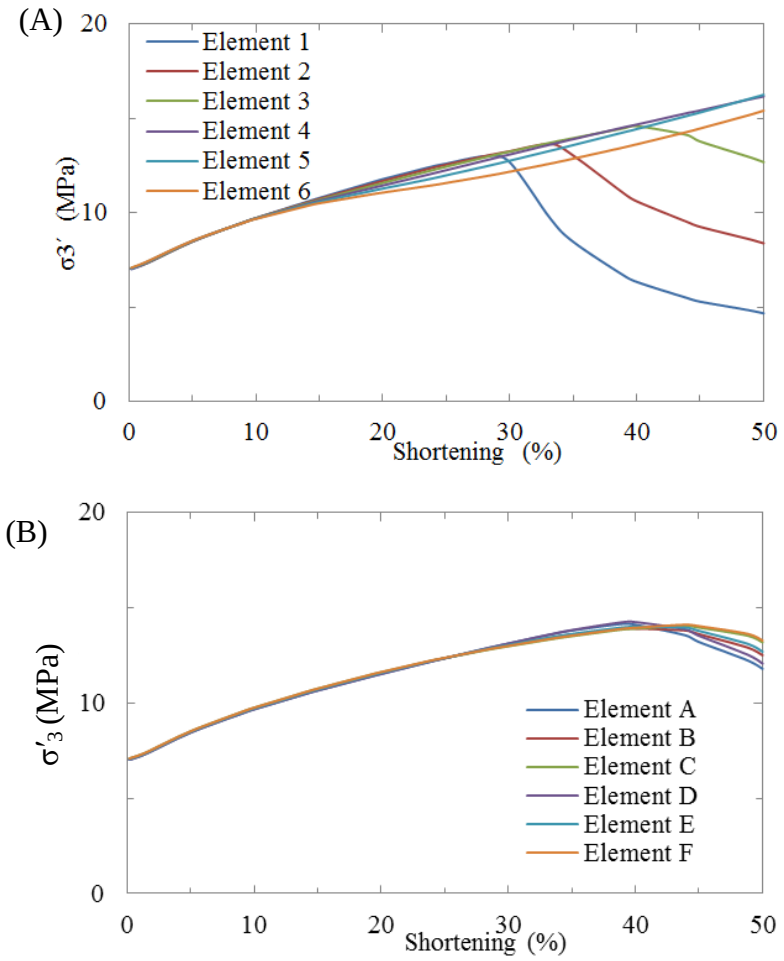

Figure 4.37 Stress history for numerical model with k=10^{-17} m^2. (A) Effective minimum principal stress development at the crest of the folding layer with permeability of 10^{-17} m^2. Elements 1 to 6 are located as shown in Figure 4.1. (B) Effective minimum principal stress development at the limb of the folding layer with permeability of 10^{-17} m^2. Elements A to E are located as shown in Figure 4.1.

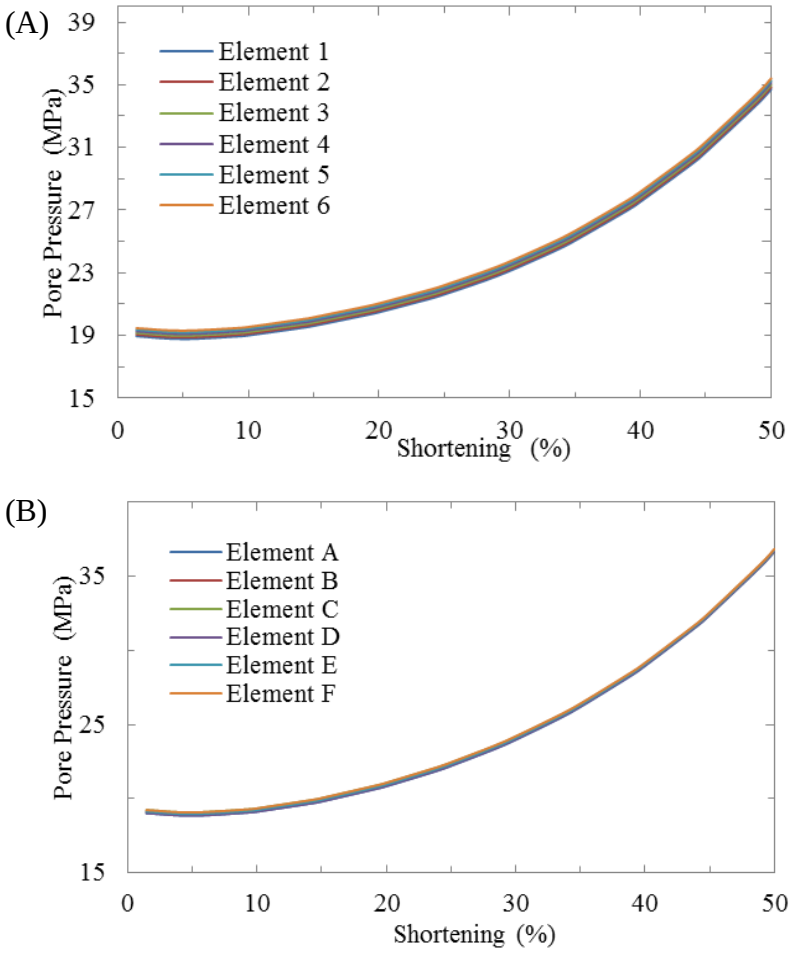

Figure 4.38 Pore pressure for numerical model with $k=10^{-17}$ m^2. (A) Pore pressure development at the crest of the folding layer with permeability of 10^{-17} m^2. Elements 1 to 6 are located as shown in Figure 4.1. (B) Pore pressure development at the limb of the folding layer with permeability of 10^{-17} m^2. Elements A to E are located as shown in Figure 4.1.

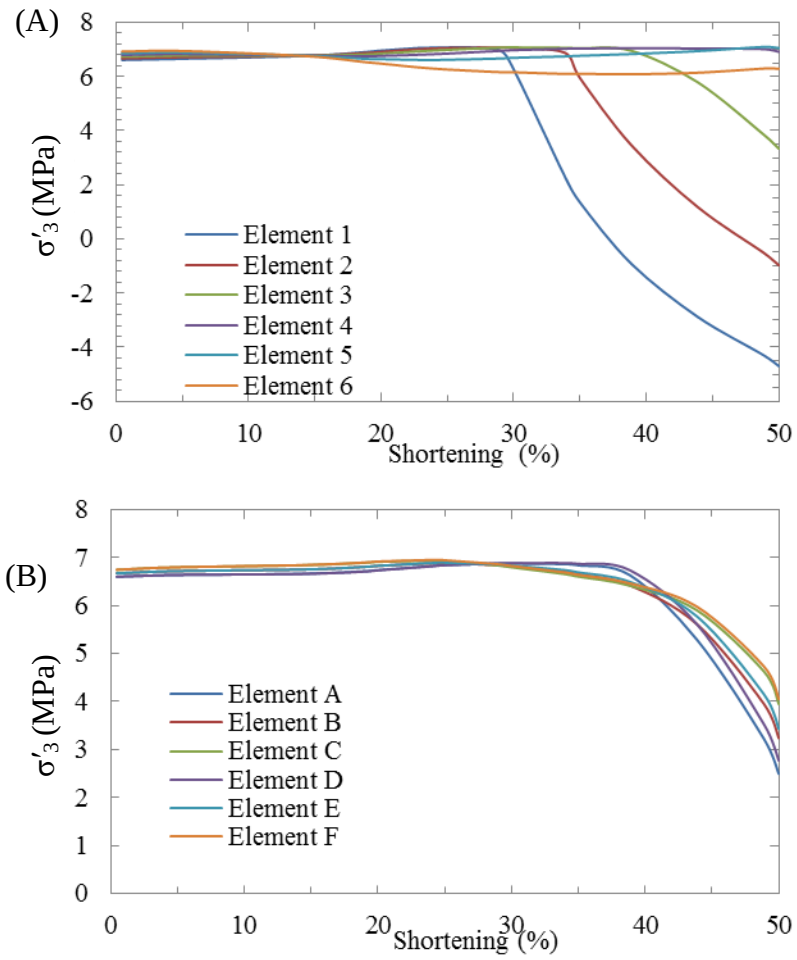

Figure 4.39 Stress history for numerical model with k=10^{-19} m^2. (A) Effective minimum principal stress development at the crest of the folding layer with permeability of 10^{-19} m^2. Elements 1 to 6 are located as shown in Figure 4.1. (B) Effective minimum principal stress development at the limb of the folding layer with permeability of 10^{-19} m^2. Elements A to E are located as shown in Figure 4.1.

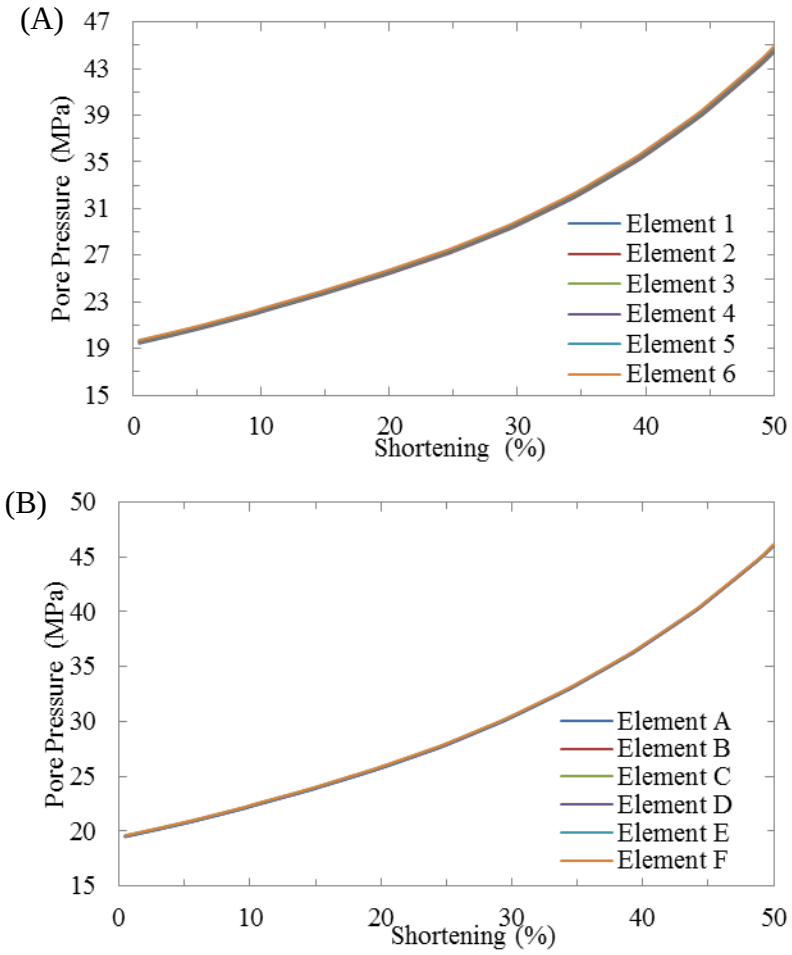

Figure 4.40 Pore pressure for numerical model with $k=10^{-19}$ m^2. (A) Pore pressure development at the crest of the folding layer with permeability of 10^{-19} m^2. Elements 1 to 6 are located as shown in Figure 4.1. (B) Pore pressure development at the limb of the folding layer with permeability of 10^{-19} m^2. Elements A to E are located as shown in Figure 4.1.

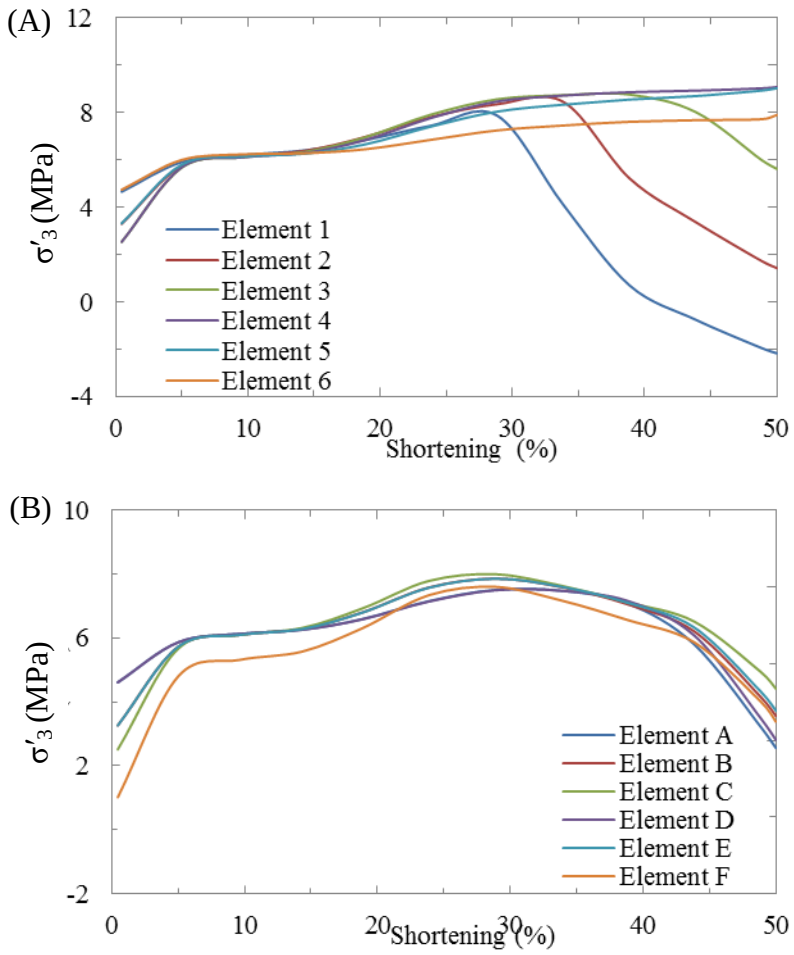

Figure 4.41 Stress history for numerical model with k=10^{-21} m^2. (A) Effective minimum principal stress development at the crest of the folding layer with permeability of 10^{-21} m^2. Elements 1 to 6 are located as shown in Figure 4.1. (B) Effective minimum principal stress development at the limb of the folding layer with permeability of 10^{-21} m^2. Elements A to E are located as shown in Figure 4.1.

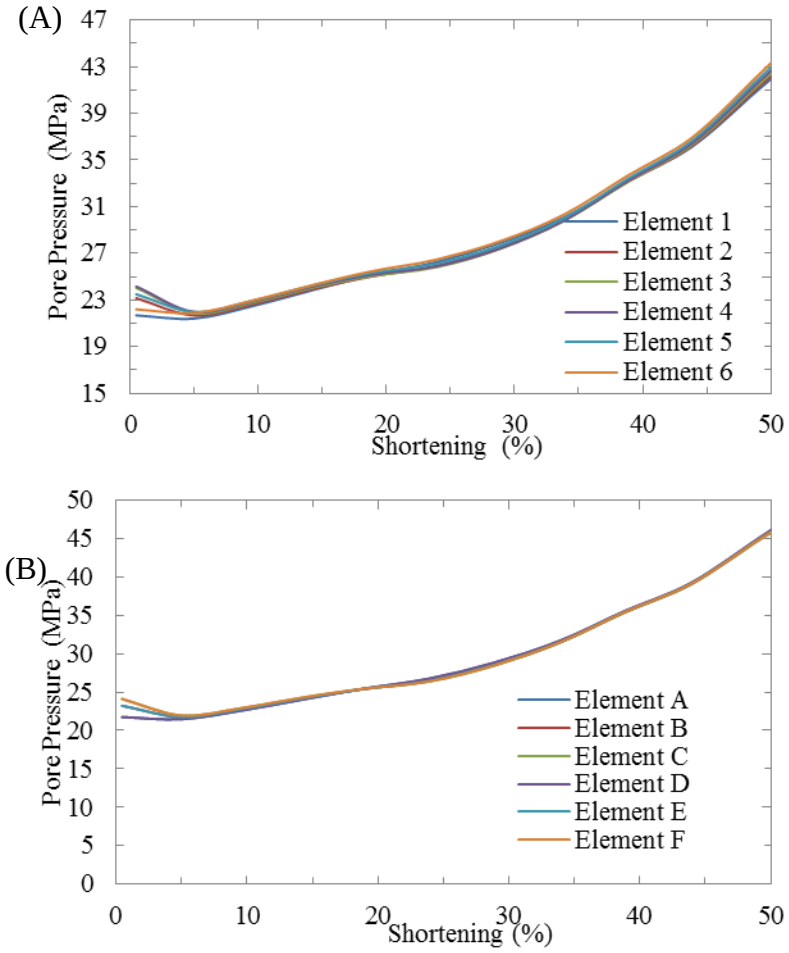

Figure 4.49 Pore pressure for numerical model with $k=10^{-21}$ m^2. (A) Pore pressure development at the crest of the folding layer with permeability of 10^{-21} m^2. Elements 1 to 6 are located as shown in Figure 4.1. (B) Pore pressure development at the limb of the folding layer with permeability of 10^{-21} m^2. Elements A to E are located as shown in Figure 4.1.

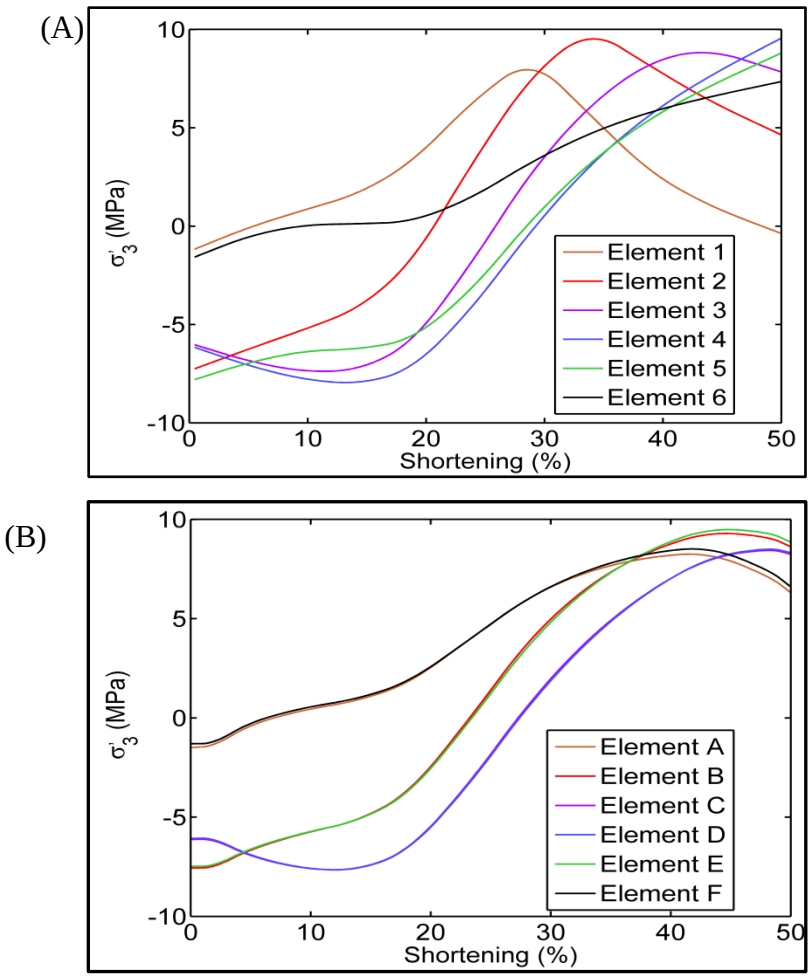

Figure 4.420 Stress history for numerical model with $k=10^{-23}$ m^2. (A) Effective minimum principal stress development at the crest of the folding layer with permeability of 10^{-23} m^2. Elements 1 to 6 are located as shown in Figure 4.1. (B) Effective minimum principal stress development at the limb of the folding layer with permeability of 10^{-23} m^2. Elements A to E are located as shown in Figure 4.1.

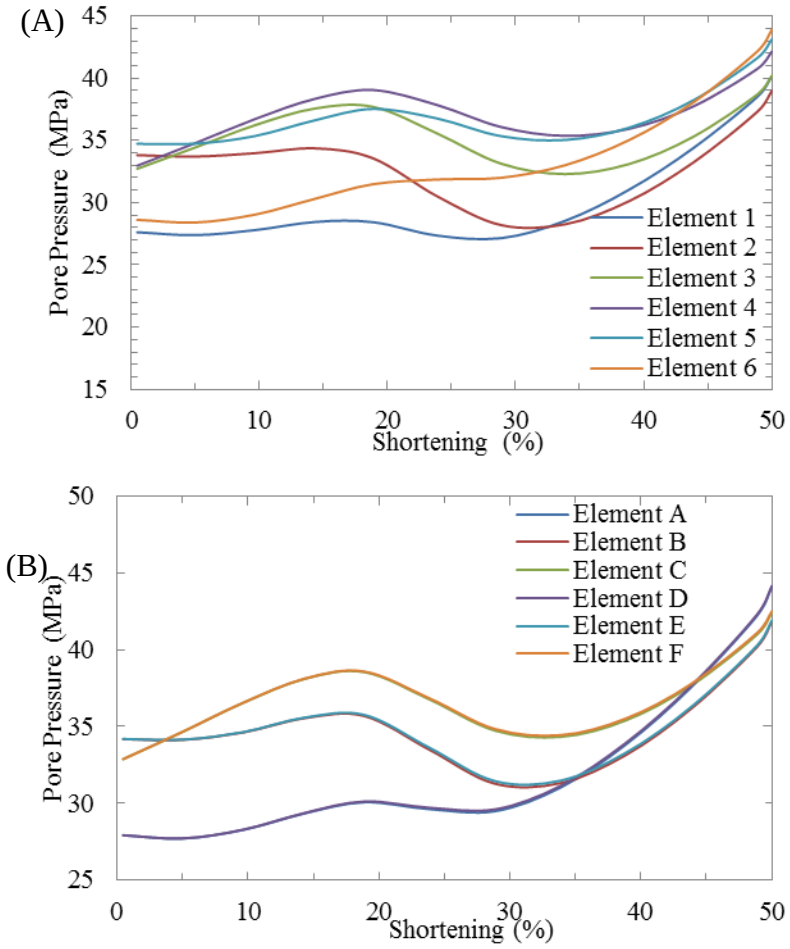

Figure 4.431 Pore pressure for numerical model with k=10^{-23} m^2. (A) Pore pressure development at the crest of the folding layer with permeability of 10^{-23} m^2. Elements 1 to 6 are located as shown in Figure 4.1. (B) Pore pressure development at the limb of the folding layer with permeability of 10^{-23} m^2. Elements A to E are located as shown in Figure 4.1.

As Figures 4.42 to4.51 show, different permeabilities result in diverse pore pressure evolutions. The pore pressure evolution is close to the theoretical, hydrostatic prediction when k is high (>10^{-16} m^2). For low k (<10^{-16} m^2), the pore pressure becomes larger than hydrostatic and significant over-pressure is generated during the early stages of deformation (see Figure 4.52). For the same amount of shortening, low permeability leads to high pore pressure both at the crest and the limb. However, the pore pressure evolution becomes independent of the changing of permeability when the permeability is smaller than 10^{-20} m^2.

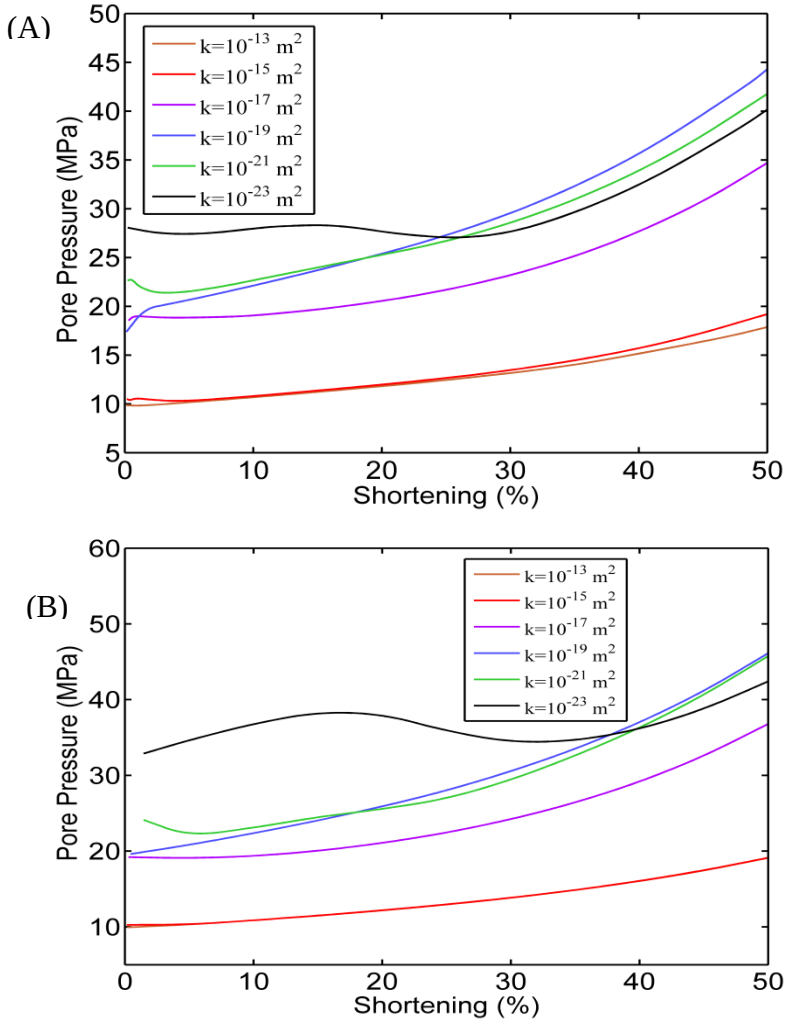

Figure 4.442 Pore pressure evolution under different permeabilities. (A) Pore pressure evolution at the crest of fold for different k. (B) Pore pressure evolution at the limb of the fold for different k.

The effective minimum principal stress drops significantly as the horizontal permeability (k) decreases and tensile stress can be produced at the crest, as illustrated in Figure 4.53*A*. The existence of tensional stress after ~ 37% shortening is observed when k is limited to certain magnitude, as exemplified by the model with k = 10^{-19} m^2. Figure 4.53*A* also suggests that the beginning of the drop of σ'_3 at the crest is around 27% shortening is independent of k. For the limb of the folding layer tensile stresses are

observed during the early shortening periods (<30% shortening) for low permeability (10^{-23} m^2; see Figure 4.53*B*). In summary, the σ'_3 magnitude evolution shows that the dependency on permeability is both highly nonlinear and non-uniform for low permeabilities (e.g. $<10^{-17}$ m^2), especially after 27% shortening. This observation can be explained by the relations between pore pressure (P_p) and effective principle stress (σ'_3). Comparing the associated fluid velocity vectors for k of 10^{-19} m^2 and 10^{-23} m^2 (see Figure 4.54A, C), it can be concluded that the pore pressure in the folding layer is hydraulically connected to the overburden for $k_h = 10^{-19}$ m^2. Thus the saturated fluids are expelled at the top of the folding layer into the matrix due to the layer parallel compaction (see Figure 4.54A) and the P_p distribution is related to the depth (see Figure 4.54B). In contrast, only limited fluids are exchanged between the matrix and the folding layer for lower k of 10^{-23} m^2, which leads to the geometry related P_p distribution (see Figure 4.54C, D). The P_p at the top of the crest for $k = 10^{-23}$ m^2 (38 MPa) is lower than the P_p at the same location for $k = 10^{-19}$ m^2 (43 MPa).

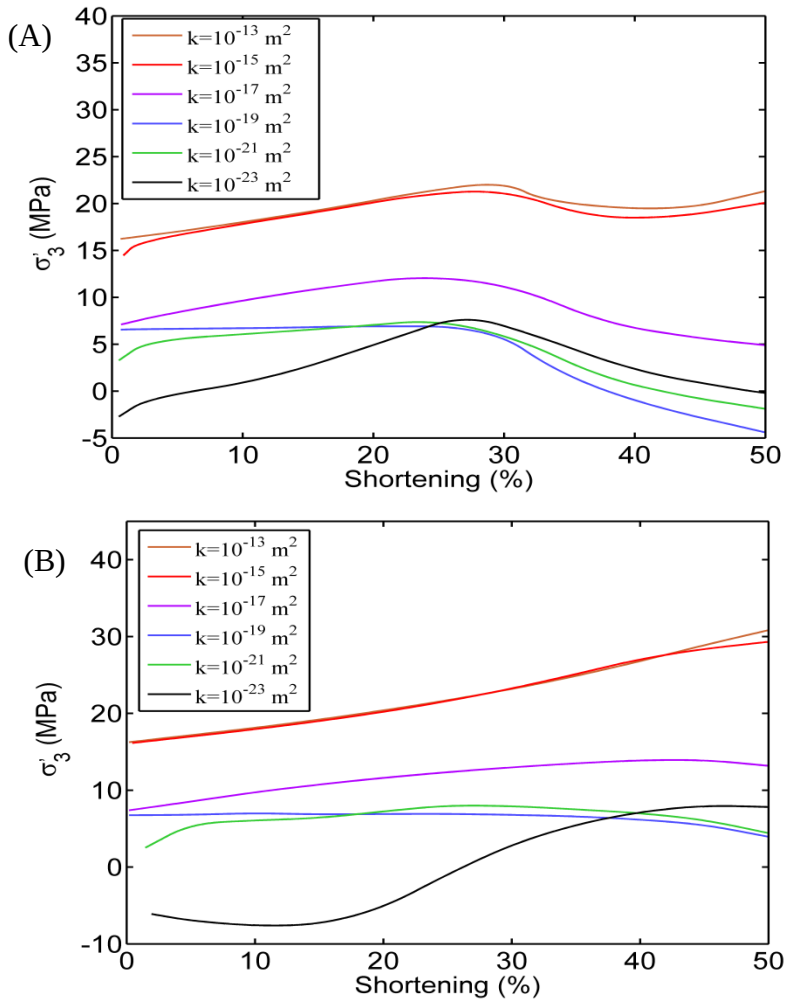

Figure 4.453 Stress evolution with different permabilities. (A) Effective minimum principal stress evolution at the crest of fold development with shortening with different k_h. (B) Effective minimum principal stress evolution at the limb of the fold for different k.

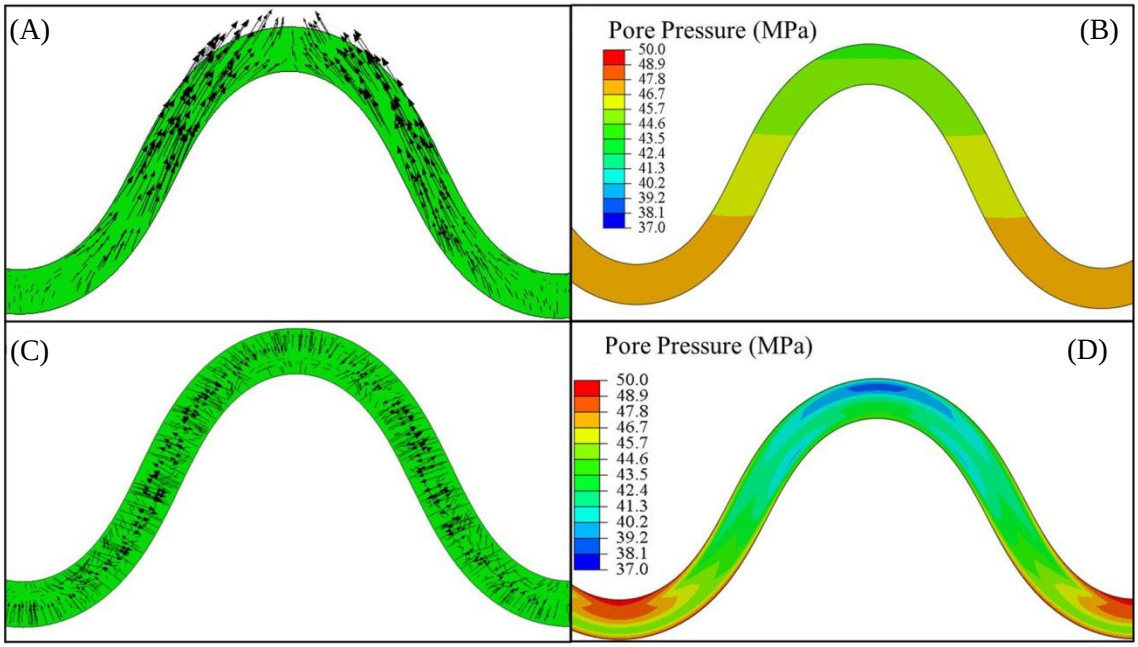

Figure 4.46 Comparison of fluid velocity and pore pressure with different permeabilities. (A) Fluid velocity vectors for 10^{-19} m^2. (b) Pore pressure magnitude for 10^{-19} m^2 exhibits depth related relation. (C) Fluid velocity vectors for 10^{-23} m^2 .(D) Pore pressure magnitude for 10^{-23} m^2 exhibits is not depth related.

4.6.2. Two Layer (folding layer and matrix) and Anisotropic Formations.

Another way of simulating anisotropic permeability in rock can be obtained by establishing different permeabilities in the folding layer and the matrix. With the same ratio of vertical permeability (k_v) over horizontal permeability (k_h), the k_h in the model material varies from 10^{-13} m^2 to 10^{-23} m^2 in folding layer and matrix, respectively. The remaining material properties in these models are assigned as listed in Table 3.1

Figure 4.55 shows the effect of k_h for the layer and the matrix's on σ'_3 evolution for 30% and 50% shortening. In this case, all the models have the same initial geometry and material parameters except for k_h. The change in σ'_3 (at the same amount of shortening) is mainly dominated by the matrix's k_h. Increasing matrix permeability from 10^{-13} m^2 to 10^{-19} m^2 results in a considerable increase of σ'_3. Tensile stresses are not occurring before 30% shortening even for the low permeability model. After 40% shortening, tensile stress is observed on the top of the crest with low k_h ($<10^{-17}$ m^2). Another important observation form this plot is that the tensile stress on the fold crest of

the fold for low matrix permeability declines with the layer permeability decrease, which is due to the high pore pressure in folding layer.

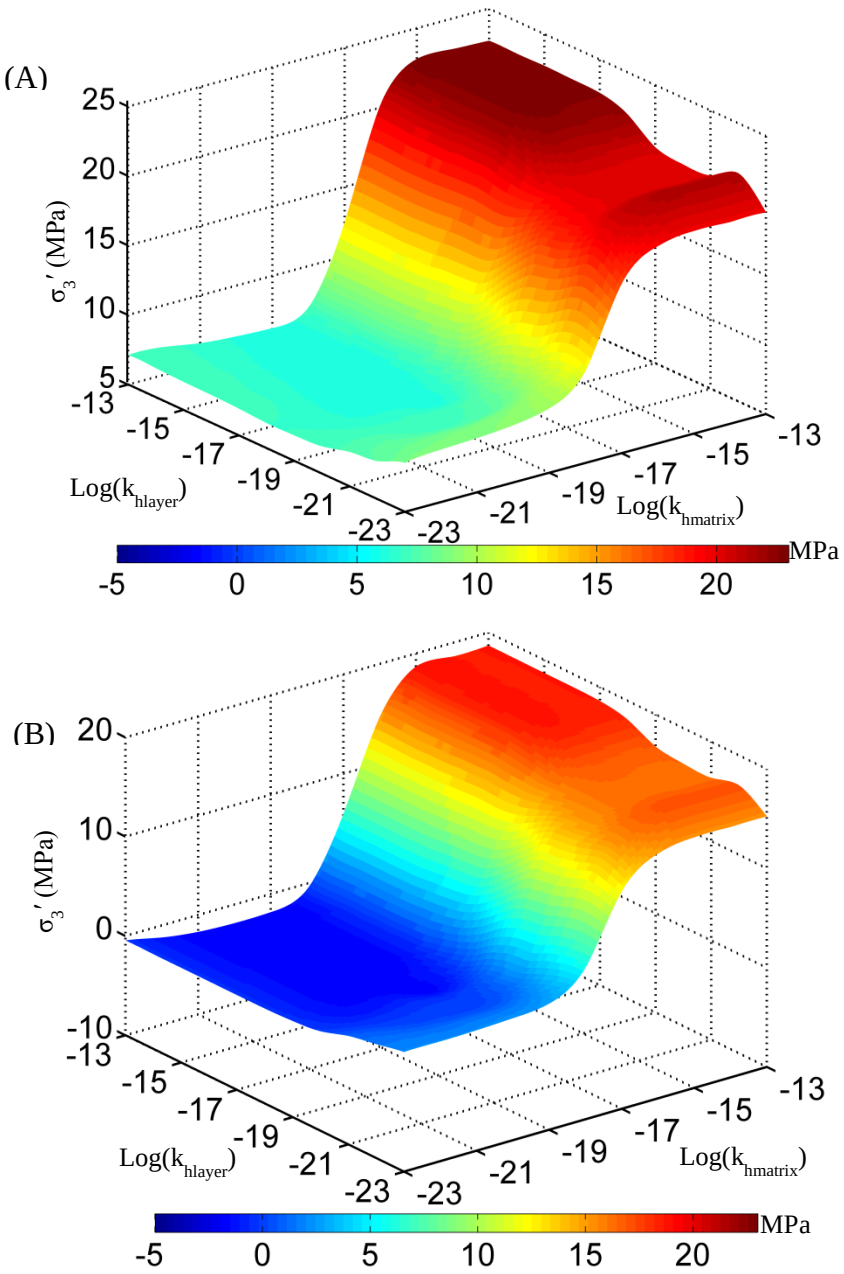

Figure 4.55 3D plot of effective minimum principal stress on foldthe crest of the fold for different permeabilities for models subjected to a different amount of shortening. (A) 30% shortening. (B) 40% shortening. (C) 50% shortening

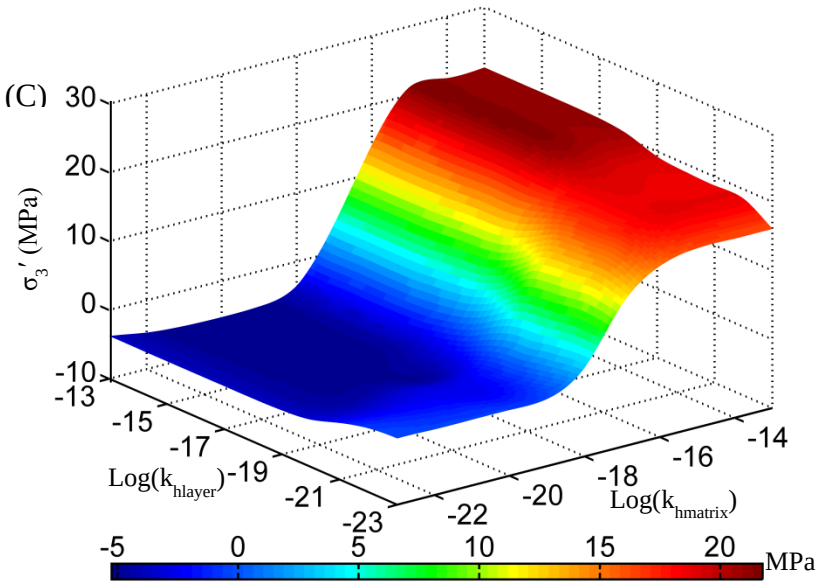

Figure 4.47 3D plot of effective minimum principal stress on foldthe crest of the fold for different permeabilities for models subjected to a different amount of shortening. (A) 30% shortening. (B) 40% shortening. (C) 50% shortening. (cont)

5. DISCUSSION

The 2D plane strain numerical modeling approach presented here is used to provide a better understanding of the initiation and occurrence of tensile failure observed in folded outcrops (e.g. Stearns, 1964; Bergbauer and Pollard, 2004) by studying the evolution of the state of stress during buckle fold development. It is generally assumed that these fractures are the results of layer parallel tensional strain above the neutral surface during the evolution of the bending/buckling processes (Ramberg, 1964, Ramsay, 1967; Price and Cosgrove, 1990). Thus, considering the relations between stress and strain in an elastic material, the locations of tensile strain above the neutral surface are commonly assumed to generate tensile fracture.

However, some recent studies show that there is no significant correlation between fracture density and folded surface curvature (e.g. Smart et al., 2009; Pearce et al., 2010), which indicates that the strain based analysis may not be sufficient to interpret fracture characteristics such as density and orientation. Previous numerical modeling of folding applies viscoelastic material without considering gravity and pore pressure, which does not yield realistic stress magnitudes (e.g. Smart et al., 2009). The in-situ state of stress is always compressive due to the significant weight of the overburden when gravity is considered (Turcotte and Schubert, 2002). Tensile stress due to buckling is hard to develop even with considerable tensile strain in curvature based modeling approaches. Unlike the influence of gravity, the presence of pore fluid increases the possibility of tensile fractures even in regions undergoing relatively low strain (Hooker et al., 2009; Olson et al., 2006).

This study applies two-dimensional numerical models which simulate the buckling process under realistic in-situ stress and strain conditions. As the main focus is concentrated on the initiation/occurrence of mode I (tensile) fractures (either bedding perpendicular or parallel), the 2D plane strain assumption is considered accurate. The comparison and general agreement to Biot's study validates the modeling approach (see Section 3.6). The sensitivity analysis of the influence of different model parameters (competence contrast, viscosity, strain rate, overburden, and permeability) on the development of fold structures and resulting stress evolution has been performed. For

natural fold-related structures, fractures are generated when the layer-parallel stress becomes tensile and exceeds the tensile strength. Based on this study, the tensile failure associated to the physical process of buckling may only be initiated for special conditions. The modeling results from the show that either large differences in rock properties competence (i.e. Young's modulus and viscosity) or low overburden pressures are required to initiate tensile failure at the crest of buckle folds during their development. Another condition which results in tensile stress at the top of the fold crest is that of fast strain rates ($>5\times10^{-12}$ s^{-1}); however this is not commonly observed in field. Most geologic deformation processes such as folding are thought to occur at average strain rates between 10^{-12} s^{-1} and10^{-14} s^{-1} (Twiss and Moores, 2007). The last tested parameter of permeability is discovered to have a governing role on the pore pressure evolution. With the overpressure generated throughout the folding layer, tensile failure at the limb of folding layer is possible to develop during early stage of bulking and tensile failure at the crest of fold hinge zone is likely to develop during the later periods of bulking.

These findings certify the conclusion of Lemiszki et al. (1994) about the importance of strain rate, overburden, pore pressures and viscosity. Based on the finite element model results of Dieterich and Carter (1969), Lemiszki et al. concludes that mode I fractures are possible to develop from certain combinations of the above variables. For example, the existence of overpressure and the amount of shortening are the key parameters for tensile failure to occur at a certain depth. Lemiszki et al.'s (1994) results show that the minimal ratio of the fluid pressure to the vertical pressure is 0.73 for a fold with 3km depth. The 2D numerical modeling study exhibited in this thesis shows that the evolution of overpressure during the layer-parallel shortening is highly depended on the rock permeability. For the example of a folding layer at a depth of 1891 meters with amplitude of 125.1 meters, the maximum permeability of the matrix rock that can cause tensile fractures on the top of the fold crest is 10^{-19} m^2. For higher permeability models, overpressure is either absent or insignificant and the compression caused by the vertical stress overcomes the extensional stress caused by the tensional strain due to the buckling process. Thus, tensile failure is unlikely to be generated even with considerable tensional strain developed on the top of the crest of the fold.

This research also indicates that sufficient shortening (e.g. >27%) and large amplitudes (e.g. > 100m) are necessary for the initiation of tensile stress on the top of crest. The orientations of tensile failures developed under the special situations at the top crest are perpendicular to σ'_3 and parallel to the fold axis of the hinge zone. This finding is in agreement with Reber et al.'s (2010) observations, which suggest that Mode I (tensile) fractures are parallel to the fold axes in high amplitude folds.

The 2D numerical simulation results presented here show that the process of buckling under compressional region is not a major factor for the initiations of tensile failure on folded layers if realistic sedimentary rock parameters are applied to the models. Furthermore, the tensile fractures at the folds limb which is observed either perpendicular or parallel to the fold axis (e.g. Silliphant et al., 2002; Bergbauer and Pollard, 2004) only develop during the early shortening period (<10% shortening) for very low permeability models (10^{-23} m^2).

Since these conditions certainly do not represent the general development histories for the majority of buckle folds exhibiting tensile failure and fail to explain tensile failure at the folds' limbs, this numerical modeling study raises the question that whether buckling under compressional stress regimes is a dominating factor for the initiation of tensile failure at depths. These commonly observed joint sets and tensile failures which occur at considerable depth (e.g. > 1km) fail to be explained by buckling alone. One of the possible causes to explain the joints sets is that they are caused by overpressure development during sedimentation and exist before folding (Price and Cosgrove, 1990). Another possibility is that these joints are caused by erosion and exhumation and defined as a post buckling phenomena (e.g. Price, 1966; Hancock and Engelder, 1989; Bourne, 2003). Since the simulation of tensile failure during pre-folding is beyond the capabilities of the numerical code applied, only the influence of erosion and exhumation is simulated.

5.1. EROSION and EXHUMATION

Numerical models to study the process of erosion and exhumation after the horizontal shortening have been established. Erosion and exhumation are crucial to the

folding layer's state of stress as the weight of overburden decreases significantly during the progress. An additional load step has been applied in the numerical models to simulate the process of erosion and exhumation by reducing the overburden weight over a reasonable geological time scale. Since it is impossible to continuously remove layers of elements over geologic time scales in the finite element model, the erosion/exhumation process is simulated by a continuous decrease of the weight of the overburden. The constant erosion/exhumation rate is chosen as 0.1 mm/yr (Twiss and Moores, 2007) by linearly decreasing the gravitational acceleration magnitude of the overburden over a period of 37 million years. Since the erosion/exhumation is assumed as a post-fold deformation, only vertical in-plane displacements are enabled. Considering the importance of pore pressure evolution during this process, two different permeabilities scenarios are considered:

(1) a high permeability model ($k = 10^{-15}$ m^2) with an initial overburden thickness of 3000 m;

(2) a low permeability model ($k = 10^{-19}$ m^2) with an initial overburden thickness of 1000 m.

5.1.1. High Permeability Model

The geometry of the high permeability model is shown in Figure 5.1. For this two-step approach, a competent viscous layer is compressed by 50% shortening with an initial depth of 3000 m, followed by a steady exhumation and erosion process for 37 million years (see Figure 5.1). After 50% shortening, the overburden depth of the folding layer increases to 5366.7 meters. The exhumation and erosion rates (both 0.1mm/year) are assumed constant and both the left and right boundaries remain fixed during this process (see Figure 5.1B). Hydrostatic pore pressure distributed in the overburden also decreases linearly with the decreasing of the gravitational acceleration magnitude. After 37 million years, the overburden of the folding layer has decreased to 1622.7 meters (see Figure 5.1A). Thus, the stress in the fold structure develops under the influence of both the vertical extension and the linear decrease in overburden pressure.

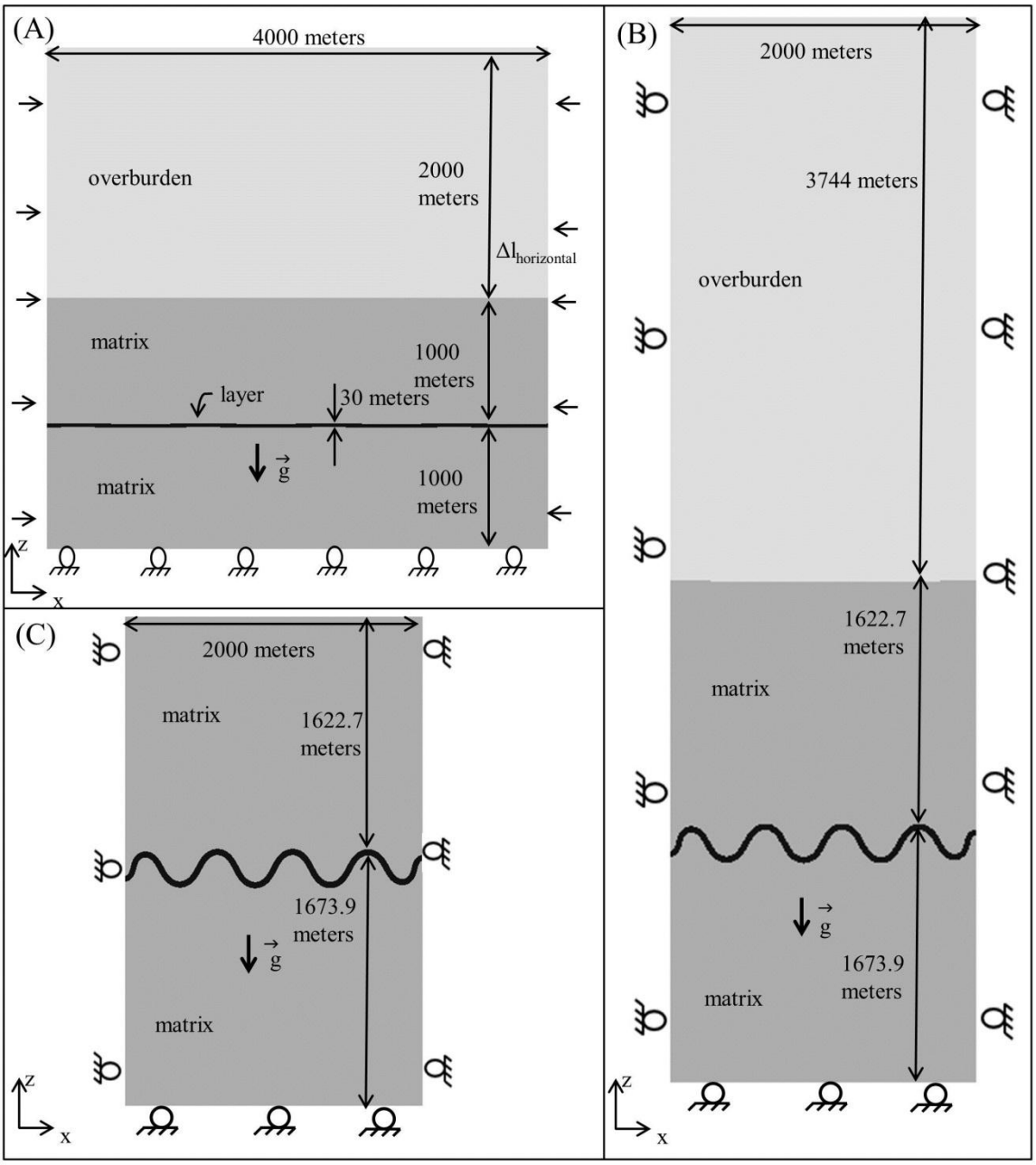

Figure 5.1 Model setup for erosion/exhumation study. (A) Model setup for the high permeability erosion/exhumation study. The folding layer is embedded in a 1000 m thick high permeability matrix. The remaining overburden has the same high permeability. (B) Model geometry and dimensions after 50% shortening. (C) Model geometry after erosional load step resulting in surface topography.

The results for this high permeability model (Figure 5.2A) show that the erosion/exhumation process causes σ'_3 to decrease to tensile magnitudes when the initial σ'_3 magnitudes at the fold crest are compressive due to buckling. Around 20.61 Ma, when the overburden depth is reduced to 3275 meters, tensile failure occurs at the top of the crest with an effective vertical stress of 60 MPa.

For an equivalent model which is only subjected to horizontal compression, an overburden pressure of 60.1MPa is developed in a model with 1800 meters initial depth and 3290.5 meters overburden depth (see section 4.4). By comparing the results from the two models, σ'_3 (-0.1MPa) at the top crest of the erosion/exhumation model is much lower than σ'_3 (60.1MPa) at the top crest of the folding layer with shortening only. The reduction of the effective minimum principle stress ($\Delta\sigma'_3$) due to the removal of overburden ($\sigma'_1/\sigma'_{vertical}$) is also larger than the result calculated from the uni-axial strain conditions. Under the assumption of uni-axial strain boundary condition, $\Delta\sigma'_3$ is obtained by (Turcotte and Schubert, 2002):

$$\Delta\sigma'_3 = \sigma'_3 - \frac{\nu}{1-\nu}\Delta\sigma'_1 \tag{112}$$

Eroding an equivalent overburden depth of 2366 meters, the decrease of $\sigma'3$ is as big as 17.77 MPa in a horizontally layered model (uni-axial strain boundary condition). Figure 5.2A shows that $\Delta\sigma'_3$ at the top of crest is 87.1 MPa after 20.61 million years erosion/exhumation. A large overburden depth remains at the onset of tensile failure, e.g. 3277 meters for the crest and 3411 meters for the limb.

The decrease rates of σ'_3 strongly depend on the elements locations, e.g. element 1 develops tensile stress after 20.61 million years (Ma), and element 4 develops tensile stress after 33.32 Ma. A similar decrease of σ'_3 is observed at the limb the fold with little dependence on the element's location (see Figure 5.2B). In summary, the reduction in overburden stress due to erosion/exhumation has significant influence on the decrease of the compressive stress in the folding layer due to buckling.

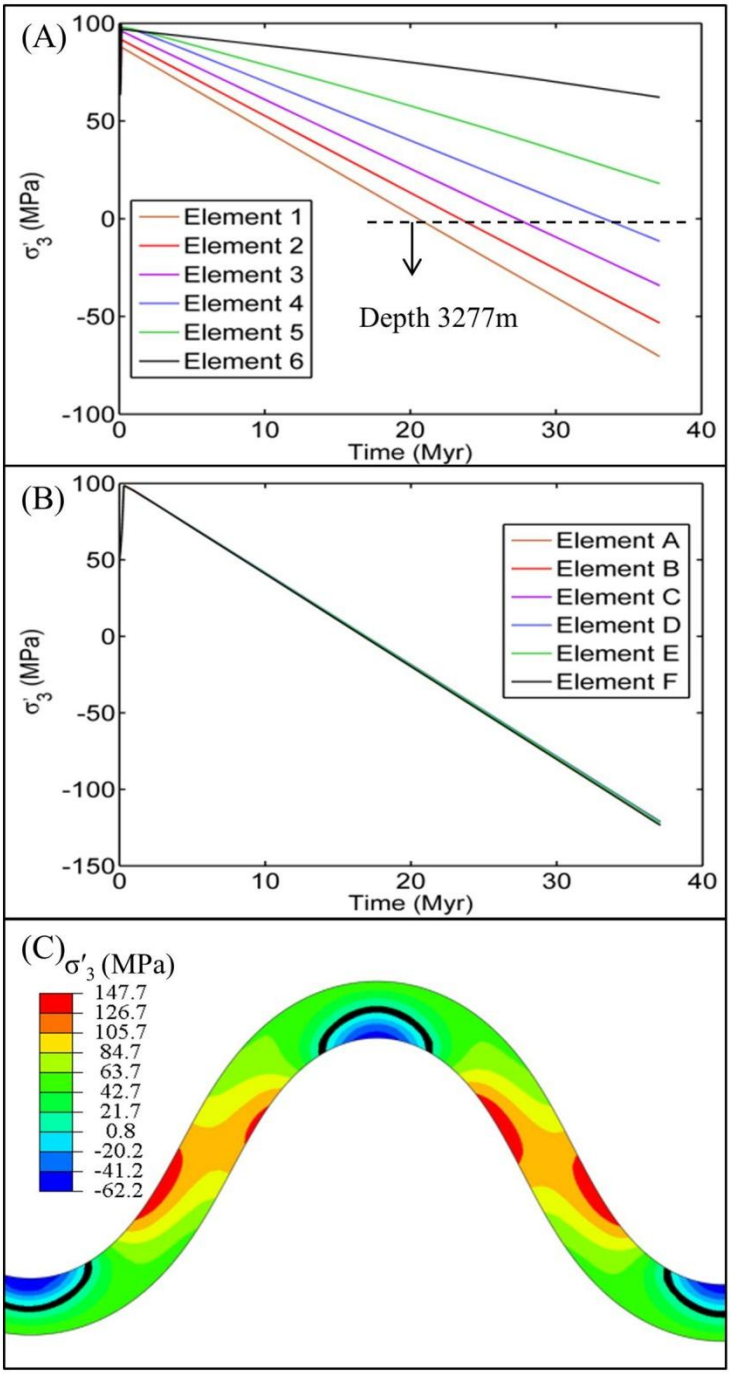

Figure 5.2 Stress history for erosion/exhumation study. (A) σ'_3 magnitudes evolution during the erosion/exhumation process for the high permeability model (10^{-15} m^2) at the crest of the fold. (B) σ'_3 magnitudes during the erosion/exhumation process for the limb of the fold. (C) σ'_3 magnitudes distribution at the folding layer after 3.7 Ma of erosion.

The positive contours showed in Figure 5.2C represents the magnitude of the tensile stresses (following the engineering sign convention of tension positive). Tensile stresses are observed both at the top of the crest in the hinge zone and at the limbs. Considerable tensile stresses (e.g. >100 MPa) are generated at the limbs. The compressive and tensile stresses are separated by the black line in Figure 5.2C. Similar results are observed by Frehner (2011) where tension occurs across the limbs at an early shortening stages (36% shortning). It should be noted that Frehner's modeling results are based on the state of strain without considering gravity. After comparing the distribution of tensional strain (Frehner's study) to tensional stresses after erosion (this study), the similarity leads to the conclusion that the reduction in overburden stress causes the amplification of the buckling stresses due to the remnant tensile strain in the folded layer. The remnant tensile strain is developed during buckling.

5.1.2. Low Permeability Model

In order to investigate the influence of erosion/exhumation on the evolution of pore pressure, a low permeability model is established (see Figure 5.3). The folding layer is embedded in a 500 m thick low permeability matrix ($k = 10^{-23}$ m^2). The overburden is assigned a high permeability (10^{-15} m^2) in order to simulate hydrostatic pore pressure dreop with depth during the erosion/exhumation process. The same erosion/exhumation rate (0.1 mm/yr) is applied.

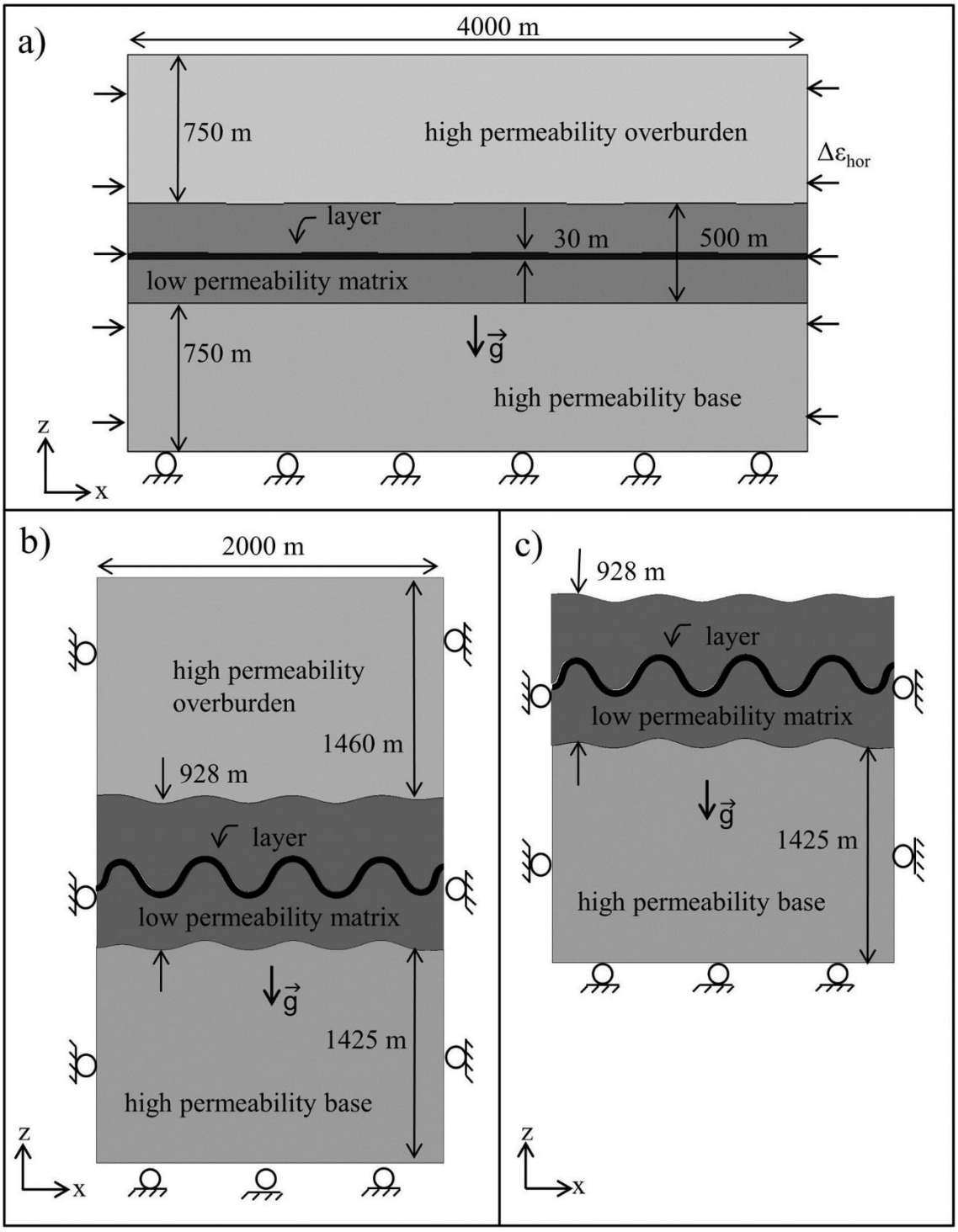

Figure 5.3 Model setup for low permeability erosion/exhumation model study. (A) model setup for the low permeability study. b) Model geometry and dimensions after 50% shortening. c) Model geometry after erosional load step resulting in surface topography.

Compared to the stress development of the folding layer in the high permeability model, obvious differences of the minimum principle stress evolution during the erosion/exhumation process are observed (see Figure 5.4A and C). Instead of a linear decrease in σ'_3 magnitudes, a significant increase of σ'_3 occurs at both the crest and on the limb in the low permeability model. Maximum compressive σ'_3 are developed around 4 Ma both at the crest and the limb. The following decrease (Figure 5.4 A and C) occurs at a lower rate and no tensile stresses are observed after 15 Ma of erosion/exhumation process with 1460 meters of overburden removed. Considering the relations of effective principle stress and pore pressure, the pore pressure development of the folding layer at the crest and limb are plotted (see Figure 5.4 B and D). Unlike the pore pressure which remains hydrostatic during shortening for the high permeability overburden, the pore pressure in the low permeability matrix develops into overpressure and increases significantly with shortening (see Figure 4.52). Once the erosion/exhumation process begins, the overpressure drops significantly compared to the red line which represents the hydrostatic pore pressure decrease according to the decrease in overburden pressure (see Figure 5.4 B and D). This significant decrease is much larger than the reduction of the total horizontal stress which is caused by the erosion. Thus, an increase of σ'_3 is observed in the first 4 Ma both at the hinge zone and the limb. The gradient of the significant decrease pore pressure declines with time. After approximately 6-7 Ma, the pore pressure is close to the equivalent hydrostatic decrease (calculated by depth, see equation 111). After that, the minimum effective stress begins to decrease. The pore pressure evolution in the low permeability matrix can be explained by observations from 1D consolidation studies (e.g. Jiao and Zheng, 1998; Ellis and Darby, 2005).

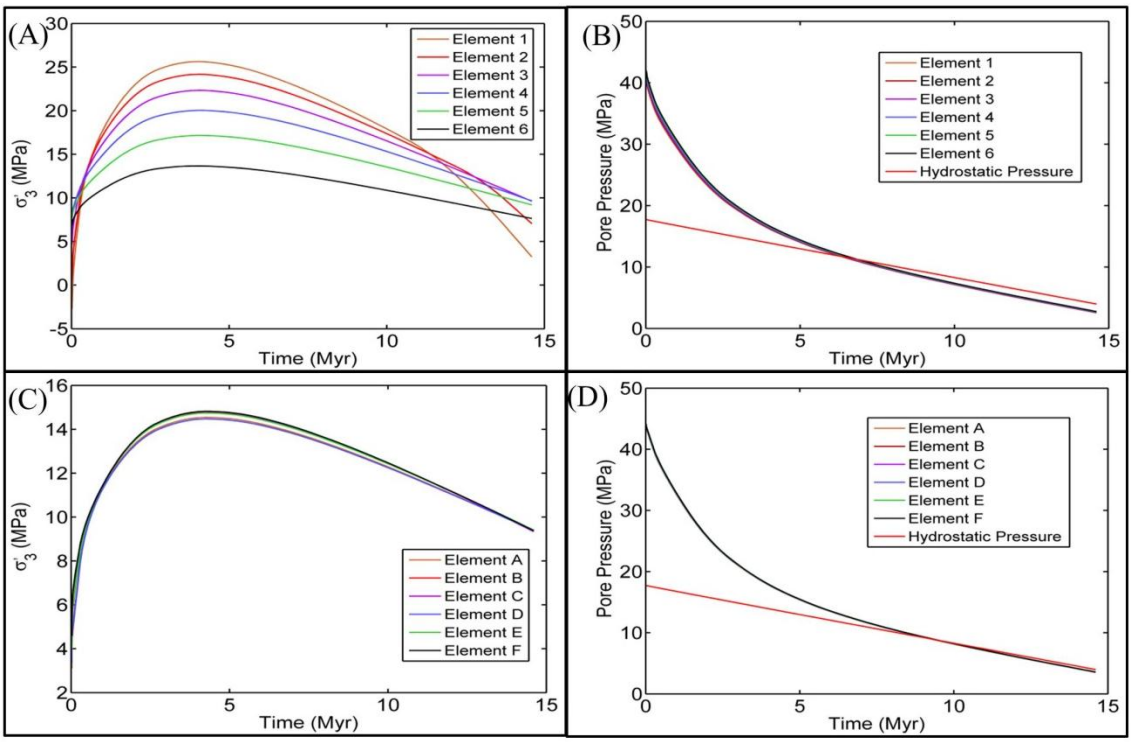

Figure 5.4 Stress history for low permeability erosion/exhumation model. (A) σ'_3 magnitudes during the erosional unloading for the low permeability model (10^{-19} m^2) at the crest of the fold. (B) Pore pressure magnitude evolution during the erosional unloading for the low permeability model (10^{-19} m^2) at the crest of the fold. The red line represents hydrostatic decrease. (C) σ'_3 magnitudes during the erosional unloading for the limb of the fold showing the same trend as for the crest.(D) Pore pressure magnitudes decrease on the limb during erosion.

5.2. Stress Orientation and Tensile Fractures

From the previous discussion, tensile failure has been developed both at the fold's crest and throughout the limbs by applying the erosional process after buckling. To fully understand the occurrence of folding related tensile failure, the tensile stress magnitudes from the numerical simulation and their orientations are combined to investigate different types of tensile failure during the folding history. For the low permeability rocks (e.g. 10^{-23} m^2, see section 4.6), tensile failure is observed to be subhorizontal and parallel to the folding layer during the early stage of shortening (< 5% shortening, see Figure 5.5A) for the top and bottom element. For the central elements bedding parallel tensile failure occurs for 0-20% shortening. For a later period of buckling, tensile stress is observed at

the top of the crest in low permeability ($<10^{-18}$ m^2) rocks due to the existence of overpressure. Fractures orientate vertically and parallel to the fold axis (Figure 5.5B). For high permeability ($>10^{-18}$ m^2) rocks, tensile failure can be observed both at the crest and limb of the folding layer during erosional unloading process. Based on the orientations of σ'_3, tensile fractures are parallel to the fold axis and orientated vertically at the crest. For the limb, tensile fractures are widespread across the limb and are parallel to the fold axis and perpendicular to the bedding (Figure 5.5C). Thus, the existences of fracture set 6 on Figure 1.3 in the limb and at the top of the crest of buckle folds are explained by this numerical simulation. Regarding to the fracture set 5 of Figure 1.3, Reber et al. (2010) conclude that it forms during low fold amplitudes under layer-subparallel compression. In order to study the existence of this fracture set (i.e. distributed at the fold limbs and perpendicular to the fold axis), the out-of-plane principal stresses (σ'_2) in the 2D modeling results are investigated (Figure 5.5). However, σ'_2 is observed to decrease to tensile stress at the top of the crest only for the low permeability (10^{-19} m^2) with low initial overburden (500 m). Furthermore, σ'_2 during the early stages acts as a compressive stress and is incapable to promote the occurrence of subvertical tensile fractures perpendicular to the fold axis (Figure 5.5). Hence the 2D numerical modeling results cannot explain the existence of fracture set 5 (see Figure 1.3) and does not agree with Reber et al.'s (2010) conclusion which is based on the history of stress orientations during folding.

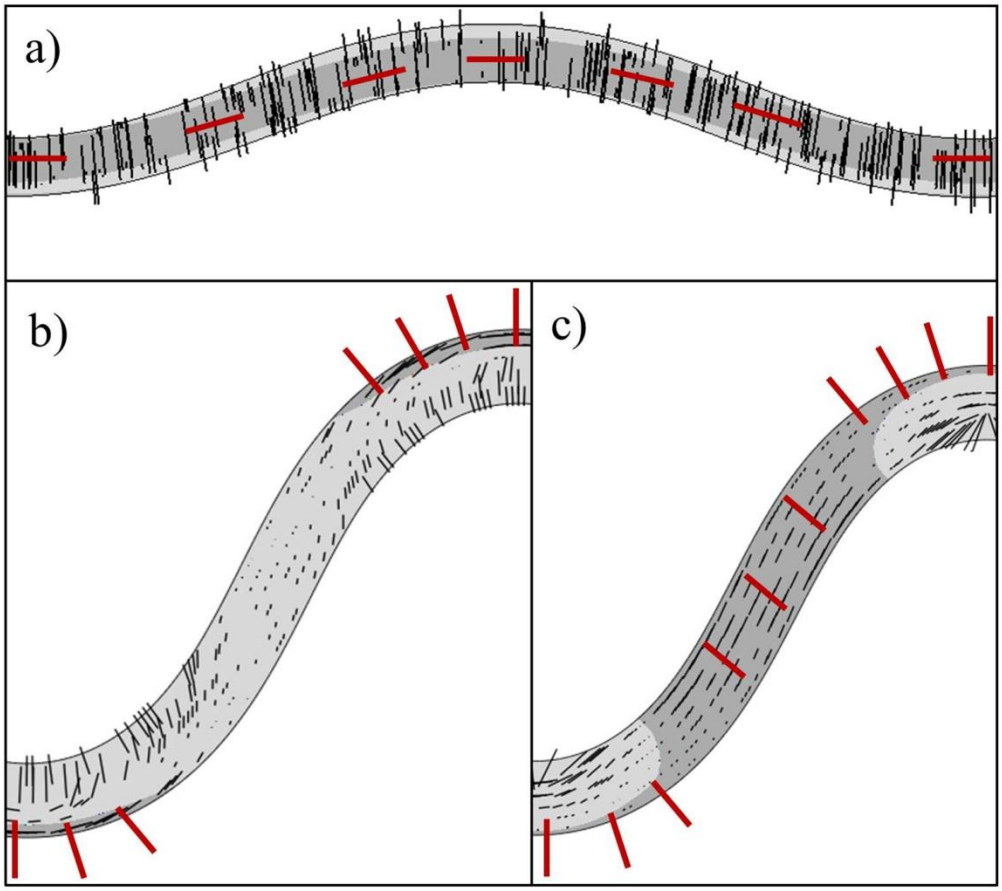

Figure 5.5 Orientations of tensile failure (red lines) for different models. The darker grey contours show the spatial extent of tensile stress magnitudes. (A) During the early stages of buckling for low permeability (10^{-23} m^2) model. (B) During the late stages of buckling for low permeability rocks ($<10^{-18}$ m^2). (C) For high permeability rocks ($>10^{-16}$ m^2) tensile failure occurs during erosional unloading.

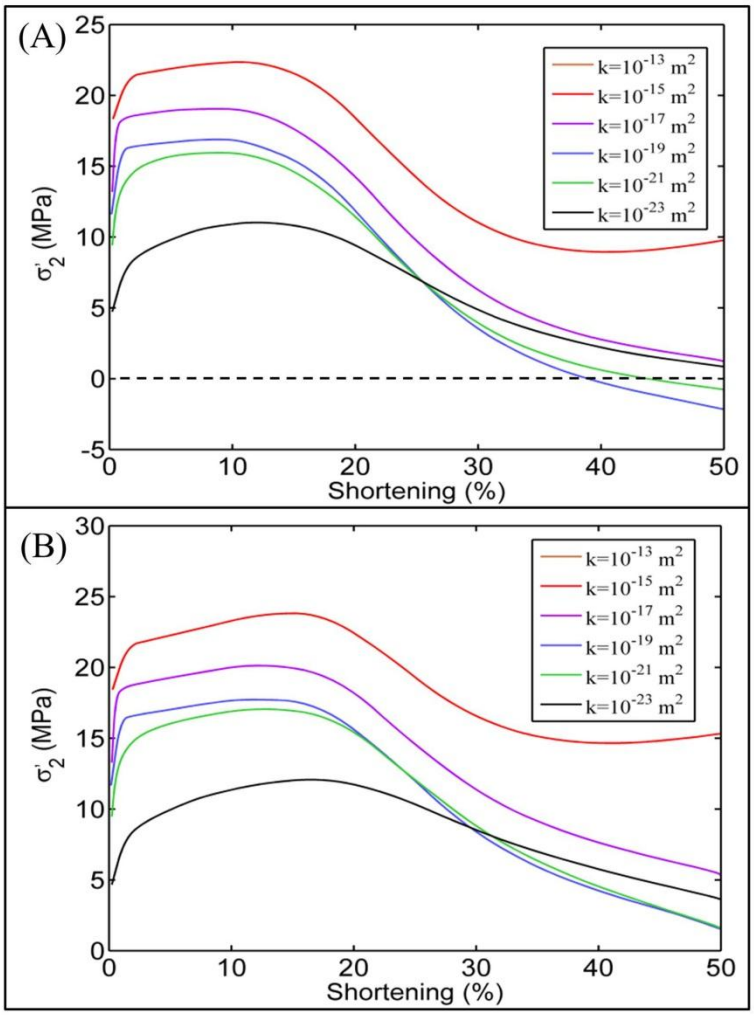

Figure 5.6 Out-of-plane effective principal stress (σ'_2) magnitude history for the crest (A) and limb (B) for varying permeability and low initial overburden (500 m).

5.3. Limitations

The application of 2D plane strain for this numerical simulation of Newtonian visco-elastic material buckling has some limitations.

(1) The 2D plane strain approach limits the analysis of the out-of-plane principal stress due to the assumption that the out-of-plane strain is zero ($\varepsilon_{yy}= \varepsilon_{xy}= \varepsilon_{zy}=0$). Therefore, a detailed analysis of tensile stresses in the direction of the out-of-plane principal stress (σ'_2) is restricted. The only case with tensile stress along the out-of-plane principal direction is the model with the low permeability and low overburden depth after

40% shortening. Considering the fact that stress magnitudes are directly dependent on the boundary conditions in that dimension (e.g. constrained, compressed or extended), the study of the initiation of tensile fracture which is perpendicular to the fold axis (fracture set 5 in Figure 1.3) requires a 3D modeling approach.

(2) Another limitation of this numerical modeling approach is the omission of a tensile failure criterion and the associated development of plastic strain in ABAQUS^{TM}. Once the tensile stress reaches the failure criterion, most sedimentary rocks will fail and stress will stop to increase. Due to this omission large tensile stress is developed (e.g. > 20 MPa) in the model even though the tensile failure criterion is reached. However, the objective of this research is to analyze the spatial and temporal development of tensile stresses. Thus, instead of studying on the stress evolution after tensile failure, this study focuses on the tensile stress history, which is considered as a critical factor for the initiation of tensile failure.

(3) For the influence of viscosity on the effective minimum principle stress evolution, an assumption that the rock's viscosity is constant has been applied. However, most materials' viscosity is considered as stress-depended. Thus, stress-depended viscosity is necessary for future studies.

(4) For the erosion/exhumation simulation, rock deformation is considered as an isothermal processes and the thermal stresses due to temperature changing during exhumation/erosion are not included. Erosion is considered as a process that enables to result in a rapid geotherm change and temperature decrease (Twiss and Moores, 2007). Furthermore, the thermal stress induced by erosion/exhumation may have a significant influence on the pore pressure evolution if pore elasticity is considered. Since these topics are considered to be beyond the objective of this paper, no thermal stress is included in this study.

6. SUMMARY AND CONCLUSIONS

6.1. SUMMARY

This study applies a 2D plane strain numerical modeling approach to simulate Newtonian single layer buckle folds. This analysis, based on the effective stress evolution on the fold's crest and limb, investigated the significant influence of different material parameters (e.g. overburden thickness, strain rate, viscosity, competence contrast, and most importantly permeability) on fold related tensile failure. Based on the analysis, tensile stress and associated tensile failure only develop at the folding layer under special conditions. Buckling due to layer-parallel shortening will result in extensional strain regions at the top of the crest and compressive strain region at the bottom of the crest. However, the occurrence of tensile stress and related failure cannot be explained by buckling only.

Important conclusions found in this research are listed as follows:

- The effective principle stress orientations and magnitudes vary throughout the folding layer during different stages of the deformation. The crest of the fold will be the first place to develop tensile stress, if possible.
- The competence contrast (R) between matrix and fold layer has significant effect on both the folding layer deformation and the stress evolution. Higher R leads to high amplitude fold structures and tensile stress at the fold's crest. Lower R results in lower amplitude folds and higher magnitudes of σ'_3 (shear stress) at the crest of the fold.
- A change in viscosity changes the fold deformation from tight to open and effects on the decrease of σ'_3 at the crest of the fold. Tensile stress can be formed for high viscosity (10^{20} Pa s).
- The stain rate has influence on the rock behavior during horizontalk compression and the decrease of σ'_3 at the crest of the fold. For lower strain rates (e.g. 10^{-12} sec^{-1}), the folding layer exhibits obvious viscous behavior and tensile stress is hard to produce on the crest.

- The initial overburden stress determines the magnitude of σ'_3 at the crest of the fold. Tensile stress is possible to be achieved at the crest when the overburden pressure is lower than 7.8MPa after 27% shortening. Higher overburden pressures reduce the possibility of tensile stresses and failure at depth. Depending on folding conditions tensile failure at greater depths may not occur (different as commonly expected).
- Permeability acts as a crucial factor on tensile stress evolution and related failure because of its relations with the generation of compression associated over-pressure. Tensile stress is observed on the top of fold after a certain amount of shortening (around 40%) when the permeability is smaller than 10^{-18} m^2. Rocks with a low permeability (10^{-23} m^2) develop tensile stresses in the limb of the fold in the early stages of shortening (<5%).
- Matrix permeability has the most significant influence on development of tensile stresses. Heterogeneous hydraulic conductivity between folding layer and matrix has slight influence on the stress history.

Based on the simulation results analysis, it can be concluded that tensile stresses at the top of the fold crest are unlikely to be generated at large depth unless a high competence contrast, extremely high strain rates or low permeability conditions occur. With the decrease of overburden pressure, tensile failure becomes more likely to develop at the top of fold's crest. Tensile fractures formed at the top of the crest are oriented subvertically and parallel to the fold axis. No obvious relation is found between buckling due to layer-parallel shortening and tensile stresses observed at the limb of the fold, except for the model with extremely low permeabilities (10^{-23} m^2) where tensile fractures form parallel to the layer during the early stage of shortening.

The process of erosion/exhumation has been simulated and exhibits a significant impact on the evolution of stress within a buckle fold. For high permeability ($k>10^{-16}$ m^2) rocks, pore pressure is found to be determined by depth only and to remain hydrostatic during all load steps (shortening and erosion). The generation of tensile stresses is observed throughout the fold structure after erosion. It can be concluded that the generation of tensile stresses (at the crest and throughout the limb of the fold) at significant depths (~3km) can be explained by the erosion/exhumation process of high

permeability rocks. Tensile fractures at the crest are oriented perpendicular to the fold axis and tensile fractures in the limb are oriented parallel to the fold axis. For low permeability rocks erosional unloading results in an increase of σ'_3 magnitudes during the early period of erosion/exhumation process (5 Ma). During this period the pore pressure decreases significantly until it reaches the hydrostatic level. As a result, the possibility of tensile stresses generation at the top of crest and at the limb decreases.

6.2. OUTLOOK

The presented study shows dynamical behavior of the single layer Newtonian buckle fold and related stress history in two dimensional (2D) numerical models. For the natural fold-related structures, the rock deformation, such as layer-parallel shortening, is always generated in three dimensional (3D) spaces instead of 2D. For some cases, it is possible that a 2D model can provide a reasonable approximation to the rock mechanics and related stress development. However, the 2D model is characterized by the incapability of the full 3D effect of geometry, material properties variation, and boundary conditions. Therefore, a 3D modeling approach is recommended for future studies of fold related fractures.

In the presented numerical simulations, the soil viscosity has only been considered both constant and independent of stress. However, the soil viscosity in both folding layer and matrix can be modified by the change of pressure because the crustal rocks viscosity is stress-dependent (Twiss and Moores, 2007). Such environment effects on rock viscosity have influence on both the shape and stress developments of fold structures. The application of stress-dependent viscosity has to be further investigated to study the complex dynamical behavior of the fold structures.

The consideration of volume change related to fluid storage and flow may also be included in future numerical simulations. The assumption of constant folding layer thickness may be invalid when a negative volume change is generated from the collapse of rock porosity, followed by a reduction in bulk permeability (Price and Cosgrove, 1990). The concern of volume change as a function of structure and mechanical

stratigraphy may enable the prediction of permeability to depend on the complete state of stress instead of overburden pressure only.

Including thermal stresses during the erosion/exhumation is necessary for future study since erosion is considered to result in significant temperature decrease (Twiss and Moores, 2007). Considering the relations between pore pressure and effective principle stress, correlating the pore pressure evolution and thermal stresses during the erosion/exhumation may be crucial for the study of the pore pressure evolution.

Further, the extension of the single layer model to a more realistic multilayer geometry may also be considered. A typical multilayer system contains several layers with certain viscosities and thicknesses. The theory of multilayer folding development so far is based on an approach similar to those for single layers folding (e.g. Biot,1961; Ghosh, 1968; Ramberg and Stroumgard,1971; Kidan and Cosgrove,1996). The previous studies mainly focus on the influence of multiple interfaces and layers of different viscosities. Few, however, are concerned with either the faults or fractures created during the folding progress of a multilayer system. Also a realistic state of stress including pore pressure and gravity has not been considered (e.g. Schmalholz and Podladchikov, 2001; Muhlhaus et al., 2002; Schmalholz et al., 2005). Thus, the numerical simulation based on realistic state of stress is necessary for future investigations.

BIBLIOGRAPHY

Abbassi, M. R. and N. S. Mancktelow, (1990), The effect of initial perturbation shape and symmetry on fold development. J. Struct. Geol., 12,273-282.

Abbassi, M. R. and N. S. Mancktelow, (1992), Single layer buckle folding in non-linear materials-I. Experimental study of fold development from an isolated initial perturbation. J. Struct. Geol., 14,85-104.

Bathe, K. J. (2008), Finite element method." Wiley Encyclopedia of Computer Science and Engineering.

Bergbauer, S., and D. D. Pollard, (2004), A new conceptual fold-fracture model including prefolding joints, based on the Emigrant Gap anticline, Wyoming, Geol. Soc. Am. Bull., 116(3-4), 294-307, doi: 10.1130/B25225.1.

Biot, M.A. (1959), On the instability of folding deformation of a layered viscoelastic medium in compression. J. Appl. Mech., 26, 393-400.

Biot, M. A. (1961), Theory of folding of stratified viscoelastic media and its implications in tectonics and orogenesis, Geol. Soc. Am. Bull., 72, 1595-1620.

Biot, M. A., H. Ode, and W. L. Roever, (1961), Experimental verification of the theory of folding of stratified viscoelatic media, Geol. Soc. Am. Bull., 72, 1621-1632.

Bobillo, N.C., F.Bastida, and J. Aller, (2000), On tangential longitudinal strain folding. Tectonophysics 319, 53-68

Bourne, S. J. (2003), Contrast of elastic properties between rock layers as a mechanism for the initiation and orientation of tensile failure under uniform remote compression, Journal of Geophys. Res/ (1978–2012), 108(B8), doi: 10.1029/2001JB001725.

Buchmann, T. J., and P. T. Connolly, (2007), Contemporary kinematics of the Upper Rhine Graben: A 3D finite element approach, Global and Planetary Change, 58(1), 287-309, doi: 10.1016/j.gloplacha.2007.02.012.

Byerlee, J. D. (1978), Friction of rocks. Pure and Applied Geophysics, v. 116(4-5),615-626.

Chapman, Richard E. (2000), Petroleum geology. Elsevier, New York.

Chapple, W.M. (1968), A mathematic theory of finite-amplitude rock-folding. Geol. Soc. Am. Bull., 79, 47-68.

Chapple, W. M. (1969), Fold shape and rheology: the folding of an isolated viscous-plastic layer. Tecronophysics, 7, 97-116.

Clough, R.W. (1960), The finite element analysis in plane stress analysis, Proc. 2nf ASCE Conf. on Electronic Computation, Pittsburgh, PA, September.

Cobbold, P. R. (1975), Fold propagation in single embedded layers. Tectonophysics, 27,333-351.

Coulomb, C.A. 1776. Essai sur une application des regles des maximis et minimis a quelquels problemesde statique relatifs, a la architecture. Mem. Acad. Roy. Div. Sav. 7: 343-387.

Dassault Systèmes (2011), ABAQUS® User Manual (version 6.11). SIMULIA, a division of Dassault Systèmes, Providence, Rhode Island.

Davis D., J. Suppe, and F. A. Dahlen, (1983), Mechanics of fold‐and‐thrust belts and accretionary wedges[J]. Journal of Geophysical Research: Solid Earth (1978–2012), 88(B2): 1153-1172.

Davis, R. O., and A.P. Selvadurai, (1996), Elasticity and geomechanics. Cambridge University Press.

Dhatt, G., and G. Touzot (2012), Finite Element Method. John Wiley and Sons.

Prisco C., and S. Imposimato, (1996), Time dependent mechanical behaviour of loose sands. Mechanics of Cohesive-Frictional Materials, Vol. 1,45-73.

Dick, H. J., and M. S. John, (1979), Compositional layering in alpine peridotites: evidence for pressure solution creep in the mantle. The Journal of Geology (1979): 403-416.

Dick, J.B. and J.M. Sinton, (1979), Compositional Layering In Alpine Peridotites; Evidence For Pressure Solution Creep In The Manlte, J Geol, V 87, 403-416.

Dieterich, J. H., and N. L. Carter, (1969), Stress-history of folding, Am. J. Sci, 267(2), 129-154.

Ellis, S., and D. Darby, (2005), A modified Terzaghi consolidation factor for first-order estimation of overpressure resulting from sedimentation: review and synthesis, Mathematical geology, 37(1), 115-123, doi: 0.1007/s11004-005-8750-0.

Ericsson, J. B., H. C. McKean, and R. J. Hooper, (1998), Facies and curvature controlled 3D fracture models in a Cretaceous carbonate reservoir, Arabian Gulf, Geological Society, London, Special Publications, 147(1), 299-312, doi: 10.1144/GSL.SP.1998.147.01.20.

Fischer, M. P., and M. S. Wilkerson, (2000), Predicting the orientation of joints from fold shape: Results of pseudo–three-dimensional modeling and curvature analysis. Geology, 28(1), 15-18, doi: 10.1130/0091-7613(2000)028<0015:PTOOJF>2.3. CO; 2

Fjar, Erling, R.M. Holt, and A.M. Raaen, (2008), Petroleum related rock mechanics. Vol. 53. Elsevier, UK.

Fletcher, R.C. (1974), Wavelength selection in the folding of a single layer with power-law rheology. Am. J. Sci, 274, 1029-1043.

Fletcher, R.C. (1977), Folding of a single viscous layer: exact infinitesimal amplitude solution. Tectonophysics, 39, 593-606.

Fletcher, R.C. (1979), The shape of single-layer folds at small but finite amplitude. Tectonophysics, 60, 77-87.

Fossen, Haakon. (2010), Structural geology. Cambridge University Press, UK.

Frehner, M. (2011), The neutral lines in buckle folds, J. Struct. Geol., 33(10), 1501-1508, doi: 10.1016/j.jsg.07.005

Ghosh, S.K. (1968), Experiments of buckling of multilayers which permit interlayer gliding. Tectonophysics, 6 (3), 207-249.

Groshong, R.H. (2006), 3-D structural geology. Springer, New York.

Hancock, P. L., and T. Engelder, (1989), Neotectonic joints, Geol. Soc. Am. Bull., 101(10), 1197-1208.

Harrison J. P, and .J A. Hudson, (2000), Engineering rock mechanics-an introduction to the principles[M]. Access Online via Elsevier.

Hennings, P. H., J. E. Olson, and L. B. Thompson, (2000), Combining outcrop data and three-dimensional structural models to characterize fractured reservoirs: An example from Wyoming. AAPG bulletin, 84(6), 830-849.

Hooker, J. H., J. F. W. Gale, L. A. Gomez, S. E. Laubach, R. Marrett, and R. M. Reed, (2009), Aperture-size scaling variations in a low-strain opening-mode fracture set, Cozzette Sandstone, Colorado. J. Struct. Geol., v. 31, p. 707–718,doi:10.1016 /j.jsg.2009.04.001.

Hubbert M K, and W. Rubey, (1959), Role of fluid pressure in mechanics of overthrust faulting I. Mechanics of fluid-filled porous solids and its application to overthrust faulting. Geol. Soc. Am. Bull., 70(2): 115-166.

Hudleston, P.J. (1973), An analysis of single-layer folds developed experimentally in viscous media. Tectonophysics, 16, 189-214.

Hudleston, P.J., and T.B. Holst, (1984), Strain analysis and fold shape in a limestone layer and implications for layer rheology. Tectonophysics 106, 321-347.

Jaeger, J. C. and N. G. Cook, (1979), W, Fundamentals of Rock Mechanics. Chapman and Hall, London.

Jiao, J. J., and C. Zheng, (1998), Abnormal fluid pressures caused by deposition and erosion of sedimentary basins, Journal of Hydrology, 204(1), 124-137, doi: 10.1016/S0022-1694(97)00115-7.

Johnson, A. M., and R. C. Fletcher, (1994), Folding of viscous layers: mechanical analysis and interpretation of structures in deformed rock, Columbia University Press, New York.

Karato S. (2008), Deformation of earth materials: an introduction to the rheology of solid earth. Cambridge University Press, UK.

Kidan, T. W. and J. W. Cosgrove, (1996), The deformation of multilayers by layer normalcompression; an experimental investigation. J. Struct. Geol., 18(4), 461-474.

Kocher, T., N.S. Mancktelow, and S.M. Schmalholz, (2008), Numerical modelling of the effect of matrix anisotropy orientation on single layer fold development. J. Struct. Geol. 30, 1013-1023.

Kocher, T., S.M. Schmalholz, and N.S. Mancktelow, (2006), Impact of mechanical anisotropyand power-law rheology on single layer folding. Tectonophysics 421, 71-87.

Ladeira, F. L., and N. J. Price, (1981), Relationship between fracture spacing and bed thickness. J. Struct. Geol. 3.2 179-183.

Ladeira, Fernando Lage. (1978), Relationship of Fractures to Other Geological Structures in Various Crustal Environments." PhD diss., Imperial College London (University of London).

Laubsher, H. B, 1975. Viscous component in Jura. Tectonophysics 27, 239-254.

Lemiszki, P. J., J. D. Landes, AND R. D. Hatcher, (1994), Controls on hinge-parallel extension fracturing in single-layer tangential-longitudinal strain folds, Journal of Geophysical Research: Solid Earth (1978–2012), 99(B11), 22027-22041, doi: 10.1029/94JB01853.

Lisle, R. J. (1994), Detection of zones of abnormal strains in structures using Gaussian curvature analysis, AAPG bulletin, 78(12).

Mancktelow, N.S. (1999), Finite-element modeling of single-layer folding in elasto-viscous materials: the effect of initial perturbation geometry, J. Struct. Geol., 21, 161-177, doi: 10.1016/S0191-8141(98)00102-3.

Mancktelow, N. S. (2002), Finite-element modeling of shear zone development in viscoelastic materials and its implications for localization of partial melting. J. Struct. Geol., 24(6), 1045-1053.

McQuillan, H. (1973), Small-scale fracture density in Asmari Formation of southwest Iran and its relation to bed thickness and structural setting, AAPG Bulletin57.12:2367-2385.

Medina, C.R., J.A. Rupp, and D.A. Barnes. (2011), Effects of reduction in porosity and permeability with depth on storage capacity and injectivity in deep saline aquifers: A case study from the Mount Simon Sandstone aquifer, International Journal of Greenhouse Gas Control, 5,146-156, doi: 10.1016/j.ijggc.2010.03.001.

Meyer, Rudi (2002), Anisotropy of sandstone permeability. CREWES Research Report . 14 (2002), 1-11.

Műhlhaus, H. B. (1993), Evolution of elastic folds in plane strain, Modern Approaches to Plasticity .Elsevier, Amsterdam, 737-765.

Mühlhaus, H. B., F. Dufour, L. Moresi, and B. Hobbs, (2002), A director theory for visco-elastic folding instabilities in multilayered rock. International Journal of Solids and Structures, 39(13), 3675-3691.

Murray, G. H. (1968), Quantitative fracture study; sanish pool, McKenzie County, North Dakota. AAPG Bulletin 52.1 : 57-65.

Narr, W., and Suppe, J. (1991), Joint spacing in sedimentary rocks. J. Struct. Geol., 13(9), 1037-1048, doi:10.1016/0191-8141(91)90055-N.

Pfiffner, O. A., and J. G. Ramsay, (1982), Constraints on geological strain rates: arguments from finite strain states of naturally deformed rocks. Journal of Geophysical Research,87, 311-321.

Ortega, O. J., R. Marrett, and S. E. Laubach, (2006), A scale-independent approach to fracture intensity and average fracture spacing: AAPG Bulletin, v. 90, p. 193–208, doi:10.1306/08250505059.

Passchier, C.W., and R.A.J. Trouw, (2005), Microtectonics. 2nd Edition, Springer-Verlag, Berlin, Heidelberg.

Pearce, M.A., R.R. Jones, S.A.F. Smith, K.J.W. McCaffrey, and P. Clegg, (2006), Numerical analysis of fold curvature using data acquired by high-precision GPS. J. Struct. Geol. 28, 1640-1646.

Plumley, W.J. (1980), Abnormally high fluid pressure: survey of some basic principles. AAPG Bulletin, 14 (2002), 1-11.

Price N. J. and J. W. Cosgrove, (1990), Analysis of Geological Structures. Cambridge University Press, UK.

Price, N.J., (1974), The development of stress systems and fracture patterns in undeformed sediments, Advances in Rock Mechanics, Proc. 3rd Congr., ISRM, I: 487-496.

Price, Neville J. (1966), Fault and joint development in brittle and semi-brittle rock, Vol. 1. Pergamon Press, Oxford, UK.

Ramberg, H.(1960), Relationship between length of arc and thickness of ptygmatically folded veins, Am. J. Sci., 258, 36-46.

Ramberg, H. (1964), Selective buckling of composite layers with contrasted rheological properties, a theory for simultaneous formation of several orders of folds, Tectonophysics, 1, 307-341.

Ramberg, H., and K. E. Strömgård, (1971), Experimental tests of modern buckling theory applied on multilayered media. Tectonophysics, 11,461-472.

Ramsay, J. G. (1967), Folding and Fracturing of Rocks. McGraw-Hill, New York.

Reber, J. E., S. M. Schmalholz, and J. P. Burg, (2010), Stress orientation and fracturing during three-dimensional buckling: Numerical simulation and application to chocolate-tablet structures in folded turbidites, SW Portugal. Tectonophysics, 493(1), 187-195, doi: 10.1016/j.tecto.2010.07.016.

Sadd, M.H. (2009), Elasticity. Elsevier, Amsterdam.

Schmalholz, S. M. (2008), 3D numerical modeling of forward folding and reverse unfolding of a viscous single-layer: Implications for the formation of folds and fold patterns, Tectonophysics, 446(1), 31-41, doi: 10.1016/j.tecto.2007.09.005.

Schmalholz, S. M., Y. Y. Podladchikov, and B. Jamtveit, (2005), Structural softening of the lithosphere. Terra Nova, 17(1), 66-72.

Schmalholz, S. M., and Y.Y. Podladchikov, (1999), Buckling versus folding: importance of viscoelasticity, Geophysical Research Letters, 26(17), 2641-2644, doi: 10.1029/1999GL900412.

Schmalholz, S. M., and Y. Y. Podladchikov, (2001), Strain and competence contrast estimation from fold shape. Tectonophysics, 340(3), 195-213.

Schmalholz, S. M., Y. Y. Podladchikov, and J. P. Burg, (2002), Control of folding by gravity and matrix thickness: Implications for large ‐ scale folding, Journal of Geophysical Research: Solid Earth (1978 ‐ 2012), 107(B1), ETG-1, doi: 10.1029/2001JB000355.

Schmalholz, S.M., and Y.Y. Podladchikov, (2000), Finite amplitude folding: transition from exponential to layer length controlled growth. Earth and Planetary Science Letters 181, 619-633.

Sherwin, J.A., and W.M. Chapple, (1968), Wavelengths of single layer folds: a comparison between theory and observation. Am. J. Sci, 266, 167-179.

Shimamoto, T., and I. Hara, (1976), Geometry and strain distribution of single-layer folds. Tectonophysics 30, 1-34.

Sibson, Richard H. (2003), Brittle-failure controls on maximum sustainable overpressure in different tectonic regimes. AAPG bulletin 87.6: 901-908.

Sibson, Richard H. (2005), Hinge-parallel fluid flow in fold-thrust belts: how widespread? Proceedings of the Geologists Association 116.3: 301-309.

Silliphant, L. J., T. Engelder, and M. R. Gross, (2002), The state of stress in the limb of the Split Mountain anticline, Utah: constraints placed by transected joints, J. Struct. Geol., 24(1), 155-172, doi: 10.1016/S0191-8141(01)00055-4.

Smart, K. J., D. A. Ferrill, and A. P. Morris, (2009), Impact of interlayer slip on fracture prediction from geomechanical models of fault-related folds, AAPG bulletin, 93(11), 1447-1458, doi: 10.1306/05110909034.

Smart, K.J., D.A. Ferrill, A.P. Morris, B.J. Bichon, D.S. Riha, and L. Huyse, (2010a), Geomechanical modeling of an extensional fault-propagation fold: Big Brushy Canyon monocline, Sierra Del Carmen, Texas. American Association of Petroleum Geologists Bulletin 94, 221–240.

Smart, K.J., D.A. Ferrill, A.P. Morris, and R.N. McGinnis, (2010b), Geomechanical modeling of a reservoir-scale fault-related fold: the Bargy anticline, France. 44th U.S. Rock Mechanics Symposium, ARMA Paper 10–201.

Smart, K.J., D.A. Ferrill, D.W. Sims, N.M. Franklin, G.I. Ofoegbu, and A.P. Morris, (2004), Integrated structural analysis and geomechanical modeling: an aid to reservoir exploration and development. Gulf Rocks 2004 – 6th North American Rock Mechanics Symposium: Rock Mechanics Across Borders and Disciplines. Houston, TX, 5–9 June 2004: ARMA/NARMS Paper 04–470.

Smith, R.B. (1975), United theory of the onset of folding, boudinage and mullion structure. Geol. Soc. Am. Bull., 86, 1601-1609.

Smith, R.B. (1977), Formation of folds, boudinage and mullions in non-Newtonian materials. Geol. Soc. Am. Bull., 88, 312-320.

Smith, R.B. (1979), The folding of a strongly non-Newtonian layer. Am. J. Sci, 279, 272-287.

Stearns, D. W. (1964), Certain aspects of fracture in naturally deformed rocks, In: R.E. Riecker, NSF Adv. Sci., Seminar in Rock Mechanics, Spec. Rep., Air Force Cambridge Res. Lab., Bedford ,Mass., pp. 97-116.

Stearns, D. W., and M. Friedman (1972), Reservoirs in fractured rock, AAPG Memoir 16, 82–100.

Stearns, M. B. (1964), Variation of the Internal Fields and Isomer Shifts at the Fe Sites in the FeAl Series, Journal of Applied Physics, 35, 1095.

Stephansson, O. (1974), Stress-induced diffusion during folding. Tectonophysics, 22(3), 233-251.

Stewart, S. A.,and R. Podolski. (1998), Curvature analysis of gridded surfaces, inM.P. Coward, T.S. Daltaban, and H.Johnson, eds., Structural Geology in Reservoir Characterization, v. 127: London, Geological Society, Special Publications, p. 133-147.

Suo, Chonghui, Shimi Peng, Suoliang Chang, Rutai Duan, and Guangming Wang. (2012), A New Calculating Method of the Curvature to Predicting the Reservoir Fractures. Procedia Environmental Sciences 12: 576-582.

Terzaghi, K. (1936), The shearing resistance of saturated soils and the angle between planes of shear, in Proc. Int. Conf. Soil Mech. Found. Eng., Vol.1, Harvard University Press,Cambridge, MA,pp . 54–6.

Thies B. (2008), Three Dimensional Multi-scale Finite Element Analysis of the Present-day Crustal State of Stress and the Recent Kinematic Behavior of the Northern and Central Upper Rhine Graben. Logos Verlag Berlin GmbH, Berlin.

Tiab, D. and C. Donaldson, (2012), Petrophysics :Theory and Practice of Measuring Reservoir Rock and Fluid Transport Properties. Elsevier, New York.

Treagus, S. H. (1973), Buckling stability of a viscous single-layer system oblique to the principal compression. Tectonophysics, 19, 271-289.

Treagus, S. H. (1981), A theory of stress and strain variations in viscous layers, and its geological implications. Tectonophysics, 72, 75-103.

Turcotte, D. L., and G. Schubert, (2002), Geodynamics. Cambridge University Press, New York.

Twiss, R.J. and E.M. Moores, (2007), Structural Geology, 2nd Edition, W.H. Freeman and Company, New York.

Watts N L. (1987), Theoretical aspects of cap-rock and fault seals for single-and two-phase hydrocarbon columns. Mar. Petrol Geol., 4(4): 274-307.

Williams, J. R., R. W. Lewis, and O. C. Zienkiewicz, (1978), A finite element analysis of the role of initial perturbations in the folding of a single viscous layer. Tectonophysics ,45, 187-200.

Zhang, Y., N.S. Hobbs, B.E. Ord, and H.B. Muhlhaus, (1996), Computer simulation of single-layer buckling, J. Struct. Geol., 18, 645-655, doi: 10.1016/S0191-8141(96)80030-7.

Zhang, Y., Mancktlow, N.S., Hobbs, B.E., Ord, and H.B. Muhlhaus, (2000), Numerical modeling of single-layer folding: clarification of an issue regarding the possible effect of computer codes and the influence of initial irregularities, J. Struct. Geol., 22, 1511-1522, doi: 10.1016/S0191-8141(00)00063-8.

Zienkiewicz, O. C., R. L. Taylor, and J. Z. Zhu. (2005), The finite element method: its basis and fundamentals. Elsevier,UK.

VITA

Xiaolong Liu was born and raised in Dongying, China. He earned his Bachelor degree in Safety Engineering in 2010, from China University of Petroleum. After graduation, he pursued one year study in the program of Oil & Gas Storage and Transportation Engineering.

In August 2011, he attended Missouri University of Science and Technology in Rolla, Missouri for his graduate studies in petroleum engineering. Half a year later, he started positions of graduate research assistant and graduate teaching assistant in the Department of Geological Science and Engineering. In Dec, 2013, he received his M.S. in Petroleum Engineering from Missouri University of Science and Technology.